A system for time-encoded non-linear spectroscopy and microscopy

Dissertation
an der Fakultät für Physik
der Ludwig-Maximilians-Universität
München

vorgelegt von
Sebastian Karpf
aus München

München, den 04. Mai 2015

Erstgutachter:	Prof. Dr. Robert Huber
Zweitgutachter:	Prof. Dr. Wolfgang Zinth
Datum der mündlichen Prüfung:	15. Juni 2015

Zusammenfassung

Ramanstreuung kann in der biomedizinischen Bildgebung dazu eingesetzt werden, Moleküle in einer Probe zu identifizieren, ohne dass die Probe vorher aufbereitet werden muss. Raman Mikroskopie kann funktionelle Bereiche sichtbar machen, indem es einen molekularen Kontrast auf Größenordnungen der Zellen bereitstellt und wird damit hochinteressant für die Krankheitserkennung in biomedizinischer Bildgebung.

Der zugrundeliegende Raman Streuprozess ist ein optisch-inelastischer Streuungsmechanismus der die Detektion von Molekülschwingungen ermöglicht. Dabei wird das gestreute Licht detektiert und die Energiedifferenz zum Anregungslicht entspricht der molekularen Schwingungsenergie. Durch diese molekülspezifischen Schwingungsenergien ist es möglich, die Moleküle zu identifizieren und weiterhin durch die Signalhöhe zu quantifizieren. Diese Technik ist seit nunmehr beinahe einem Jahrhundert bekannt und findet breite Anwendung in Gebieten wie der Biologie, Chemie und der Medizin. Das Problem der Ramanstreuung ist die geringe Signalstärke des Effekts, wobei normalerweise nur eines von einer Milliarde Photonen gestreut wird. Es ist jedoch möglich, diesen Effekt durch nichtlineare Techniken um einige Größenordnungen zu verstärken. Dies wird besonders relevant beim Einsatz in der biomedizinischen Bildgebung von hochstreuendem Gewebe und bei hochauflösender Spektroskopie, wo gewöhnliche, gitterbasierte Spektrometer an ihre Grenzen stoßen. In der vorliegenden Arbeit wird ein neues System zur stimulierten Ramanstreuung (SRS) und hyperspektralen Ramanmikroskopie mittels eines schnell wellenlängenabstimmbaren Lasers vorgestellt. Hierfür wurde eine neue, zeitkodierte (TICO) Technik entwickelt, die es ermöglicht, die abgefragte Raman-Schwingungsenergie in der Zeit zu kodieren und weiter die durch SRS auftretende Leistungssteigerung direkt in der Zeitdomäne aufzunehmen, indem sehr schnelle Analog-zu-Digital-Wandler (ADC) mit 1.8 Gigasamples/s eingesetzt werden.

Der hierfür entwickelte Pumplaser ist ein faserbasierter Masteroszillator Leistungsverstärker (MOPA) mit integriertem Ramanwandler, der einen Betrieb bei 1064 nm, 1122 nm oder 1186 nm ermöglicht. Diese Mehrwellenlängenfähigkeit basiert auf dem Ramaneffekt in der Glasfaser, der durch ein Keimlicht einer 1122 nm Laserdiode stimuliert wird. Überraschenderweise wurde dadurch ebenfalls ein schmalbandiger Betrieb (0,4 cm^{-1}) der kaskadierten Ramanbanden bei 1186 nm und 1257 nm beobachtet, was zunächst der erwarteten breitbandigen Ramanbande von Glas widerspricht. Diese Ergebnisse wurden untersucht und es wird ein Modell vorgeschlagen, wonach der gefundene Effekt auf einer Kombination von Vier-Wellen-Mischen und kaskadierter Ramanstreuung beruht. Das schmalbandige kaskadierte Ramanlicht bei 1186 nm wurde im Experiment für hochauflösende Ramanspektroskopie von Benzol benutzt.

Als Raman Stokeslaser wurde ein schnell wellenlängenabstimmbarer Fourierdomänen modengekoppelter (FDML) Laser benutzt, der einige Vorteile kombiniert. Als wichtigste

Vorteile dieses faserbasierten Lasers sind die breite Abdeckung relevanter Ramanenergien, die sich von möglichen 250 cm^{-1} bis 3150 cm^{-1} erstreckt, die gleichzeitig hohe spektrale Auflösung (0.5 cm^{-1}), und der für biologische Bildgebung interessante Dauerstrich-Betrieb (CW) zu nennen. Weiterhin wurde eine neue, zweistufig balanzierte Detektion entwickelt, die SRS Messungen an der Schrotrauschgrenze ermöglichen. Die wohldefinierte Wellenlängen-zu-Zeit Beziehung dieses Lasers wurde darüber hinaus dafür benutzt, den TICO-Raman Spektren direkt Ramanenergien zuzuweisen. Dadurch wurden hochqualitative Ramanspektren mit akkurater Wellenzahlinformation möglich.

Das entwickelte System wurde für Anwendungen in der Raman Spektroskopie und nicht-linearen Bildgebung eingesetzt. Als Ergebnisse werden breitbandig abgetastete Ramanspektren präsentiert, die mit spontanen Raman Spektren verglichen werden. Weitere, neue spektrale Anwendungen wurden untersucht und erste Mikroskopiebilder erzeugt. Hierfür wurde die Probe mittels eines Verschiebetisches verfahren und an jedem Pixel ein TICO-Raman Spektrum aufgenommen. Die so erzeugten hyperspektralen Raman Mikroskopiebilder wurden in farbig kodierte Bilder mit molekularem Kontrast umgewandelt. Es wird eine TICO-Raman Mikroskopieaufnahme von einem Pflanzenschnitt präsentiert. Das System erlaubt es ferner, durch den Einsatz des hochintensiven Pumplasers Bilder mit Mehrphotonenabsorption zu messen, indem zweiphotonenangeregte Fluoreszenzbildgebung (TPEF) angewandt wird.

Zusammenfassend wird in dieser Arbeit die Entwicklung eines neuen Systems der Spektroskopie und nichtlinearen Bildgebung beschrieben und erste Messergebnisse präsentiert. Mit diesem System wird es möglich sein, viele verschiedene Bildgebungsverfahren zu verbinden. Darunter unter anderem Bildgebungsverfahren wie die optische Kohärenztomographie (OCT), Absorptionsspektroskopie, SRS, TPEF, Frequenzverdopplung (SHG) und Frequenzverdreifachung (THG) und Fluoreszenzlebenszeitmikroskopie (FLIM). Der wohl vielversprechendste Vorteil dieses Systems liegt in dem faserbasierten Design, welches es ermöglichen kann dieses System zukünftig zur endoskopischen Bildgebung einzusetzen. Bereits jetzt ergibt dieser faserbasierte Aufbau ein sehr robustes System, das verlässlich, justagefrei und einfach zu bedienen ist.

Abstract

Raman scattering can be applied to biological imaging to identify molecules in a sample without the need for adding labels. Raman microscopy can be used to visualize functional areas at the cellular level by means of a molecular contrast and is thus a highly desired imaging tool to identify diseases in biomedical imaging. The underlying Raman scattering effect is an optical inelastic scattering effect, where energy is transferred to molecular excitations. Molecules can be identified by monitoring this energy loss of the pump light, which corresponds to a vibrational or rotational energy of the scattering molecule. With Raman scattering, the molecules can be identified by their specific vibrational energies and even quantified due to the signal height. This technique has been known for almost a century and finds vast applications from biology to medicine and from chemistry to homeland security. A problem is the weak effect, where usually only one in a billion photons are scattered. Non-linear enhancement techniques can improve the signal by many orders of magnitude. This can be especially important for fast biomedical imaging of highly scattering media and for high resolution spectroscopy, surpassing the resolution of usual spectrometers.

In this thesis a new system for stimulated Raman spectroscopy (SRS) and hyperspectral Raman microscopy with a rapidly wavelength swept laser is presented. A time-encoded (TICO) technique was developed that enables direct encoding of the Raman transition energy in time and direct detection of the intensity change on the Stokes laser by employing fast analogue-to-digital converter (ADC) cards (1.8 Gigasamples/s).

Therefore, a homebuilt pump laser was developed based on a fiber-based master oscillator power amplifier (MOPA) at 1064 nm and extended by a Raman shifter that can shift the output wavelength to 1122 nm or 1186 nm. This is achieved by seeding the Raman amplification in the fiber with a narrowband 1122 nm laser diode. Surprisingly, this also leads to narrowband (0.4 cm^{-1}) cascaded Raman shifts at 1186 nm and 1257 nm, which is in contrast to the usually broadband spontaneous Raman transition in fused silica. The underlying effect was examined and therefore concluded that it is most probably due to a combined four-wave-mixing and cascaded Raman scattering mechanism. Experimentally, the narrowband cascaded Raman line was used to record a high-resolution TICO-Raman spectrum of benzene.

As Raman Stokes laser, a rapidly wavelength swept Fourier domain mode-locked (FDML) laser was employed which provides many advantages for SRS. The most important advantages of this fiber based laser are that it enables coverage of the whole range of relevant Raman energies from 250 cm^{-1} up to 3150 cm^{-1}, while being a continuous wave (CW) laser, which at the same time allows high resolution (0.5 cm^{-1}) spectroscopy. Further, it enables a new dual stage balanced detection which permits shot noise limited SRS measurements and, due to the well-defined wavelength sweep, the TICO-Raman technique directly provides high-quality Raman spectra with accurate Raman transition energy calibration.

This setup was used for different applications, including Raman spectroscopy and non-linear microscopy. As results, broadband Raman spectra are presented and compared to a state-of-the-art spontaneous Raman spectrum. Furthermore, several spectroscopic features are explored. For first imaging results, samples were raster scanned with a translational stage and at each pixel a TICO-Raman spectrum acquired. This led to a hyperspectral Raman image which was transformed into a color-coded image with molecular contrast. Biological imaging of a plant stem is presented. The setup further allowed performing multi-photon absorption imaging by two-photon excited fluorescence (TPEF).

In summary, this thesis presents the design, development and preliminary testing of a new and promising platform for spectroscopy and non-linear imaging. This setup holds the capability of biological multi-modal imaging, including modalities like optical coherence tomography (OCT), absorption spectroscopy, SRS, TPEF, second harmonic generation (SHG), third-harmonic generation (THG) and fluorescence lifetime imaging (FLIM). Amongst the most promising characteristics of this setup is the fiber-based design, paving the way for an endoscopic imaging setup. Already now, this makes it a robust, alignment-free, reliable and easy-to-use system.

Content

1. Introduction

Raman scattering is a scattering mechanism that can be used to identify molecules in a sample. First described by physicists Raman and Krishnan in 1928 [1], they discovered this phenomenon whereupon light is inelastically scattered and the energy difference is absorbed in molecular vibrations. These vibrations are highly dependent on the molecule type and can thus provide a "fingerprint" of the molecules, i.e. a unique identification. This discovery led to the Nobel Prize in physics being awarded to Sir Chandrasekhara Venkata Raman in 1930.

A drawback of conventional Raman scattering is the very small Raman scattering cross section, typically in the range of 10^{-30} $cm^2*sr^{-1}*molecule^{-1}$. This means, that typically only one photon in 10^9 is scattered, making the detection of these few photons technically difficult. Furthermore, when used in biological samples, tissue scattering can further obscure the scattered light.

A way to overcome this problem is to enhance the effect by non-linear techniques. Already in 1962 Woodbury and Ng [2] observed the stimulated Raman scattering (SRS) effect of nitrobenzene inside a laser resonator generating a strong light output at a new wavelength, not corresponding to any fluorescence line of the Ruby laser gain medium. In 1965, Maker and Terhune [3] discovered another non-linear Raman technique, where three photons generate a higher energetic, anti-Stokes photon. This technique was later given the name Coherent Anti-Stokes Raman Scattering (CARS) – an acronym chosen in honor of their employer Ford Motors Company. Many other interesting Raman techniques were invented over the years, providing advantages in different applications and drawbacks in others. One particularly interesting finding shall be highlighted here, as it does not involve highly intense laser light, but rather uses continuous wave (CW) light to accomplish stimulated Raman scattering. Owyoung et al. reported in 1977 [4] the use of a CW Helium-neon laser in combination with a tunable CW dye laser to generate stimulated Raman spectra. The advantage of this technique is the possibility to tune the energy difference between pump and Stokes laser to generate Raman spectra, which are non-distorted (as compared to e.g. CARS) and can thus be readily interpreted. Furthermore, they used low-power CW lasers for SRS, which is advantageous in preventing non-linear damage in the sample. SRS has the big advantage that the signal is linear in sample concentration (as opposed to quadratic in e.g. CARS). This allows usage of SRS as a convenient chemical analysis tool with the advantage of higher signal levels than in traditional spontaneous Raman scattering.

In this thesis I will describe a new system for SRS by employing rapidly wavelength swept lasers together with a new concept called time-encoded (TICO) Raman. The Stokes laser, a Fourier-Domain Mode-Locked (FDML) laser, is used to detect the stimulated Raman gain (SRG) resulting from SRS. FDML lasers were initially invented to enable high speed optical coherence tomography (OCT) imaging through the swept-source technique [5], but also short pulse generation was reported [6]. Typical sweep speeds are in the kHz to MHz

range, covering up to 200 nm in the Near-Infrared wavelength region (1000–1600 nm). These continuous sweep spans correspond to ~1000 cm^{-1} within a half period of the laser (~µs), making this light source highly interesting for high-speed SRS spectroscopy.

Another advantage of the FDML laser is the fiber-based design. Optical fibers are highly desired in biomedical applications, as the rather short penetration depth of optical imaging in tissue restricts the use to the surface proximity. One way to overcome this is to use fiber endoscopes, especially for biomedical imaging.

To this end, a system was developed that is capable of performing fast SRS Raman-spectroscopy and hyperspectral Raman microscopy, while being fiber-based.

2. Theory: Stimulated Raman scattering (SRS)

In spontaneous Raman scattering (Figure 2.1) the pump light at energy ω_{Pump} is inelastically scattered by a molecule. A photon at a new energy ω_{Stokes} or $\omega_{Anti\text{-}Stokes}$ is created, which has an energy difference to the pump photon corresponding to a Raman transition Ω_{Raman}. This Raman transition energy is stored in an excitation of either a molecular vibration or rotation. The excitation energy is highly dependent on the molecules geometry and its' composition and therefore permits the identification of the scattering molecule. In conventional, spontaneous Raman scattering the spectrum of the scattered photons is recorded which allows the determination of the species end even quantify the number of molecules in the sample.

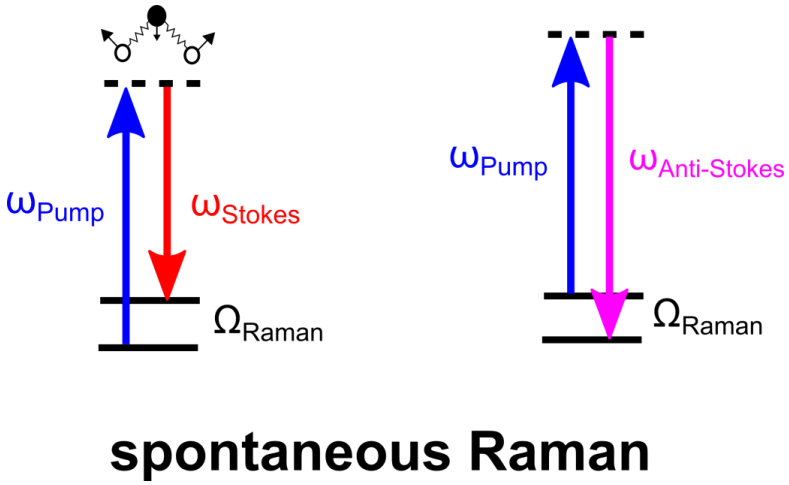

Figure 2.1: Energy diagram for spontaneous Raman scattering. A pump photon is inelastically scattered and energy is stored in a molecular vibration or rotation Ω_{Raman}. The Stokes photon is emitted at the energy difference $\omega_{Stokes} = \omega_{Pump} - \Omega_{Raman}$. In Anti-Stokes scattering, the emitted photon is at a higher energy $\omega_{Anti\text{-}Stokes} = \omega_{Pump} + \Omega_{Raman}$. Anti-Stokes scattering occurs when the photon is scattered by an already excited molecule (e.g. vibrating at thermal energy).

The excitation of a Raman transition can be explained as an interaction of the electrical field of the incident light with the molecule. The electrical field induces a polarization:

$$P(t) = \varepsilon_0 \chi^{(1)} E(t)$$

where ε_0 is the permittivity of free space and $\chi^{(1)}$ is the linear susceptibility [7]. This formula holds for small electrical fields, where the systems' response is linear. If higher fields are applied, as it is the case in high power laser irradiation, the polarization needs to be expanded by a power series and higher order terms need to be included:

$$P(t) = \varepsilon_0 \chi^{(1)} E(t) + \varepsilon_0 \chi^{(2)} E^2(t) + \varepsilon_0 \chi^{(3)} E^3(t) + \cdots$$

The higher order susceptibilities $\chi^{(2)}$ and $\chi^{(3)}$ are very small[1], but the high electric fields scaling with the squared or cubed order can make the higher terms comparatively large. This area of optics is thus called non-linear optics, as the effects scale with the squared or cubed exponent of the field. The strong electrical fields cause a non-linear response of the material irradiated. The susceptibility is a complex number, containing a real part $\mathrm{Re}\,\chi^{(3)}$, which describes absorption, and an imaginary part $\mathrm{Im}\,\chi^{(3)}$, which describes scattering effects like SRS.

Examples of processes that scale with the second order susceptibility $\chi^{(2)}$ are second-harmonic generation (SHG) or difference frequency generation. Interestingly, second order nonlinearities only occur in noncentrosymmetric molecules, so many materials providing inversion symmetry have a vanishing $\chi^{(2)}$.

Most materials provide inversion symmetry and can thus be probed by the third-order nonlinearity. SRS is such a third-order nonlinear effect. In third-order polarization effects, described by

$$P^{(3)}(t) = \varepsilon_0 \chi^{(3)} E^3(t),$$

the electric field can consist of three distinct electrical fields $\mathrm{E(t)} = \mathrm{E_1(t)} + \mathrm{E_2(t)} + \mathrm{E_3(t)}$. This leads to a total of 44 possible terms [7] including parametric processes, like four-wave mixing (FWM) and sum-frequency generation (SFG) and non-parametric processes, like stimulated Brioullin scattering (SBS) and SRS[2].

In SRS two light sources are incident on the sample: a Raman pump and a Raman probe light (Figure 2.2). If the energy difference between the two corresponds to a Raman transition, pump photons are scattered to probe photons[3]. The energy difference is stored in a molecular excitation Ω_{Raman}. This energy loss leaves the scattering molecule in an excited state and that is why SRS is called a non-parametric process.

In SRS the power changes on the laser sources are recorded. Therefore, usually either the stimulated Raman loss (SRL) on the pump laser or the stimulated Raman gain (SRG) on the probe laser can be measured (cf. Figure 2.2).

[1] Typical orders of magnitude for the higher order susceptibilities are $\chi^{(2)} \approx 10^{-12}\,\frac{\mathrm{m}}{\mathrm{V}}$ and $\chi^{(3)} \approx 10^{-24}\,\frac{\mathrm{m}^2}{\mathrm{V}^2}$ [7].

[2] The susceptibilities $\chi^{(2)}$ and $\chi^{(3)}$ are tensors which depend on the frequency of the applied field. The entries represent the polarization of the electrical fields. For instance, the third-order susceptibility $\chi^{(3)}$ is a fourth-rank tensor $\chi_{\mathrm{ijkl}}{}^{(3)}$ which consists of 81 elements. These entries contain e.g. the CARS effect [3], the Raman induced Kerr effect (RIKE) [8] and SRS [2].

[3] The probe light can thus also be called Stokes light, as it corresponds to the Stokes shift of the pump light.

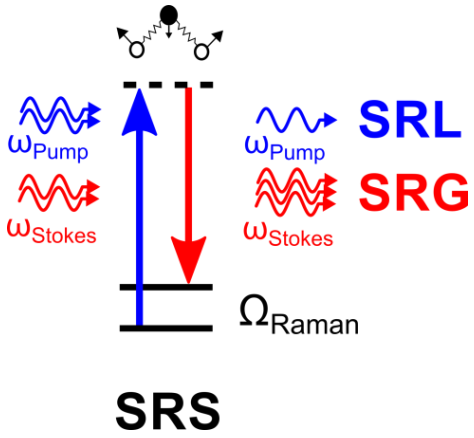

Figure 2.2: Energy diagram for stimulated Raman scattering (SRS). Two light sources, a Raman pump (blue) and a Raman probe (or Stokes, red), are incident on the molecule to stimulate a molecular excitation $\Omega_{Raman,}$ when the energy difference $\Delta\omega = \omega_{Pump} - \omega_{Stokes}$ corresponds to a Raman transition Ω_{Raman}. Then, pump photons are inelastically scattered to Stokes photons and stimulated Raman loss (SRL) on the pump power and stimulated Raman gain (SRG) on the Stokes power occurs.

For this case, where the FDML probe laser has moderate powers, it is convenient to use a strong pump laser and measure the SRG signal on the probe laser.[4] Following the derivation of Owyoung et al. [4], the SRG signal for a focused overlap can be calculated by:

$$\frac{dP_{Stokes}}{P_{Stokes}} = \frac{384\pi^4}{\lambda_{Pump}\lambda_{Stokes}cn}[Im\,\chi^{(3)}(-\omega_{Stokes}, \omega_{Stokes}, \omega_{Pump}, -\omega_{Pump})]P_{Pump}$$

where λ_{Pump} and λ_{Stokes} are the pump and probe wavelengths, c the speed of light, n the refractive index, P_{Pump} the pump power and Im $\chi^{(3)}$ the imaginary part of the third-order susceptibility for parallel polarized pump and Stokes light. This formula holds for tightly focused beams[5], where the sample interaction length contains the focal volume and the beam geometries for both beams are nearly identical.

It is to be noted, that the SRG signal scales linearly with the imaginary part of the third-order susceptibility Im $\chi^{(3)}_{iijj}$ and is thus free from nonresonant background, unlike in CARS where the nonresonant background obscures the signals and the spectra show a distorted lineshape [9].

The spectra obtained by SRS have readily interpretable Raman spectra, just like spontaneous Raman spectra, and are free from spectral distortions. Furthermore, the SRG signal scales linearly with the sample concentration, unlike quadratically in CARS, which

[4] As the SRL would scale with the probe laser power, which is about five orders of magnitude lower, it is more convenient to measure the SRG signal here. This gets obsolete if the pump and Stokes powers reach comparable values.

[5] In fact, in the case of tightly focused beams where the sample length includes several Rayleigh lengths the SRG is independent of the focus size.

makes quantitative measurements, like analysis of the sample constituents, easy and reliable (see also section 7.7).

3. SRS spectroscopy with rapidly wavelength swept lasers

The application of tunable lasers enables the measurement of SRS spectra by tuning the energy difference and thereby the Raman transition energy. This was shown already in 1977 by Owyoung et al. [4]. Nevertheless, the use of CW pump and CW probe lasers required long integration times on the lock-in amplifier, as the SRG effect was in the order of 10^{-5} and, furthermore, the tuning of the CW dye laser was comparatively slow. This thesis presents the application of a rapidly wavelength swept FDML laser as probe laser, which provides ultra-high sweep speeds. It is used for SRG measurements by choosing a quasi CW[6] approach. As the SRG signal scales linearly with the applied pump power, the pump laser is modulated to nanosecond pulses in order to obtain high instantaneous powers at moderate average powers, which enables SRG signals in the range of 10^{-2}.

The application of a wavelength swept laser, as shown in Figure 3.1, allows to address different Raman transitions simply by adjusting the relative timing between the pump pulses and the rapidly wavelength swept probe laser.

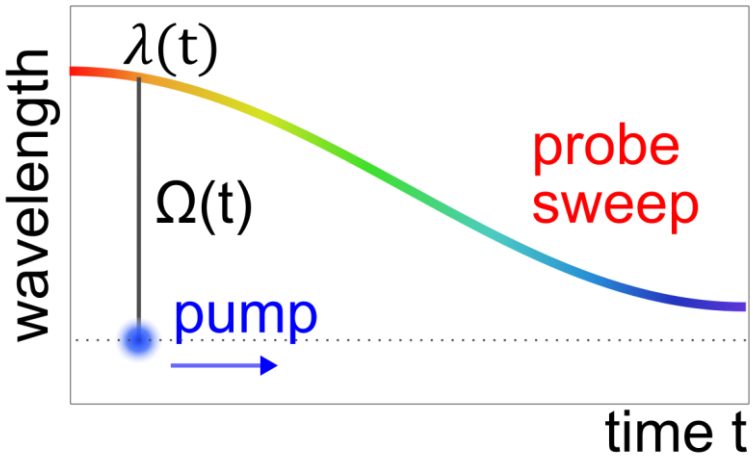

Figure 3.1: Illustration of pulsed SRG generation in combination with a wavelength swept laser. The wavelength sweep over time allows to tune the energy difference. The relative timing between the pump pulse and the sweep is used to probe different Raman transitions.

Therefore, the concept of time-encoded (TICO) Raman is introduced (Figure 3.2). This concept will be explained in more detail in chapter 6, but here the basic idea shall be outlined. The wavelength sweep of the rapidly swept laser is divided in *n* time intervals, which

[6] The term quasi CW is used here in the sense that nanosecond and longer pulses are used. The pump laser operates in the nanosecond regime and the probe laser is CW operated.

correspond to *n* different wavelength ranges. By addressing the different intervals individually with pump pulses and measuring the SRG signals, a Raman spectrum can be obtained. A great advantage of this approach is that the wavelength, and therefore the Raman transition, is encoded in time.

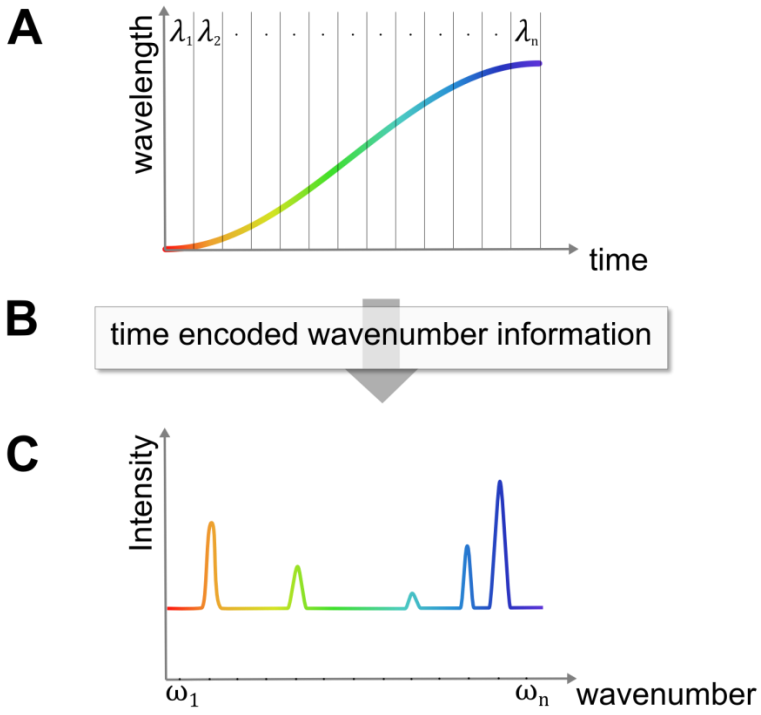

Figure 3.2: Acquisition of Raman spectra through the time-encoded (TICO) technique. **(A)** The sweep of the FDML Stokes laser is divided in a raster of *n* wavelengths. **(B)** The wavelengths correspond to unique time intervals of the sweep. **(C)** The measurement of SRG signals over time can be used to map the SRG signals to Raman transistions (wavenumber values ω).

The following chapters present the pump and probe lasers which enable the use of such a time-encoded SRS approach. Further, the TICO-concept, its' realization and the implementation into a fiber-based, electronically controlled system will be explained.

4. Pump-Laser

4.1. Master Oscillator Power Amplifier (MOPA) Setup

As described in chapter 1, the SRG signal scales linearly with the pump power. Therefore, the pump laser was modulated to short pulses with high instantaneous powers in order to maximize the SRG signal while keeping the average power on the sample low in order to avoid sample damage.

The pulse modulation in combination with the demand for flexible timing of the pump laser pulses relative to the FDML Stokes laser lead to the decision on a fiber Master Oscillator Power Amplifier (MOPA) design [10]. This design allows to freely synchronize the pump laser to other components by actively modulating the waveform on an electro-optical modulator (EOM). Furthermore, the light source is adjustable in power through the amplification stages and provides an alignment-free and flexible fiber-based setup.

With the flexible MOPA design, a manifold of repetition frequencies is possible, so the CW exposure can be adjusted to the optimal exposure level that the sample can withstand.

In the following, the pump laser source is presented. Further information regarding model numbers, results and efficiencies can be found in the diploma thesis by Matthias Eibl [11] and the manuscripts on the pump light source [12, 13].

The setup of the light source is shown in Figure 4.1. As a seed light source a semiconductor laser diode at 1064 nm in a fiber pigtailed butterfly housing was used. The external fiber Bragg grating makes it a narrowband seed light source (FWHM 30 MHz, Lumics LU1064M150). The pulses are generated in two steps. First, the 1064 nm diode current is pre-modulate to yield ~30 ns pulses - this way the following fiber amplifier stages are not de-excited between the pulses. The pre-modulation is necessary, as the EOM has only a limited extinction ratio, typically ~30dB. As the duty cycle is also in this range (1000-10.000), this means that the leaking light power would become comparable if not bigger than the pulse light power, leading to a loss in fiber amplifier efficiency. So the pre-modulation increases the contrast of the pump pulses.

After the pre-modulation, the light is modulated by a fiber coupled EOM with a maximum bandwidth of 12 GHz (Photline, NIR-MX-LN-10). The electrical pulses to the EOM are provided by a homebuilt electronic pulse generator board (EPB). This electronic setup is shown in Figure 4.2. The pulse length of the EPB can be digitally adjusted from 440 ps up to 10 ns in 10 ps increments on-the-fly on a personal computer (cf. Figure 4.3). Once the optical pulses are created on the EOM, they are amplified by ytterbium doped fiber amplifiers (YDFA).

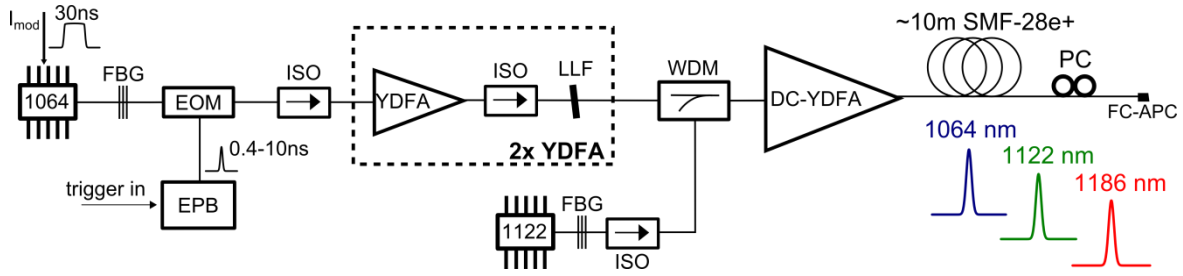

Figure 4.1: The setup of the multi-color fiber MOPA. The seed diode at 1064 nm has a fiber bragg grating (FBG) installed to ensure a narrow linewidth operation. The short optical pulses are actively modulated with an EOM, but also the 1064nm laser diode is pre-modulated to 30 ns (see text). The short pulses are provided by an electronic pulse board (EPB) which allows digitally choosing the pulse length. ISO: isolator, YDFA: ytterbium-doped fiber amplifier (two stages), LLF: laser line filter, WDM: wavelength devision multiplexer, DC-YDFA: double-clad YDFA, PC: polarization controller, FC-APC: fiber coupler angle-polished connector.

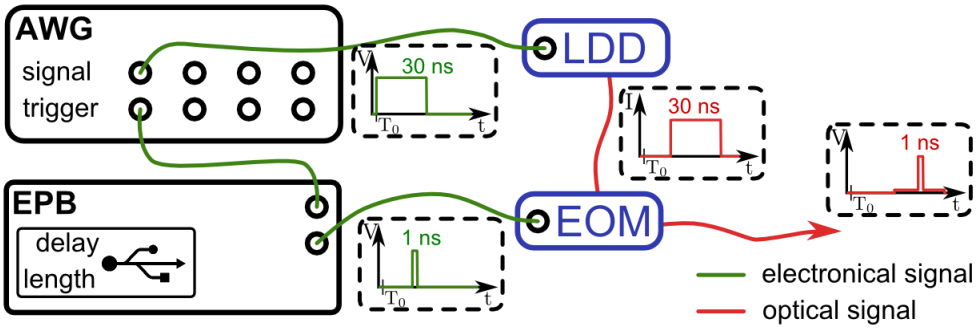

Figure 4.2: The electronic setup for the fiber MOPA. The arbitrary waveform generator (AWG) pre-modulates the laser diode driver (LDD) to ~30 ns optical pulses. A second channel is used to trigger the electronic pulse board (EPB), on which the pulse length and the delay can be set digitally via the USB port. Typically 1 ns pulses are modulated via the electro-optical modulator (EOM).

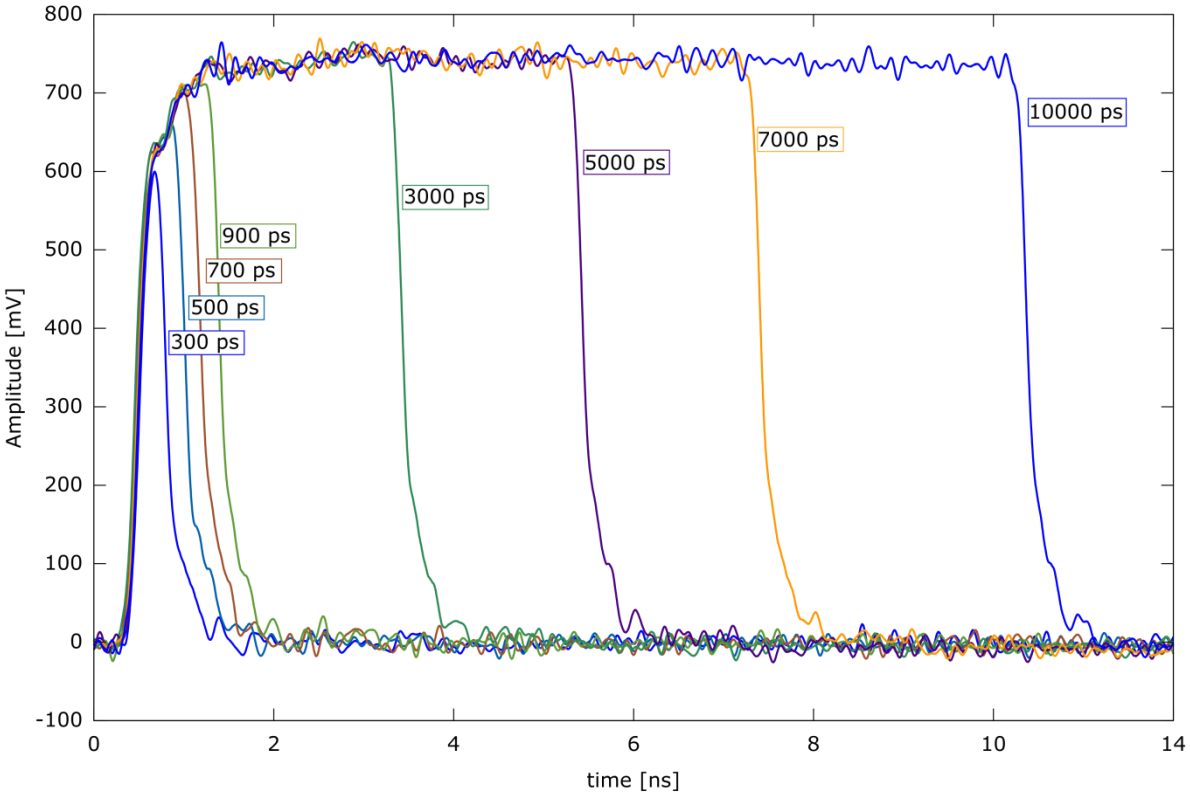

Figure 4.3: Temporal characteristics of the electronical pulses from the EPB, used to modulate the EOM. The pulse length can be digitally adjusted from 400 ps up to 10 ns in 10 ps increments. Shown are only few examples for better visibility.

The following YDFA stages (see Figure 4.1, dashed box) consist of ytterbium doped single-mode fiber, core pumped by semiconductor laser diodes at 976 nm, i.e. at the absorption maximum of ytterbium. The pump light is coupled in counter propagating direction by fiber wavelength division multiplexers (WDM). The pump diodes are protected by fiber coupled isolators (indicated by arrows in Figure 4.1). The 1064 nm laser diode provides up to 150 mW of CW output power. After the EOM the power level of the pulses is about 20 mW. The instantaneous power is amplified by the first YDFA to about 10 W (at usually 1 ns pulse length and 50 kHz repetition rate). The power of the 976 nm pump diode in the first YDFA is 450 mW. The second stage is set up identically to the first amplifier stage. After each stage a free space laser line filter is employed, serving to filter out the unwanted amplified spontaneous emission (ASE) from the ytterbium doped fiber. The filter window of 3 nm around 1064 nm effectively filters the ASE background, which peaks around 1030 nm.

The third YDFA is a double-clad YDFA (DC-YDFA) which is cladding pumped by a 976 nm multimode pump diode, providing up to 9 W of pump power. A major advantage of using a cladding pump design is the available pump diode power on the market for multimode (MM) diodes and the relatively low price per Watt compared to single-mode (SM) diodes. The absorption is reduced as compared to a core pumped setup, but cladding geometries can

be optimized to obtain higher core absorption. Also, the often larger core diameter lowers the intensity quadratically which can be harnessed to omit unwanted non-linear effects.

As coupler for the MM pump diodes, a (2+1)x1 coupler was used, with the pump light traveling in counter propagating direction to the signal. About 3 meters of DC ytterbium fiber (10 µm core diameter, 105 µm cladding diameter) were used, which were fusion spliced to the coupler. The splices could not be protected by regular splice protector sleeves, as a leakage of the cladding pump light was observed, which was due to the higher refractive index of the standard protection sleeves. Therefore, the splices were suspended in air in order to use the low refractive index of the surrounding air for total internal reflection in the cladding.

An absorption dependence on the bending and layout geometry of the DC-fiber (LIEKKI, Yb1200-10/125DC) was observed. Especially the seed light was observed to leak out of the core in significant amounts when moderate bending (~10 cm bending radius) was applied.

After each of the three YDFA stages tap couplers (99:1 ratio) were installed to monitor the power levels. Additionally, fiber polarization controllers were installed after the DC-YDFA in order to control the output polarization of the multi-color MOPA.

To the signal output of the (2+1)x1-coupler about 5 meters of SMF-28e+ fiber were fusion-spliced and after the fiber a 99/1 tap coupler installed. The SMF-28e+ fiber was found to maintain the single-mode profile of the 1064 nm light [14]. The 99 percent output of the coupler had an FC/APC fiber connector which was used for the collimator in the bulk optic setup. Also a fiber polarization controller was inserted to control the pump polarization in the setup.

4.2. Raman shifter

The fiber after the DC-YDFA was used as a beam delivery fiber to the bulk optic setup but also as a Raman-shifter to extend the TICO-Raman coverage (see Figure 6.8). For clarity, it is important to note that this Raman process in the fiber MOPA is only to shift the output wavelength of the pump laser and is independent of the SRS effect measured in combination with the FDML laser.

Glass fibers provide optimal conditions to shift the excitation wavelength via the Raman gain of fused silica [15-17]. This is particularly useful because of the small mode field diameter in SMF fibers and the long interaction lengths. The broadband gain of fused silica (Figure 4.4) can help to extend the spectral coverage of the laser. In order to achieve narrowband shifting, the Raman scattering process was stimulated by a seed light. Therefore, a Raman seed light source was inserted after the second YDFA. This seed was provided by a narrowband laser diode at 1122 nm (Innolume, LD-1122-FBG-400). This wavelength corresponds to a Raman shift of ~486 cm^{-1} (corresponding to the energy difference between 1064 nm and 1122 nm). This shift is at the far end of the maximum gain of fused silica [16]

(cf. Figure 4.4). The seed light at 1122 nm is inserted before the final, high power amplification stage which was found to provide the highest signal-to-noise ratio for the narrowband SRS shifting compared to the broad spontaneous Raman shifting. The high Raman conversion efficiencies are possible due to the long interaction length together with the small mode field diameter in the single-mode fiber. In Figure 4.5, it can be seen that most of the power was transferred from 1064 nm to 1122 nm, as the 1122 nm peak is now 8 dB (i.e. 6-times) higher than the 1064 nm light.

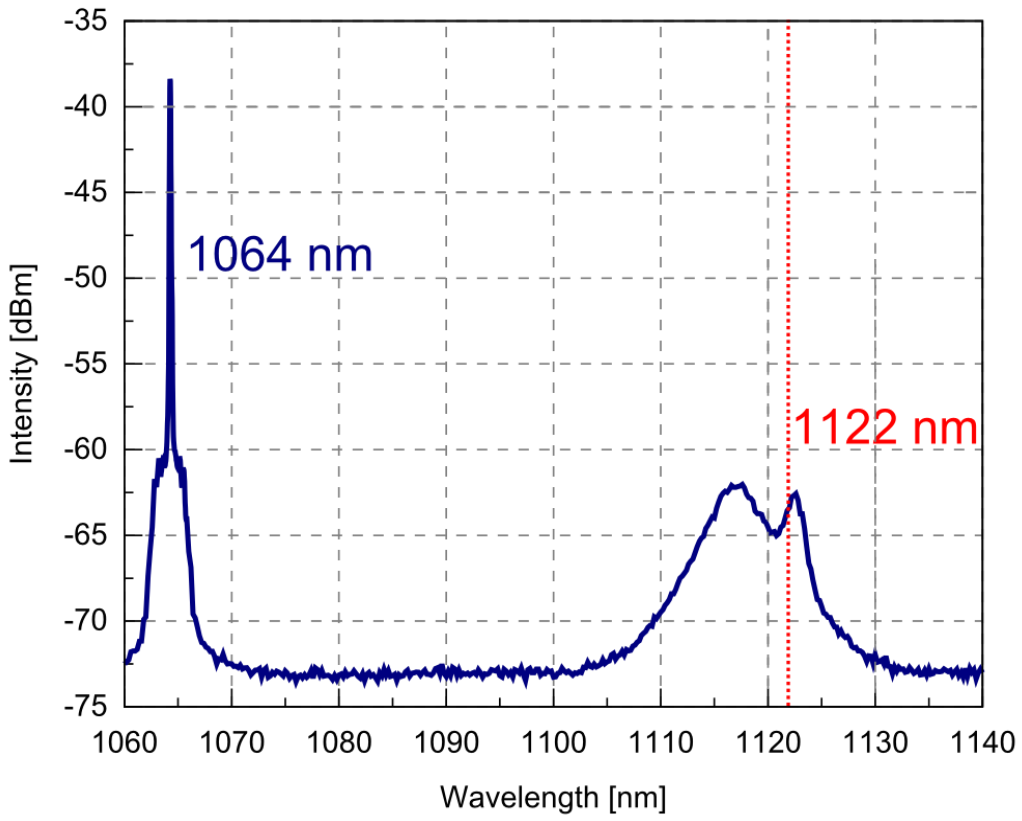

Figure 4.4: Experimentally measured spontaneous Raman gain spectrum of the SMF-28e+ fused silica fiber and the 1064 nm pump. The seed laser diode for Raman shifting at 1122 nm lies in the far, high Raman gain.

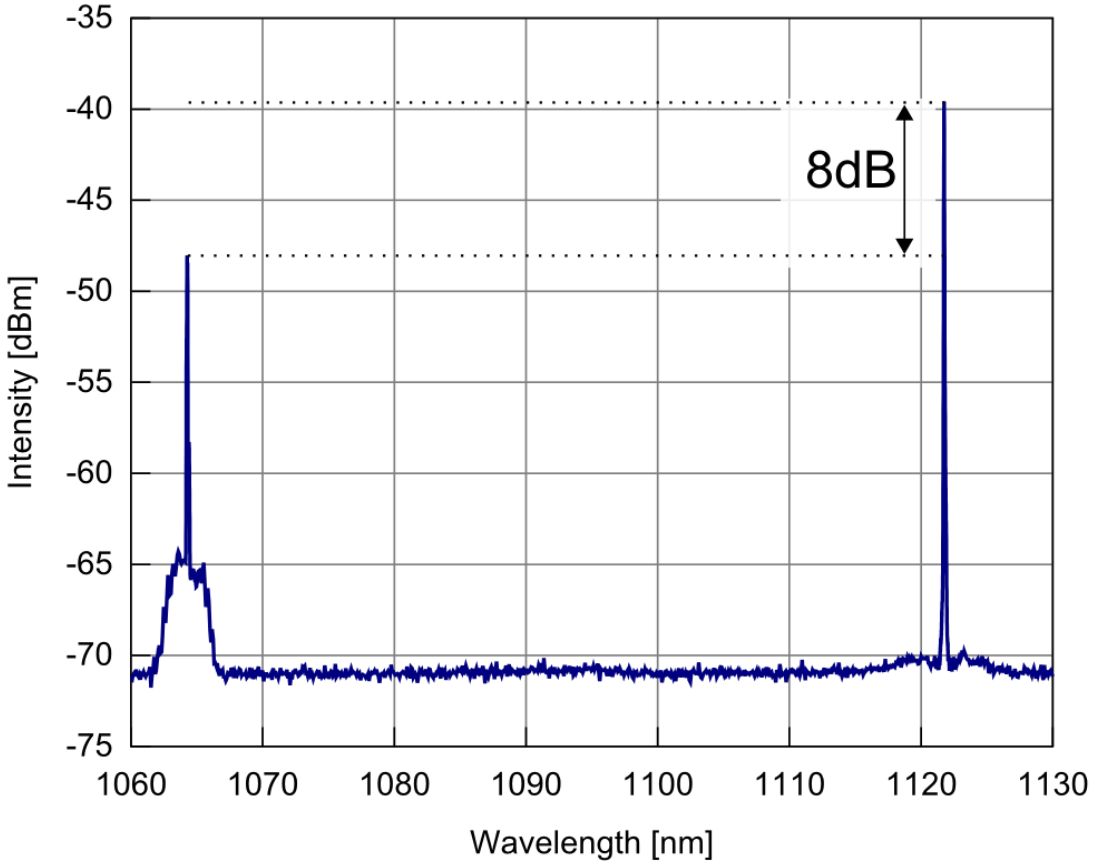

Figure 4.5: Output spectrum of the pump laser when most of the power is Raman shifted from the 1064 nm to the 1122 nm band.

Besides the high efficiency, another advantage of the Raman shifter setup is that both wavelengths exit the same fiber. Conveniently, this shifting process is controlled electronically by switching the 1122 nm diode and adjusting the power in the DC-YDFA. In many fiber lasers, SRS is an unwanted nonlinear effect limiting the maximum obtainable power [18]. In this laser, the Raman effect is instead harnessed to shift the output to a new wavelength. This enables the coverage of more Raman transitional energies to be probed by the FDML Stokes laser (see also Figure 6.8).

Another effect that often limits the maximum power is stimulated Brillouin scattering (SBS) [19], where the photons are scattered by acoustic phonons as opposed to optical phonons in SRS. In single-mode fibers, the acoustic phonon frequency depends on the acoustic velocity and the refractive index of the fiber material. For the employed SMF-28e+ telecom fiber and the 1064 nm wavelength, the SBS shift is at ~16.4 GHz with ~50 MHz FWHM linewidth [18, 20]. An experimental observation of SBS in the backward direction can be seen as a peak at lower frequency in the output spectrum in Figure 4.6. This scattering frequency is observed twice when recorded in forward direction. A common practice to suppress SBS is to broaden the linewidth of the laser beyond the 50 MHz linewidth of the Brioullin phonons, e.g. by active spectral modulation [10]. In the presented MOPA laser, the

pulse length effectively broadens the spectrum, as will be explained here. The 1064 nm seed laser diode (Lumics LD1064M150) has a linewidth specification of <30 MHz. This linewidth corresponds to a time-bandwidth-limited pulse length of 14.7 ns (assuming Gaussian shape). If the pulse length is lowered, the bandwidth increases. This means, a pulse duration of 2.5 ns corresponds to approximately 176 MHz linewidth. This is already much broader than the SBS linewidth. As the SBS gain depends on the spectral width and the interaction length [19], wherein the latter also scales linearly with the pulse duration, lowering the pulse duration leads to a quadratic decrease in SBS gain. This was confirmed experimentally and a quadratic dependence of the SBS threshold on the pulse length was measured [11]. In all, the pulse length can be shortened as an efficient measure to circumvent SBS limitation on the pump power.

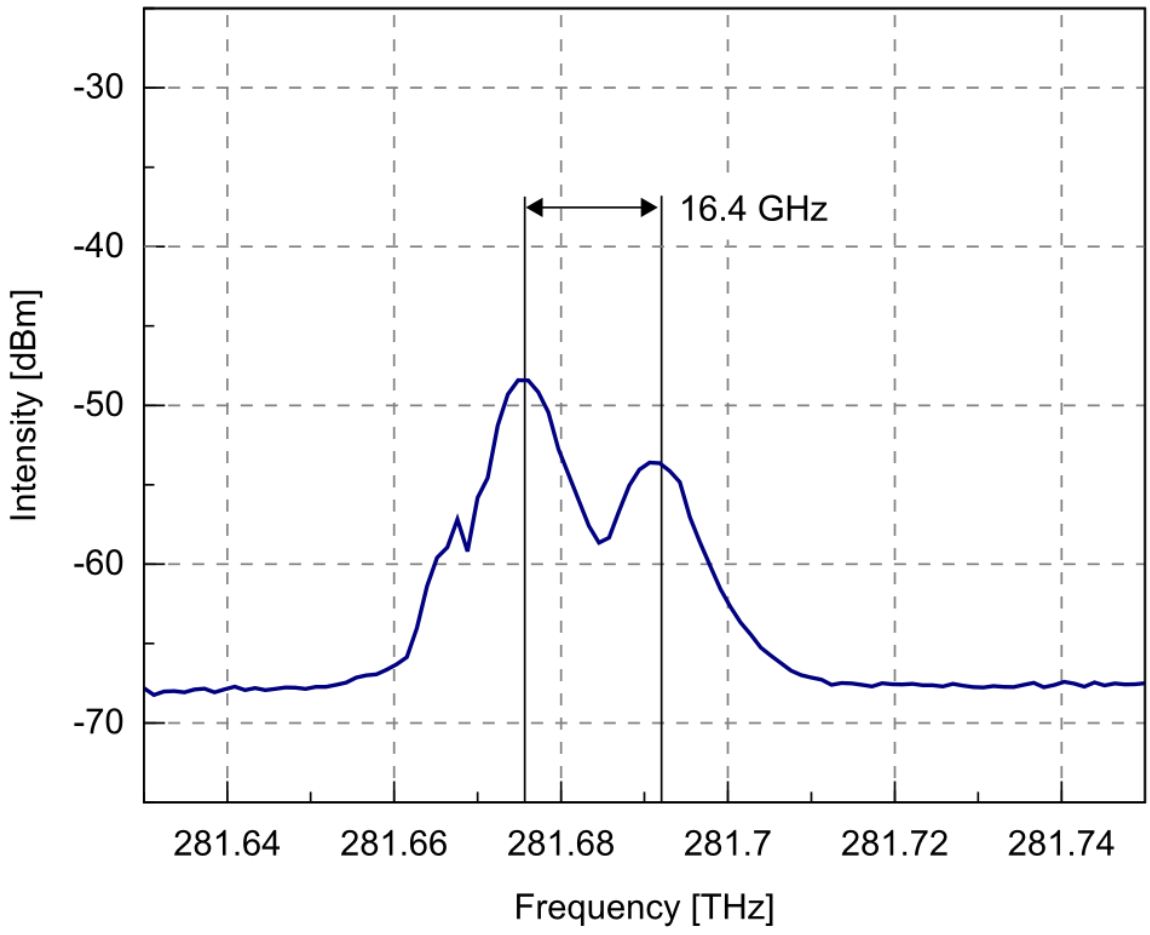

Figure 4.6: Stimulated Brioullin scattering of a 2.5 ns pulse in an SMF-28e+ fiber recorded in backward direction.

4.3. Cascaded Raman-shifting and four-wave mixing

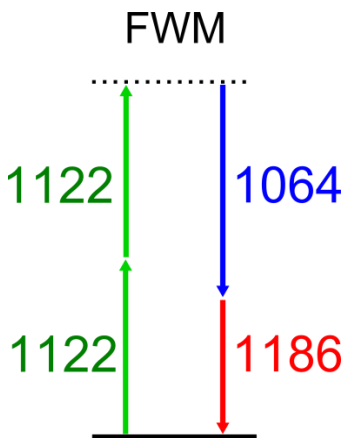

Figure 4.7: Four-Wave mixing (FWM) is a parametric process where two pump waves are converted into a signal and an idler wave. In the here depicted degenerate case, two 1122 nm waves are converted into one 1064 nm and one 1186 nm wave.

During the experiments on the SRS shifting to 1122 nm it was found that the maximum obtainable power at 1122 nm was limited to a certain value after which power was lost to a cascaded Raman shift. Surprisingly, this cascaded Raman shift was found to be narrowband (cf. Figure 4.9). Usually, one would expect the bandwidth of the cascaded Raman line to have the characteristics of the Raman transition in fused silica [21-23], i.e. the Raman bandwidth as measured in Figure 4.4. Instead, the line at 1186 nm was found to be of narrowband character with ~50 pm FWHM (see Figure 4.9). The resolution of the optical spectrum analyzer (OSA) was set at highest resolution (20 pm). As is evident from Figure 4.9, the linewidth of the 1186 nm line is roughly equal to the linewidth of the 1064 nm and the 1186 nm lines. This indicates that in the presented light source, the linewidth is preserved throughout the cascaded Raman shifting process. Another interesting observation is that the three peaks are equidistant in frequency (14.4 THz).

The current model is that this narrowband feature of the 1186 nm cascaded Raman line is a combined effect of cascaded Raman shifting and four-wave mixing (FWM). Since a Raman shift from 1122 nm would be broad (see Figure 4.4), spontaneous Raman scattering cannot account for its narrowband nature. Usually in cascaded Raman shifters the narrowband structure is achieved by designated resonators [17]. Here, no resonators are used. The whole shifting process is obtained in a single-pass setup. Furthermore, no seed light at 1186 nm is inserted. To analyze the effect more closely, the condition for FWM is considered. This condition is twofold: First, since it is a parametric process (see Figure 4.7), the energy needs to be conserved. As can be seen from Figure 4.7, this holds $2E_{1122} = E_{1064} + E_{1186}$. Using the values from Figure 4.9, this leads to an idler wavelength of 1185.8 nm. Second, the momentum needs to be conserved, leading to the well known phase-matching condition [24]:

$$\Delta k = \frac{2n_{1122}\omega_{1122}}{c} - \frac{n_{1064}\omega_{1064}}{c} - \frac{n_{1186}\omega_{1186}}{c}$$

Δk is called the phase mismatch and should be zero for momentum conservation.[7] Taking the refractive indices from the Sellmeier equation for GeO_2-doped fused silica [25], one finds $\Delta k \cong -87\frac{1}{m}$ for this setup. This means, that this configuration is not perfectly phase matched. The phase mismatch corresponds to a coherence length $L_{coh} = \frac{\pi}{\Delta k}$ of roughly 3 cm. After this coherence length, the generated FWM light has a phase shift of π with respect to the initial FWM light, which would lead to destructive interference. Thus, it is believed that the 3 cm coherence length is sufficient to seed the narrowband cascaded SRS effect observed. This explains the observed narrowband line at 1186 nm (see Figure 4.8). The high amplification of the SRS together with the FWM effect produce high power 1186 nm pulses with narrowband characteristics. An experimental spectrum is shown in Figure 4.9. Also visible is the occurrence of spontaneous broadband Raman scattering, visible in the pedestals below the 1186 nm peak. This pedestal gives an integrated energy of roughly 30% of the energy in the narrowband peak. When considering the ratio of spontaneous Raman to SRS for the maximum 1122 nm generation (Figure 4.5), one finds by integration that only ~2% of the energy lies in the pedestal.

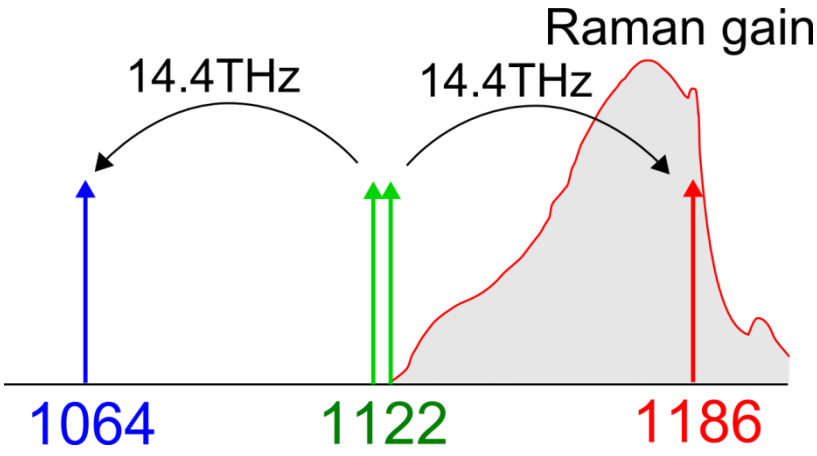

Figure 4.8: The combination of FWM followed by SRS amplification in the SMF-28e+ fiber can lead to a narrowband amplification of the 1186 nm light, as was experimentally observed.

A further indicator for the model of the combined FWM/SRS effect is the appearance of a subsequent cascaded Raman shift at 1257 nm (Figure 4.10) which is again of narrowband character. Although this light at 1257 nm is at low power levels, it is clear that it is sharper than what would be expected by the broad spontaneous Raman linewidth. In a preliminary test

[7] The factor $2\gamma P$ for the contribution of self-phase modulation was neglected, as it is about 2 orders of magnitude smaller than the phase mismatch. If perfect phase-matching is to be achieved, the wavevector mismatch should be equal to this factor. Also, a waveguide dispersion contribution was neglected since all wavelengths travel with a single-mode Gaussian in the SMF28e+ fiber.

with longer fibers, this peak at 1257 nm could not be brought to higher power levels. Instead of the narrowband peak at 1257 nm, already the 1185 nm band showed a broad character upon higher amplification. This needs to be investigated in more detailed upon considering a broader range of parameters in future experiments.

The shifted pulses at 1186 nm showed high temporal, spectral and spatial purity. This is demonstrated in a recorded SRS spectrum of benzene around its narrowband transition at 992 cm^{-1} (see Figure 7.7). In order to create such a high quality spectrum, the spatial overlap with the probe beams is critical. Furthermore, the spectral width of the 1186 nm light needs to be narrower or comparable to the spectral width of the Raman spectrum (~ 3 cm^{-1} or 0.4 nm at 1186 nm, cf. Figure 4.9). Lastly, the temporal overlap for the nanosecond pulses and the synchronized detection is important. The spectrum in Figure 7.7 thus proves the quality of the presented laser light at 1186 nm.

The presented pump laser is highly flexible in terms of pulse repetition rate, power levels, wavelengths and beam delivery. This flexibility is an important step for the stimulated Raman scattering setup for use with the rapidly wavelength swept FDML lasers. These lasers serve as the Stokes laser and will be presented in detail in the next chapter.

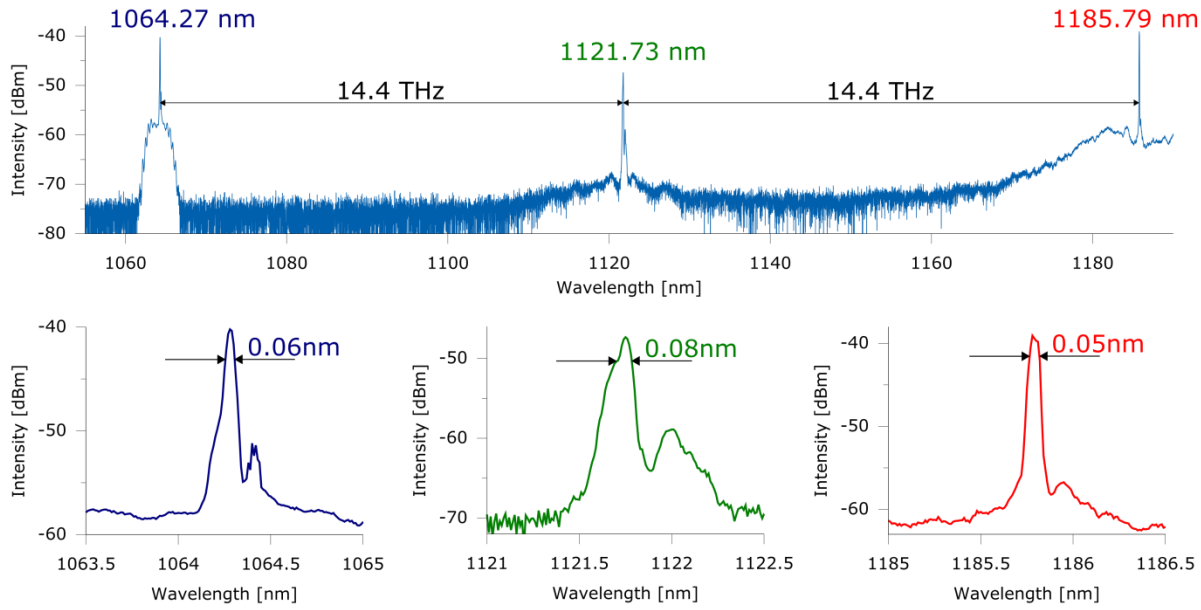

Figure 4.9: The spectral output of the multi-color fiber MOPA. Via cascaded Raman shift the pulses can be shifted from 1064 nm and 1122 nm to 1186 nm. This occurs without designated resonators and in a single pass configuration. Some pedestal underground can be observed below the narrow peaks, probably resulting from ytterbium ASE below the 1064 nm peak, spontaneous Raman scattering for the cascaded shifts and due to SBS. However it is to be noted that the signal levels are on a logarithmic scale so most of the power lies indeed in the narrowband peaks.

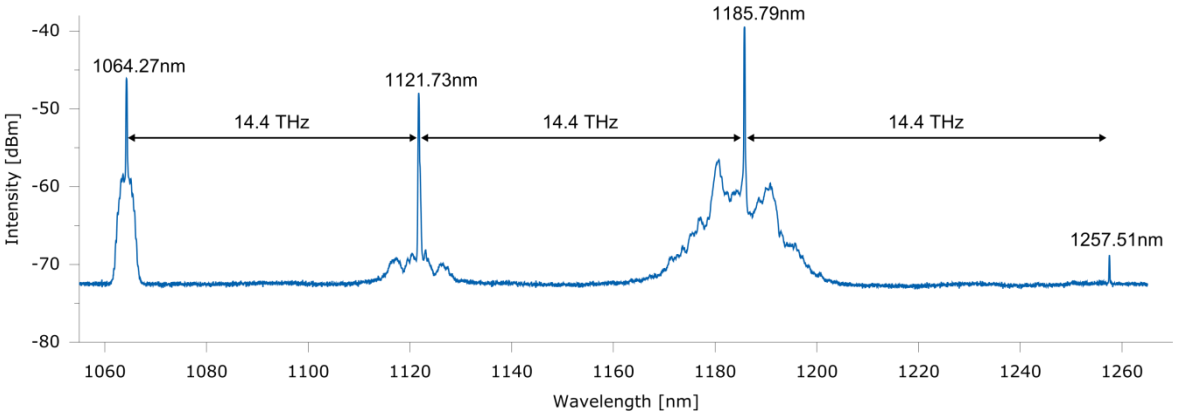

Figure 4.10: Upon higher amplification of the fiber MOPA, the wavelength shift can be extended even to 1257 nm, the third order cascaded Raman shift from 1064 nm. This peak at 1257 nm is of narrowband nature, narrower than what would be expected by spontaneous Raman scattering. This spectrum is the result of a resonatorless, single-pass amplification in the single-mode fiber.

The typical instantaneous power levels of the multi-color MOPA were up to 1.6 kW at 1064 nm and about 720 W at 1122 nm. These powers depend on the fiber lengths, i.e. the Raman scattering interaction length, and were limited by the onset of spontaneous Raman scattering. These maximum powers may be increased by optimizing the fiber lengths to the desired power level. In fact, a 50/50 coupler was inserted before the DC-YDFA to add a second, identical DC-YDFA to be used as a shifting stage for another desired output wavelength (see Figure 4.11). This way, the interaction length on this second branch can be optimized for the Raman shift to e.g. 1186 nm, requiring a longer interaction length (~10 m), while the first branch is optimized for e.g. 1064 nm and 1122 nm pump light (~6 m). Even with only half the 1064 nm seed light entering the two DC-YDFAs, no decreases in output powers were observed. The only drawback is that, in this configuration, two fiber couplers are used for the different output wavelengths instead of only one fiber. This can then be compensated for by recombining the beams after collimation on dichroic filters.

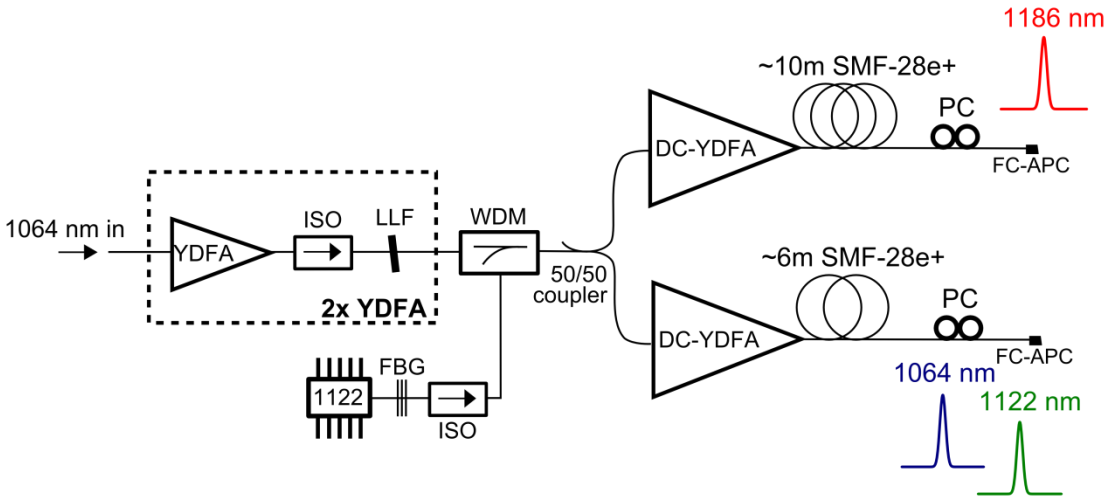

Figure 4.11: Possibility of creating a two-branched output, where one branch is used for maximal 1064 nm and 1122 nm light generation and the second branch for maximum 1186 nm generation.

5. FDML-Laser

As Raman probe laser a rapidly wavelength swept Fourier-domain mode-locked (FDML) [5] laser is used. This kind of laser was originally developed for the use in optical coherence tomography (OCT) [26]. In swept source OCT [27-31], the rapid wavelength sweeps are used to generate a beat signal, where the beat frequency $\Delta\nu$ is a function of the pathway difference Δz (or equivalently a time delay Δt) in an interferometer. Thus, a swept source laser with a known $\frac{\Delta\nu}{\Delta t}$ or $\frac{d\nu}{dt}$ can be used to calculate the depth profile due to scattering of light by analyzing the Fourier transform[8] of the beat frequencies. These lasers offer a broad sweep (~150 nm) in the Near-infrared at high repetition rates (MHz). This sweep range corresponds to up to 1000 cm^{-1}, making it an ideal light source for the development of a fast stimulated Raman spectroscopy system. To this end, two FDML lasers around 1310 nm and 1550 nm were built. Both could be adjusted to work either at 50 kHz repetition rate or 400 kHz[9] by interchanging the tunable filter and the optical fiber delay line. The schematic setup is shown in Figure 5.1. The ring laser setup comprises a semiconductor optical amplifier (SOA) as gain medium, optical isolators to ensure uni-directional lasing, the swept fiber Fabry-Pérot filter and the optical delay line consisting of several hundred meters of single-mode fiber. A photography of such an FDML laser is shown in Figure 5.2. This long delay line enables the storage of the entire sweep in the cavity, so that the cavity round-trip time corresponds to the sweep time of the swept Fabry-Pérot filter. This way the light in the cavity does not need to build up every time the wavelength is changed, like in short cavity lasers, but instead conducts multiple round trips in the FDML laser. This leads to a coherent lasing operation with good coherence length and low intensity noise [33]. This intensity noise is important, as the SRS signal is recorded as a power change on the FDML laser (SRG measurements).

[8] In SS-OCT with an FDML laser, a Hilbert transformation is used, which also extracts the phase of the fringes. This phase is used to resample the fringe signals, as the sinusoidal wavelength sweep does not provide a linear slope in $\frac{d\nu}{dt}$, so the the phase reconstruction can be used to recalibrate the samples of the fringes to obtain a linear $\frac{d\nu}{dt}$ slope.

[9] One period covers two times the sweep range. One sweep goes from long wavelength (red) to smaller wavelength (blue) and the next from blue to red. This can also be made unidirectional by buffering [32].

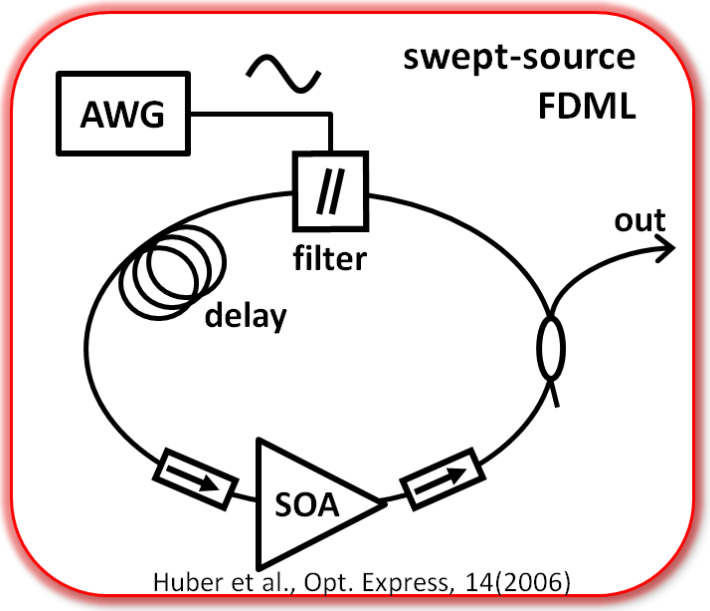

Figure 5.1: Schematic setup of the FDML laser. The arbitrary waveform generator (AWG) drives the optical filter, used to sweep the laser wavelength. The semiconductor optical amplifier (SOA) serves as the gain medium for laser operation. The entire setup is fiber-based.

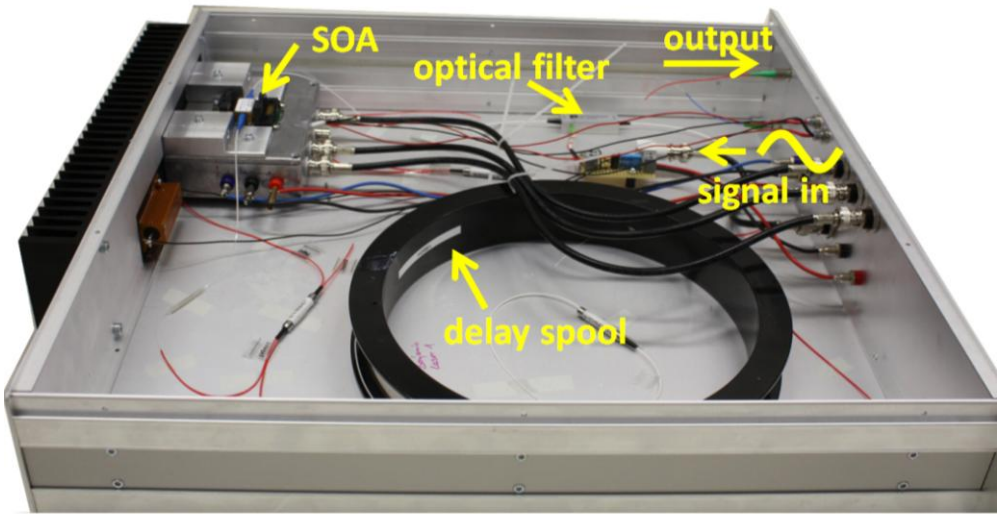

Figure 5.2: Photography of an FDML laser. The whole laser fits in a 2 height unit 19 inch case.

5.1. Noise characteristics

An important prerequisite for the FDML laser as a SRG probe laser is a low relative intensity noise. As the SRG intensity change on the FDML laser are detected, it is important to be able to measure down to the shot noise limit. This was achieved in the presented setup.

If the driving frequency of the filter inside the FDML is adjusted carefully to the resonance frequency imposed by the cavity length, the relative intensity noise can be as low as 0.2 percent at 100 MHz detection bandwidth [33]. By additionally employing a differential balanced detector this can be further reduced drastically[10]. A last measure to lower the relative intensity noise down to the shot noise limit was the development of a digital balancing step. This is explained in more detail in the following chapter. By the combination of all these measures, the shot noise limit for the 2x2 mW FDML power was reached. The shot noise corresponding voltage can be calculated by $\sigma_V = \sqrt{2 \cdot e \cdot I \cdot \Delta B} \cdot TIG$, where e is the elementary charge, I is the photocurrent, ΔB is the detection bandwidth and TIG is the gain of the transimpedance amplifier. In this case, using the detection bandwidth of 350 MHz, a photocurrent of 2x2 mA[11] and a transimpedance gain of 4000 V/A, the shot noise voltage can be calculated to: $\sigma_V = \sqrt{2 \cdot 1.6022 \cdot 10^{-19} \cdot 2 \cdot 2 \cdot 10^{-3} \cdot 350 \cdot 10^{6}} \cdot 4000\,V = 2.68$ mV. This value needs to be multiplied by $\sqrt{2}$, giving 3.79 mV, since two measurement values are subtracted in the digital balancing step whereupon the noise adds quadratically. This gives a relative shot noise level of 4.7×10^{-4}, as the 2 mW Stokes power would result in a DC-coupled detector voltage of 8000 mV. The noise level of the detection did match this level which means that without averaging, intensity changes on the probe laser as low as 4.7×10^{-4} can be measured with the system.

This is depicted schematically in Figure 5.3. The upper graphic shows the sweep characteristics of the FDML laser with a sinusoidal wavelength sweep over time. The lower graphic depicts that this detection setup is able to detect signals as low as 4.7×10^{-4} on the CW output of the swept laser.

[10] Typical values for differential balanced detectors are >20 dB common mode noise rejection.

[11] With responsitivity of 1 A/W for the InGaAs detectors around 1500 nm and the factor of 2 for the balanced detection.

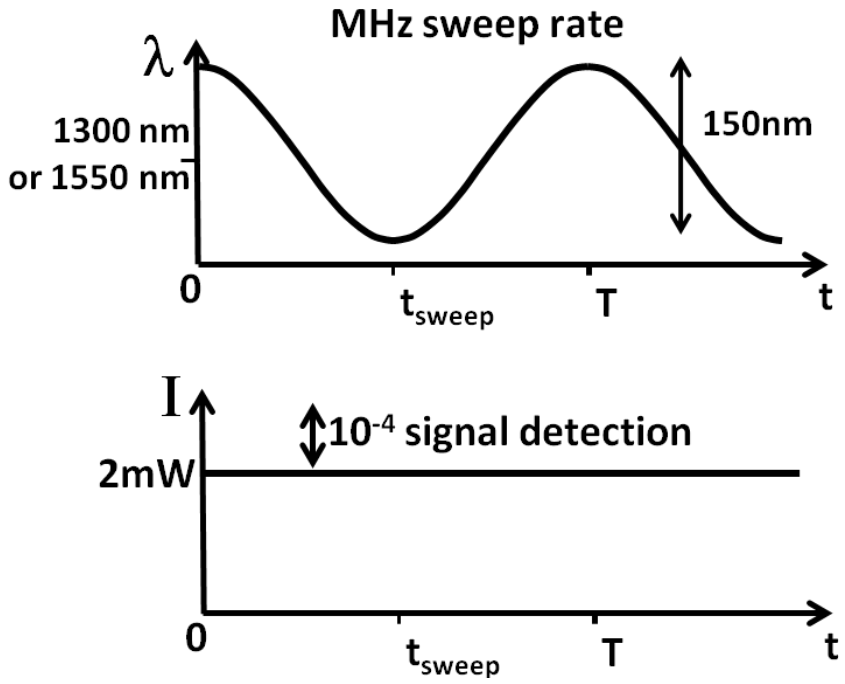

Figure 5.3: Simplified visualization of the output of the FDML laser. Upper graph: The sinusoidal sweep in wavelength covers about 150 nm in half a period T. Thus a sweep time t_{sweep} is assigned as half this period, effectively covering one wavelength span. Lower graph: the idealized intensity output: a CW with low intensity noise. This low noise in combination with an elaborate, two step balanced detection makes the measurement of shot noise limited intensity changes (e.g. due to SRG) as low as 4.7×10^{-4}possible (see text).

5.2. Spectral and temporal output

A typical output spectrum of the used FDML laser is shown in Figure 5.4. The OSA used for recording the span of the FDML laser is to slow to resolve the FDML sweep in time. An average over many sweeps is recorded by the OSA. This also leads to the commonly seen "bull horn" structure on the output spectrum (see Figure 5.6), as the turning points of the cosine sweeps result in a longer exposure time in the OSA, resulting in a seemingly higher power value. Note that in Figure 5.4 only the lower wavelength "horn" shows up, as the higher wavelength "horn" lies outside of the SOA gain bandwidth and is thus suppressed. Around 1370 nm faint water absorption lines are visible resulting from the higher-harmonics of the water vapor inside the OSA.

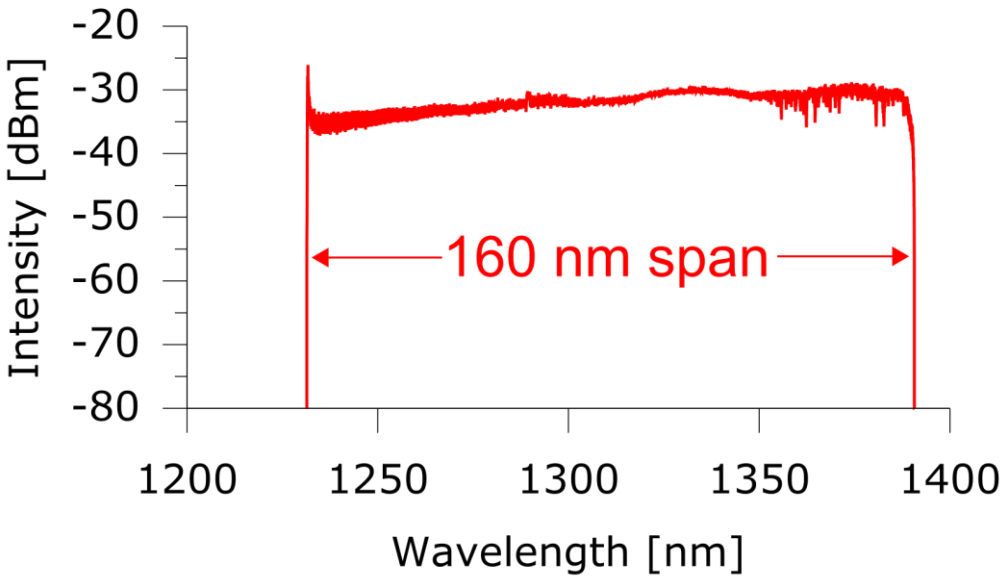

Figure 5.4: Typical output spectrum of the employed FDML laser around 1310 nm measured with an optical spectrum analyzer. High-harmonic water absorption bands from water vapor in the OSA are visible around 1370 nm.

A typical temporal output is shown in Figure 5.5. For the TICO-Raman recordings this temporal sweep output is recorded once. Therefore, a monitor port of a tap coupler is plugged in a DC-coupled photodiode and digitized. Subsequently, it is multiplied by the tap-coupler ratio and fitted with a b-spline fit of 2nd degree. This fit is used later for division in order to represent the SRG signal as intensity change $\frac{dP_{probe}}{P_{Probe}}$ on the probe laser (see section 4.1). A smoothened curve is preferable in order to not impose any ripples on the recorded spectra. The small deviations of the fit are negligible since they are about four orders of magnitude lower than the measured SRG signals, but can be improved by using other fit methods like higher order spline fits or Savitzky-Golay filtering.

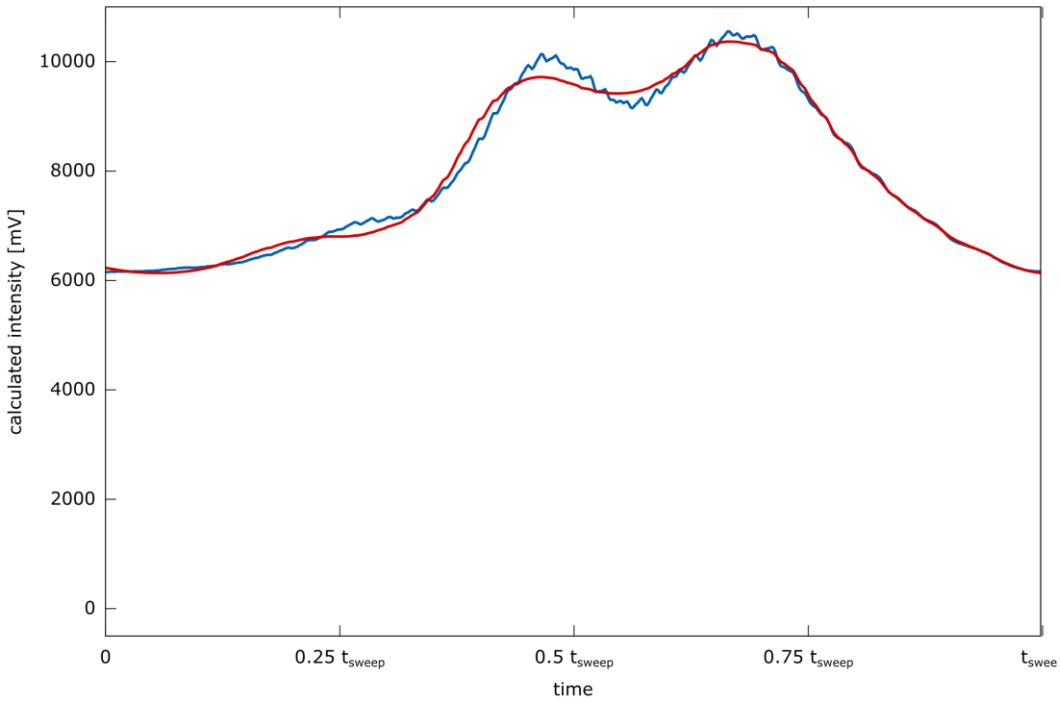

Figure 5.5: Temporal output of the intensity of a typical FDML sweep. The curve is first measured on a DC-coupled photodiode with a tap-coupler. Then, the intensity in the SRS setup is calculated from the tap coupler ratio. This trace is then used to express the SRG signals as relative intensity changes. The fit (red) is obtained by a b-spline fit. This fitted curve is used to smoothen the DC-trace in order to not impose any ripples on the resulting SRG spectra after division.

5.3. Time-to-wavelength encoding

As described earlier, the FDML laser incorporates a fiber Fabry-Pérot filter to tune the wavelength. An electronic sine wave drives the resonator length and thereby effectively tunes the resonant wavelength. Therefore, the FDML laser also ought to have a sinusoidal sweep in wavelength [12]:

$$\lambda_{FDML}(t) = \lambda_{center} + \frac{\lambda_{span}}{2} \cos\left(2\,\pi\frac{t}{T} + \Phi\right)$$

where λ_{center} is the center wavelength, λ_{span} the span of the sweep, T the period of the FDML laser and Φ the initial phase of the Fabry-Pérot filter, which can electronically be set to zero. This well-defined sweep can be used to calculate the wavelength trace over time by extracting the center wavelength and the span from the OSA spectrum (see also the SI of [12] for more information).

Usually in FDML-based OCT, the sweep characteristic used to reference the measurements is a time trace of a reference fringe pattern. A time-delay is introduced in a Michelson interferometer and the fringes are recorded. From this the phase information and

the frequency over time trace is extracted, which is then used for resampling. Other methods use more elaborate driving electronics in order to produce a linear sweep in frequency [34].

Since in SRS the phase is irrelevant and only the wavelength over time information is of importance, it was tested whether this information can be obtained in a simpler and faster manner. This idea was found to work very accurately. First, a spectrum of the FDML output is recorded with the OSA (Figure 5.6). The spectral information, i.e. the central wavelength and the sweep span range is recorded in the measurement software in LabVIEW. Then a cosine wave is modeled in the software in order to assign a wavelength to each sample of the synchronized ADC detection (cf. Figure 5.7). This time-to-wavelength encoding is effectively a mapping of wavelength to the time of the sweep. This is possible, on the one hand, due to the well-defined sinusoidal sweep of wavelength over time of the FDML laser and, on the other hand, by the synchronized detection with the PLL, which drives the external sample clock of the ADC card (explained in more detail in chapter 6).

This time-to-wavelength trace then serves, in combination with the pump wavelength, to calculate the probed Raman transition energies. This will be described in section 6.4. The precise calculation is shown in a comparison of a TICO-Raman spectrum with a state-of-the-art spontaneous Raman spectrum in section 7.3.

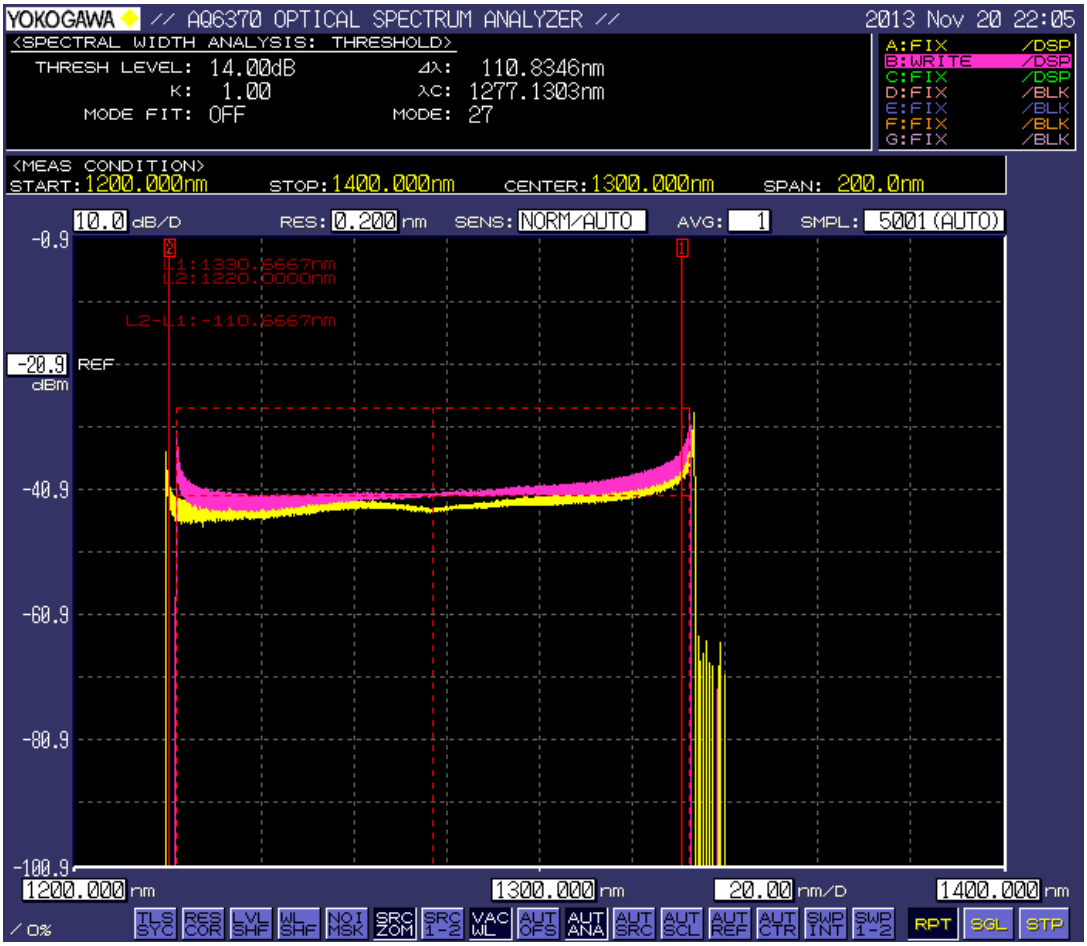

Figure 5.6: Typical spectra of an FDML laser. This spectrum is recorded in the LabVIEW measurement program and the spectral information (center wavelength, span) used for the calculation of the Raman frequency coverage.

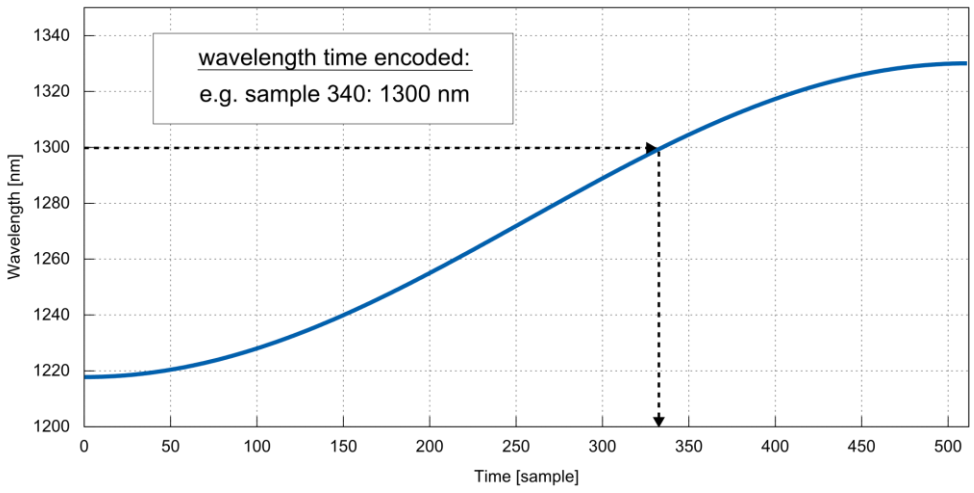

Figure 5.7: Time-to-wavelength encoding. By taking the span and the center wavelength of the FDML sweep, the sinusoidal sweep in wavelength is modeled in the LabVIEW measurement program. The synchronized PLL detection allows to assign a wavelength to each ADC sample. Together with the wavelength of the pump laser this is used to calculate the Raman transition frequencies (see chapter 6.4).

6. TICO-Raman technique

The wavelength swept FDML probe laser with its broadband span in combination with the multi-color, narrowband pump MOPA enables the coverage of a broad range of Raman transitions. In order to create Raman spectra, the stimulated Raman gain must be detected for all possible energy differences. Therefore, the time encoded (TICO) Raman concept is introduced, where the Raman transition energy is encoded and detected in time.

6.1. Concept

The idea of the TICO concept, as explained in chapter 3, is to encode the Raman transition energy in time. As a prerequisite, the FDML laser has the wavelength encoded in time (Figure 5.7). By employing a monochromatic pump laser, SRG signals (cf. chapter 1) will occur whenever the instantaneous energy difference between pump and Stokes laser coincide with a Raman transition (Figure 6.1 A)[12]. At these energy differences, molecular vibrations are coherently driven via SRS (Figure 6.1 B). The SRG signals are detected with a photodetector (Figure 6.1 C) after blocking the pump light with appropriate filters.

In a more detailed description (Figure 6.1 D), modulated pump laser pulses are used to generate SRG signals on the probe laser. This is advantageous, since the SRG signal scales linearly with the pump power and by employing high instantaneous pump powers one maximizes the SRG effect while keeping the average power exposure on the sample low (cf. chapter 1). In order to address all the possible energy differences, the TICO concept was developed, where the FDML sweep is raster-scanned by the pump pulses for SRG generation. Each rainbow-colored line in Figure 6.1 D represents one FDML sweep and the blue dots represent a pump pulse. For each sweep the pump pulse addresses a certain Raman transition. By employing a fast analog-to-digital converter (ADC) card with a synchronized sample clock one can directly digitize the SRG signals. The pump pulse length is chosen to correspond to the ADC analog bandwidth. This way, the full SRG signals are detected and digitized. In the computer measurement program the SRG signals are extracted from the ADC data stream and mapped to a spectrum. Since the wavelength of the pump is known and the wavelength of the FDML probe laser is encoded in time, the SRG signals can be mapped to Raman transition energies. In all, with the TICO approach it is possible to automatically record SRS spectra. In TICO-Raman, the raster mesh can be adjusted to the desired sample resolution which in SRS is only ultimately limited by the lasers' linewidth (in contrast to spontaneous Raman spectra which are limited by the spectrometer specifications). Additionally, the TICO-Raman concept allows to freely adjust the raster scanning pattern. In

[12] For simplification, this shows a CW pump laser. In the real implementation, flexible timed pump pulses are used.

Figure 6.1 *n* consecutive sweeps are used to probe a set of *n* Raman transitions. This can also be decoupled depending on the application. For instance, if higher speeds are needed, many pulses can be applied to one sweep (see also section 7.8). If *m* pulses per sweep are applied, the number of sweeps for one spectrum reduces to *n/m*. Similarly, if the average power exposure is critical, the pulse repetition rate can be reduced by using only every *i*-th sweep. This increases the time per spectrum to *i* * *n*. All this can be conveniently programmed as a waveform and uploaded to the AWG. This makes the TICO-approach very flexible.

An important point for the measurement of SRG signals is the intensity noise on the Stokes laser. The FDML laser in combination with the newly developed dual stage balanced detection allows for shot noise limited SRG measurements, as will be explained in chapter 6.7.

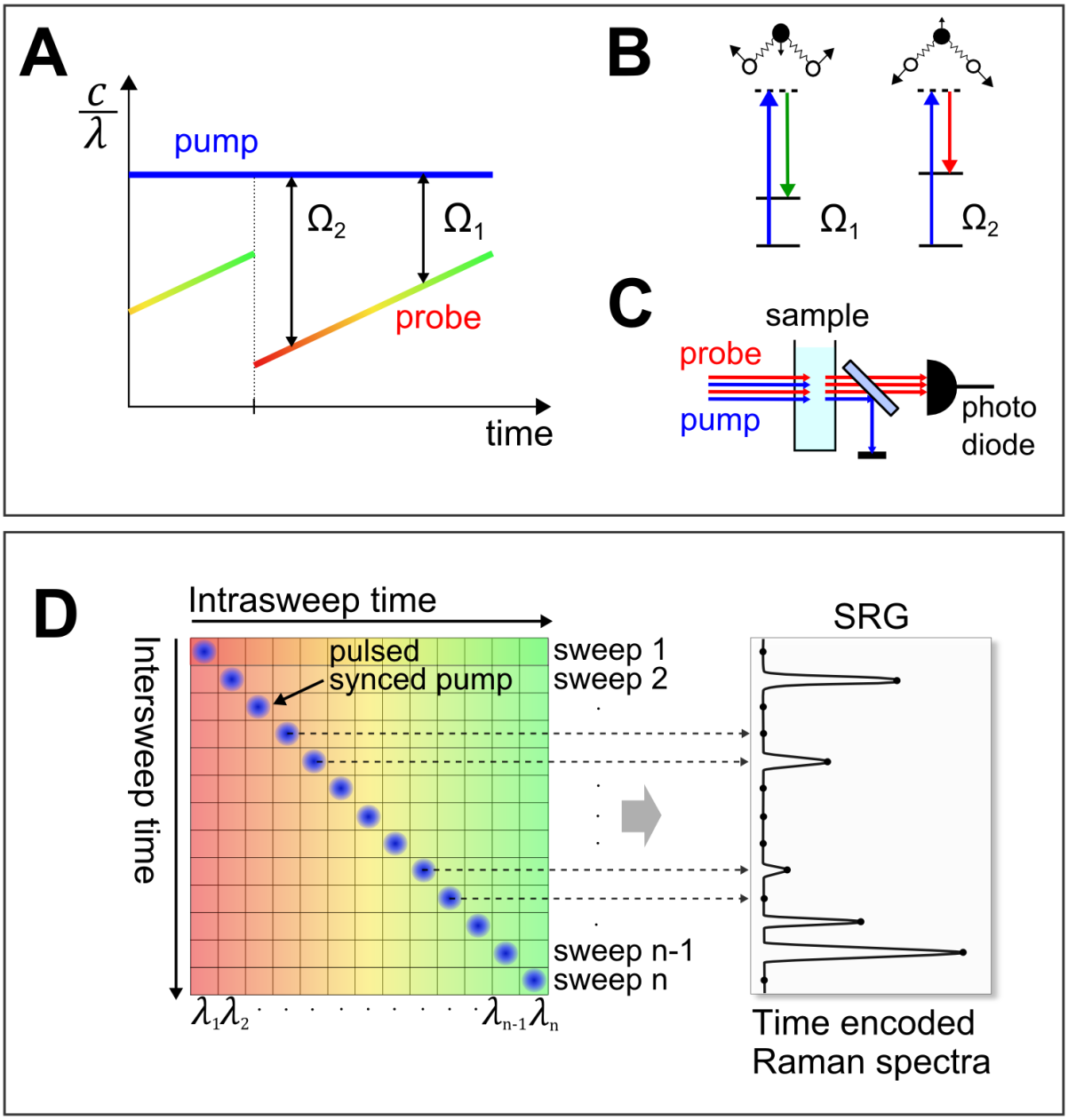

Figure 6.1: The time encoded (TICO) Raman concept. (A) The energy difference between pump and probe laser is swept in time. (B) If the energy difference corresponds to a Raman transition, a molecular vibration is excited. This leads to an annihilation of pump photons and, correspondingly, to a creation of probe photons (C). This stimulated Raman gain (SRG) signal is detected on a photodiode as an intensity change on the probe laser. (D) In more detail, the pump laser is modulated to short pulses, in order to enhance the SRG signal. These pulses are raster-scanned over the set of probe wavelengths (rainbow-colored). This raster-scanning is conducted by programming the timing relative to the sweep start. This time-encoded concept allows to detect and map the SRG signals to a Raman spectrum (D, right).

Another representation of the TICO-Raman concept is shown in Figure 6.2, showing especially the process of signal extraction. This is a detailed description of raster-scanning with 512 spectral points. The pump pulses are set at 512 positions of the probe sweep, one pulse per sweep, at 512 consecutive sweeps (Figure 6.2 I.A). This effectively tunes the energy

difference or, equivalently, the wavelength difference (Figure 6.2 I.B). The probe laser is detected in a time-gated window that corresponds to the duration of the Raman effect (i.e. the pump pulse duration since the Raman effect is instantaneous). The measured SRG signals are mapped to a spectrum (Figure 6.2 I.C-D). This mapping process is depicted in Figure 6.2 II, where the SRG signals are not only mapped to spectral points but through the time-encoded wavelength information also Raman transition energies are calculated and assigned.

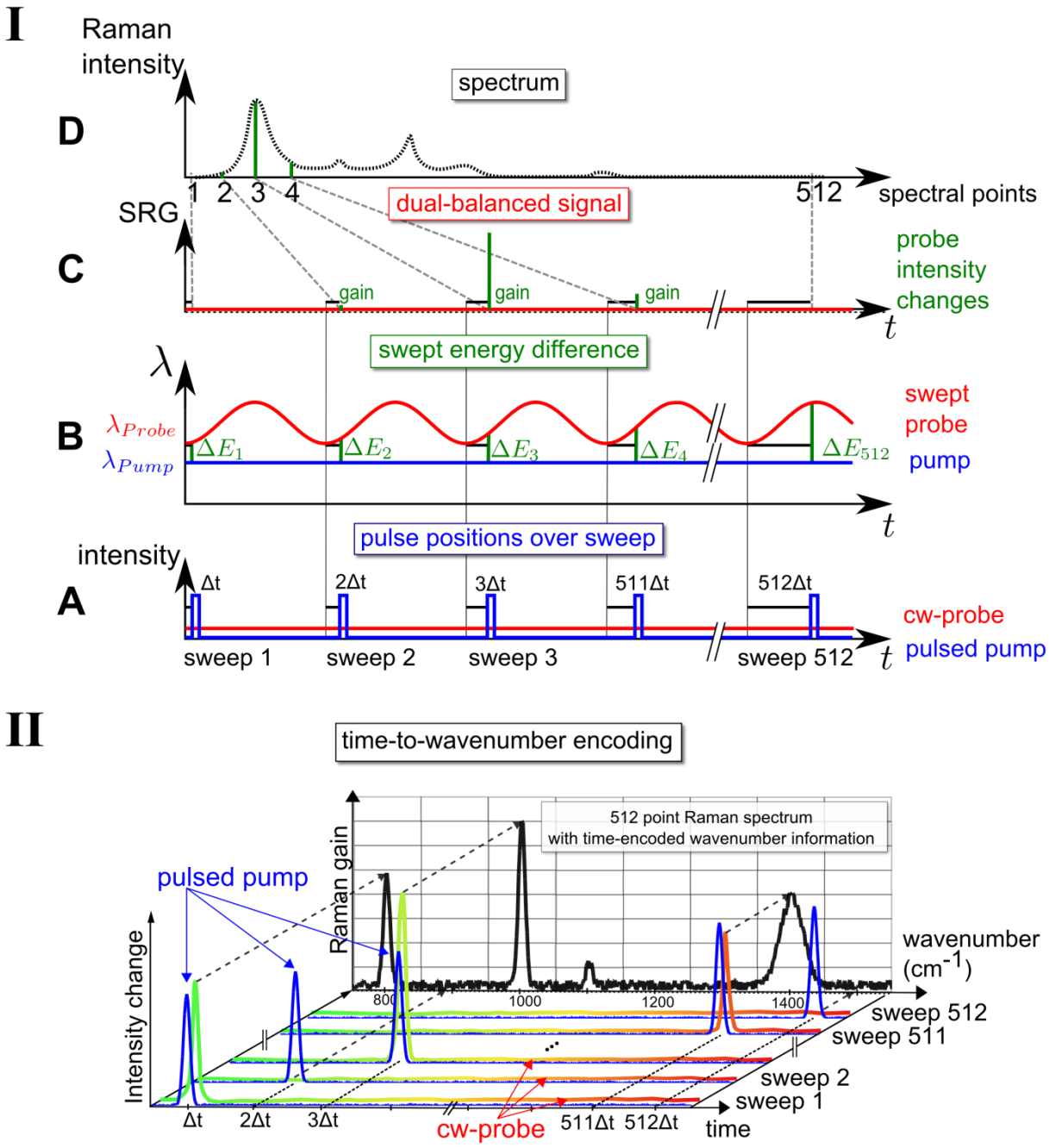

Figure 6.2: Schematic representation of the TICO concept. **(I.A)** The pump pulses raster scans the set of energy differences at 512 spectral positions. These correspond to 512 time delays Δt with respect to the sweep start. **(B)** The wavelength swept FDML laser enables the Raman transition energies to be swept. The SRG signals are detected **(C)** and combined to a spectrum **(D)**. **(II)** the TICO information is further used to map the spectral points to Raman transition energies (cm^{-1}).

6.2. Implementation

In the actual setup implementation (Figure 6.3) programmable waveforms are used to drive both lasers together with a synchronized detection to recover the full SRG signal heights. This can be achieved through the AWG, the two flexible laser sources, and a PLL for

the ADC card. As Stokes laser two FDML lasers around 1300 nm and 1550 nm are used[13]. The filter was driven at either 415 kHz for imaging, or at 55 kHz for spectroscopy. This difference in speed is due to the AWG, which is limited in sample clock speed at 100 MHz, as will be calculated in the following text.

For spectroscopy, it is wanted to raster-scan the spectra at higher resolution. A total of 1024 samples per FDML sweep were chosen, resulting in 512 spectral positions for one sweep. This resulted in 56 MHz synchronized sample clock speed[14]. One complete waveform programmed to the AWG contained 512 sweeps plus one extra sweep at the end for digital balancing. In digital balancing (cf. Figure 6.5) the same sample of the subsequent sweep is used for background subtraction. This means, that if sample *i* of one sweep is sampled by the pulse, i.e. used for SRG signal detection the same sample *i* of the next sweep without pump is used for the background. This is possible, as the FDML laser has a good sweep-to-sweep correlation. For the last sweep with pump pulse, there is a subsequent final sweep added to serve as reference. In this final sweep no pump pulse is positioned.

For imaging 64 spectral points were chosen, so the final waveform had 65*128 samples on the AWG and the sample clock rate was 128*415 kHz=53 MHz. For more details see also the publication on the system [12].

The output of the FDML lasers was amplified in a booster stage [5] with the same SOA than the one in the cavity in order to boost the output to 100 mW. After the booster, the light was splitted by a 50:50 coupler. One port was used for the Raman signal, the other one served as a reference signal for the differential photodetector. The reference arm had a free-space delay stage (not shown in Figure 6.3) in order to set the same optical pathway for both arms to ensure optimal common mode rejection in the balanced photodiode. Additionally, this delay stage can be used to adjust the reference power and optionally to insert duplicate filters used in the sample arm, compensating for any chromatic imperfections of the filters. In the sample arm, the fiber output of the FDML laser was collimated by aspherical lenses (f=18.4 mm). A dichroic mirror served as a beam combiner for the FDML light and the pump light. The pump laser was also collimated by an f=18.4 mm aspherical lens. Shortpass filters in the pump beam were used to filter any light at longer wavelength than the pump light. This is necessary, since SRG signals on the probe light as low as 10^{-6} are to be detected. The powers used were 2 mW of probe light and about 1 kW of pump light, i.e. six orders of magnitude higher instantaneous pump power than probe power. This means, that any residual light of the pump needs to be attenuated by more than twelve orders of magnitude. This holds especially true for any spontaneous Raman light of the pump light produced inside the delivery fiber that may be scattered from 1064 nm up to around 1300 nm. This light would obscure an SRG signal, so it is crucial to filter this out by shortpass filters in the pump arm before combining it with the probe light.

[13] The use of two FDML lasers allows the broad spectral coverage, as explained in section 6.5.

[14] With an FDML laser at 55 kHz and 1024 samples per sweep one calculates the required sample clock speed to 55 kHz * 1024 = 56.320 MHz.

After combining the pump and Stokes light, an aspherical lens (f=4.5 mm) focuses the light on the sample. This achieves a focal spot diameter ($1/e^2$) of the 1310 nm light of 2.25 µm[15], which allows for a short interaction lengths of the two laser beams (50 percent of the Raman effect occur within two times the Rayleigh length, which corresponds to about 6 µm for this setup). Careful adjustment of the beam overlap between pump and probe lasers is crucial. A chromatic error on the focal positions was observed between the different wavelengths due to the fused silica aspherical lens used for focusing. This was compensated by adjusting the collimator of the pump beam. This produced a slightly diverging beam but led to a good overlap between the pump and the probe beam. The two focal positions were adjusted by inserting a glass objective slide in the focus of the probe beam and adjusting the pump beam divergence to maximize the reflection signal.

The overlap was directly optimized by the SRG signal height of benzene, which was compared to a reference value found in literature [4]. In a future setup, better microscope objective or achromatic lenses can further improve the performance.

After the sample volume, the two beams were recollimated using the same lens as used for focusing. After recollimation, a telescope lens system was used to lower the beam diameter to avoid additional fringe[16] noise (cf. Figure 6.9). The pump light was then filtered out by a set of dichroic longpass filters. The probe light was then focused on the balanced photodiode. After subtraction of the reference light, the electrical signal is amplified by a transimpedance amplifier and digitized on a personal computer. The digital processing is described in the next section.

[15] The calculation uses a mode field diameter (MFD) of 9.2 µm for Corning SMF-28e+ fiber. This results in a focus diameter of 9.2 µm*4.5 mm/18.4 mm=2.25 µm.

[16] With "fringe" a sinusoidal modulation due to interference is described. See Figure 6.9 for an example.

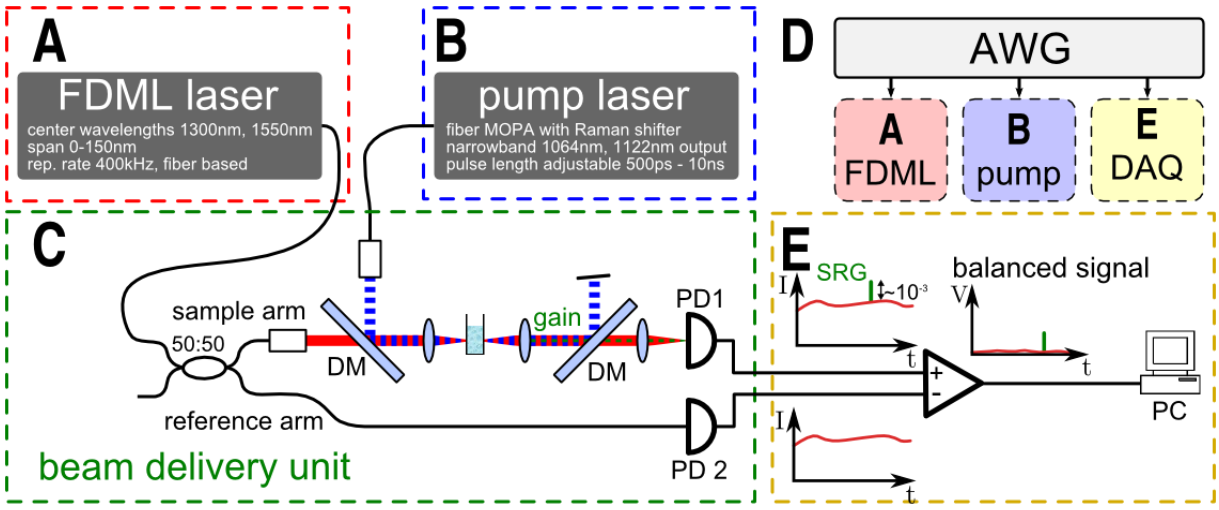

Figure 6.3: The schematic setup of the TICO Raman system. (A,B) The probe and pump lasers are fiber-based, making the delivery to the Raman sample easy. (C) The fiber outputs are collimated and the pump and probe beams combined on a dichroic mirror (DM). The beams are then focused on the sample. After the sample, the pump pulses are filtered out by DMs and only the probe laser is detected on a balanced photodetector (PD1,PD2). For that, a 50:50 fiber coupler is inserted in the probe delivery fiber, thereby providing the reference signal for the balanced PD (E). The electronic balancing subtracts the probe offset and the ADC card in a personal computer (PC) effectively digitizes only the SRG signals. This way, the ADC range is optimally utilized only for SRG detection, avoiding loosing bits for the probe power offset. (D) The AWG drives the whole system. Both lasers are driven synchronously by the AWG, no dedicated locking mechanism is necessary. Furthermore, also the data acquisition (DAQ) is driven synchronously by the AWG, enabling full detection of the SRG signal.

6.3. Digital processing with PLL driven detection (dual-stage balancing)

The detection was driven synchronously in order to allow the time-to-wavelength calculation and, thereby, the assignment of Raman transition energies (see also the next section 6.4). In addition, it allowed to employ a new kind of balancing, called digital balancing, which is part of the newly developed dual stage balancing technique, which enables a shot-noise limited detection. This technique will be explained here.

The electrical signal from the photodiodes, as mentioned before, is created in a differential, balanced photodiode. This achieves rejection of common mode noise, as this noise is present on both the sample and the reference arm. Furthermore, it subtracts the probe light offset. The SRG signals are usually only small compared to the large signal offset (about 10^{-3}), so subtracting this offset via a differential photodiode makes the detection of the small SRG signal more efficient. Without the offset, the full range of the ADC (i.e. also the whole 14-bit) can be optimally used only for intensity changes occurring in the sample arm. This step is shown in Figure 6.5 on the left. This step is the analog balancing.

In the middle of Figure 6.5, the second step is shown. This step is called digital balancing, since a digital referencing step is performed which is made possible due to the

coherence properties of the FDML laser. Shown above in rainbow colors is the superposition of 512 sweeps. The 16-bit resolution (14-bit effective) of the ADC card is used for an 800 mV range, instead of the ~10.000 mV DC-coupled trace. The 512 rainbow colored traces show a small deviation from a perfect zero-line as some ripples are still present. These ripples are due to chromatic imperfections in the optical components, making the sample and reference arms not perfectly power balanced over the ~150 nm wavelength span. Fortunately, these ripples remain the same over all 512 sweeps. With the newly introduced digital balancing, one can subtract these ripples by subtracting consecutive sweeps. This is shown in the middle, lower graphs. As the temporal position of the Raman pump pulse is increased for every sweep, subtracting the same sample position from consecutive sweeps subtracts the ripples and only the SRG signal remains. This results in a SRG spectrum with shot noise limited performance (digital balanced signal, blue curve).

In the third step, the wavenumber values are assigned to the TICO spectrum. The FDML wavelength values over time are known (cf. Figure 5.7) and by calculating the energy difference to the pump wavelength, one can calculate the Raman vibrational energies. This results in high-quality spectra with highly accurate wavenumber values. Figure 6.5 shows experimental data of neat benzene, measured with a 1064 nm pump and an FDML around 1550 nm.

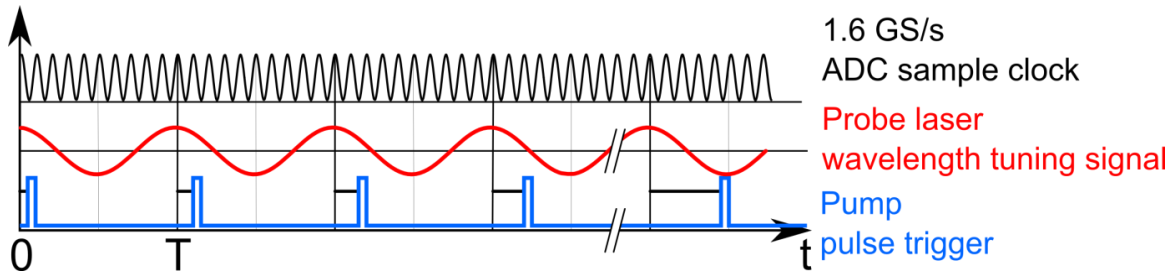

Figure 6.4: The TICO electronic waveforms used for synchronized excitation and detection. The blue curve is the trigger signal for the MOPA pump laser. The pulses are delayed with respect to each FDML sweep for consecutive sweeps. The red curve is the sinusoidal waveform that drives the FDML laser. The black, upper waveform is a high-frequency waveform at up to 1.6 GHz that is used to synchronously drive the detection. Therefore, a PLL multiplies a waveform from the AWG to this high frequency. This signal is then used as external sample clock input in the ADC card.

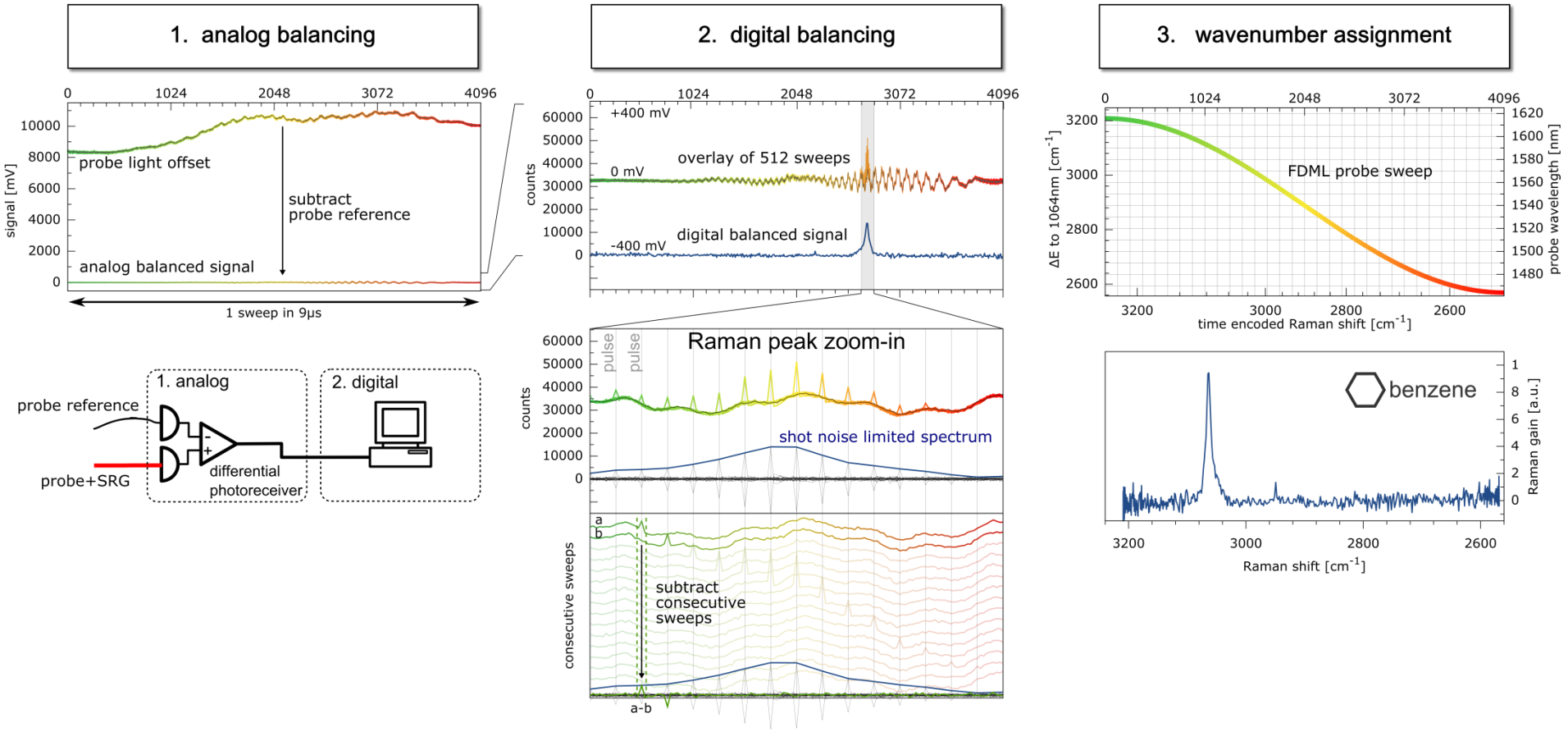

Figure 6.5: The dual balancing concept explained step-by-step. Left: In the first step, the analog balancing subtracts the reference signal. This step subtracts both common mode noise and the probe light offset in order to use the ADC card resolution only for SRG signals. Middle: In the second step consecutive sweeps are subtracted. Any remaining noise on the signal (here ripples) are subtracted and only the SRG signals are extracted. This step finally reduces the sensitivity down to the shot noise limit. Right: In the last step, the calculated wavenumber energies are mapped to the SRG signals through the well-defined wavelength sweep of the FDML laser. This results in the high-quality TICO-Raman spectra with wavenumber information. Shown is experimental data of neat benzene around 3000 cm^{-1}.

6.4. Time-to-wavenumber calculation

As described in section 5.3, the FDML laser has the output wavelength encoded in time. In practice, this can be used to calculate the Raman transition energies (cm^{-1} wavenumber values). First, the FDML span is measured with an optical spectrum analyzer (OSA) (sample data shown in Figure 6.6, inset). Then, a time trace of the wavelength is calculated, made possible by the PLL driven detection ensuring a constant sweep-to-sweep time base. Together with the wavelength of the pump laser, this can be used to generate a time-to-wavenumber mapping which is used to assign wavenumber values to the TICO Raman spectra. This is shown in Figure 6.6, where a wavenumber is assigned to every sample position (i.e. time) of the sweep.

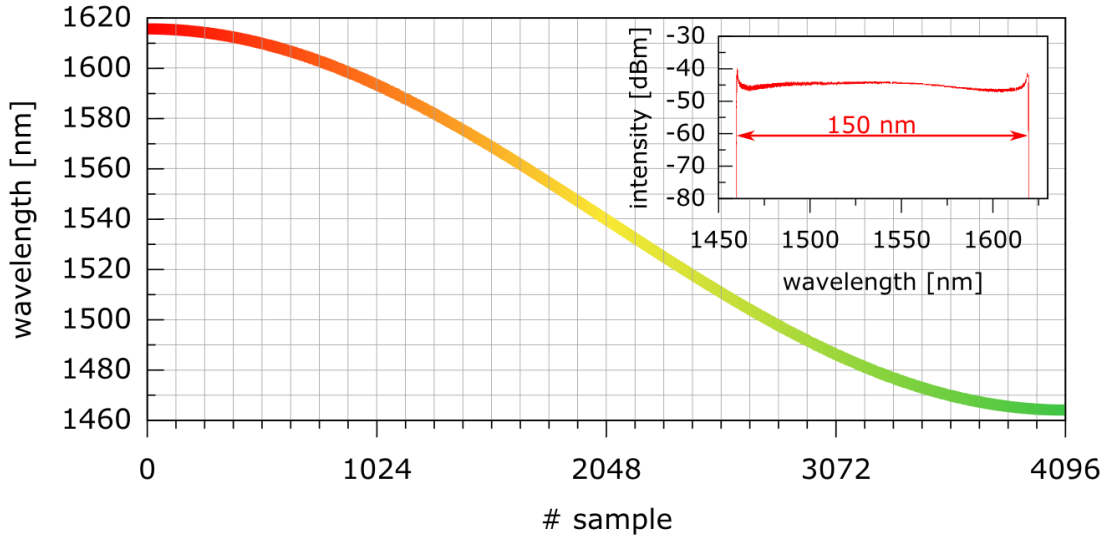

Figure 6.6: Calculated wavelength sweep used for wavenumber assignment. First, the wavelength sweep (center wavelength and sweep range) of the FDML is recorded with an OSA (inset). A cosine waveform is then calculated for the sweep in the LabVIEW measurement software with the sample information obtained from the time-synchronized detection and the wavelength information extracted from the OSA sweep. This way, every sample position of the ADC card is assigned to a wavelength and, in the subsequent step, to a wavenumber value through the knowledge of the pump laser wavelength (see also Figure 6.5).

For the time-to-wavenumber calculation exact timing is crucial. Therefore a PLL was employed, driven by a phase-locked signal from the AWG, which provides a synchronized sample clock input for the ADC card. Another important aspect is the temporal offset of the first pump pulse position in the Raman sample (first black line in Figure 6.7). The generation of the pump pulse and the propagation in the pump laser takes a certain time, which does not necessarily coincide with the time of the propagation of the FDML laser. Therefore, before

measuring TICO Raman spectra, this timing between pump, probe and detection needs to be determined and accounted for. Therefore, a glass objective slide is inserted in the probe beam, resulting in a fringe pattern being visible on the probe light (cf. Figure 6.7). This fringe pattern shows the relative phase of the FDML sweeps. Then, the first sweep can be set to start at the position of the first pump pulse (not shown, but timing is indicated by the left vertical black line) by setting a phase correction value in the AWG. The pump pulse position is measured by removing the pump blocking filters (at low pump powers), so the pump pulses are incident on the photodetector. Once the FDML sweep and the first pulse are synchronized by adjusting the phase of the FDML waveform on the AWG, the detection needs to be adjusted to account for this pump pulse offset, i.e. the delay between the ADC trigger start and the first pump pulse. This pump pulse sample offset is directly set in the LabVIEW software by omitting the first few samples (usually about 80 samples). Once this sample delay and the FDML phase are set, the TICO-Raman spectra can be recorded in a fully automated manner with probe offset corrected SRG signal heights and correct Raman transitional energies.

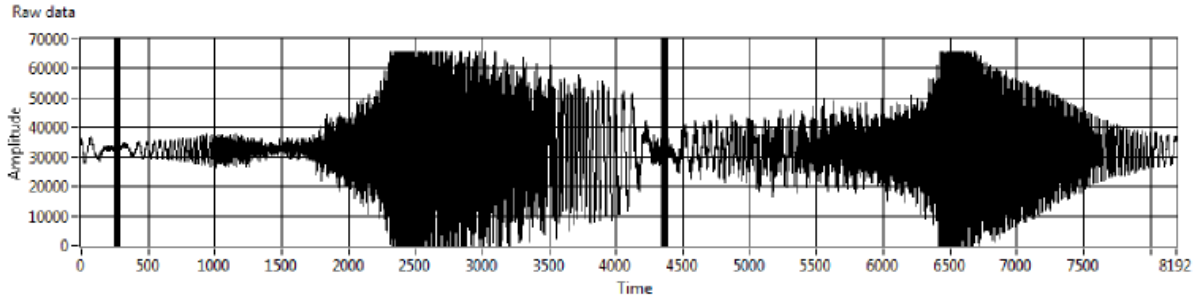

Figure 6.7: Fringe pattern showing the relative phase of the FDML laser sweeps. By inserting a glass plate in the beam, interference fringes on the swept FDML laser are generated. These can be used to find the turning points of the sweep. The phase of the FDML driving waveforms are then adjusted an the AWG to correspond to the phase of the first pump pulse (indicated by black lines). This ensures that the first pump pulse probes the start of the wavelength sweep.

6.5. Spectral coverage

In order to address all relevant Raman transitions, the TICO system is capable of covering the whole Raman spectrum from 250 cm^{-1} up to 3250 cm^{-1} (Figure 6.8). This comprehensive coverage of 3000 cm^{-1} is possible by combining several pump wavelengths with two FDML lasers. The pump wavelengths are at 1064 nm, 1122 nm and 1186 nm (cf. Figure 4.9, section 4.3) and the two FDML lasers operate around 1310 nm and 1550 nm. The thereby obtained spectra provide a spectral overlap region which aids stitching a comprehensive Raman spectrum. Examples are shown in the experimental results section 7.1.

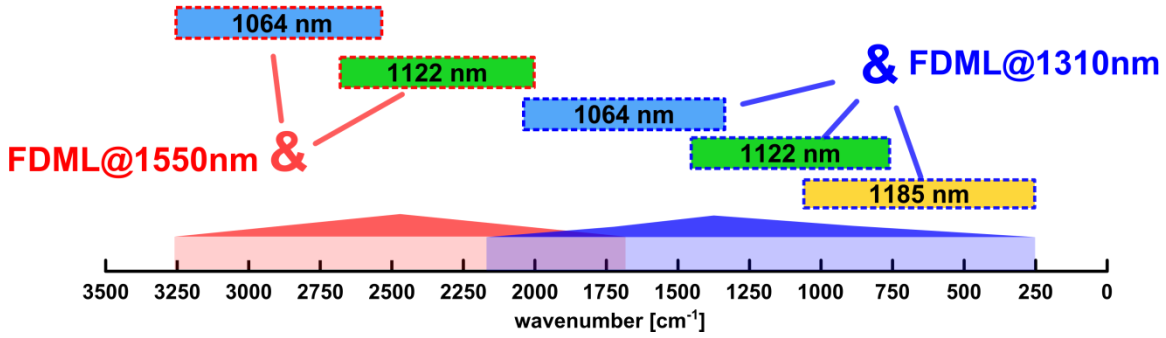

Figure 6.8: Spectral coverage of the current TICO system. By combining three pump wavelengths with two FDML lasers, it is possible to comprehensively address Raman vibrational energies from 250 cm^{-1} up to 3250 cm^{-1}.

6.6. Spectral resolution

The spectral resolution is currently given by the pump and probe lasers' linewidth and the sampling density of the spectra. A maximum of 512 spectral points limit per single spectrum is given by the AWG and the slowest FDML laser sweep repetition rate of 55 kHz (see chapter 6.2 for more details). The sampling spectral resolution can be increased by lowering the overall span of the FDML laser. The final limit is then set by the laser linewidth. The pump laser at 1064 nm[17] has a FWHM linewidth of 0.06 nm (cf. Figure 4.9) which translates to 0.5 cm^{-1}. The higher bound value of the probe laser is given by the FDML laser at 1250 nm with an estimated instantaneous linewidth of ~100 pm [33] or 0.6 cm^{-1}.

6.7. Measures for shot noise limited performance

For recording even smallest SRG signals, the intensity noise on the probe laser needs to be minimal. This is ensured if the SRG signals are only limited by the fundamental shot noise caused by the probe light (cf. section 5.1). This limit was reached for the TICO-Raman system, as several measures were taken. First, the FDML operation was carefully adjusted before every TICO-Raman measurement. The polarization in the FDML ring was adjusted and the filter frequency was set to minimize the noise. Second, the analog balancing (cf. Figure 6.5, left) with the differential photodiode was optimized by carefully matching the reference arm power to the sample arm power. Third, digital balancing (cf. Figure 6.5, middle) further reduced the noise by subtracting same samples of consecutive sweeps, one with SRG and one without. This removed most of the remaining noise. Nevertheless, a small noise remained, which was analyzed as a high frequency noise occurring in the free-space

[17] The lowest wavelength has the highest relative spectral width. For this reason, the lowest wavelength for the pump and the Stokes are considered for spectral resolution. This, of course, is only the case if the absolute FWHM values of the laser linewidth are the same for all wavelengths.

setup: The origin were interference fringes originating from optical elements which increased the noise, probably due to small phase fluctuation from sweep to sweep of the FDML. This was resolved by first minimizing reflections in the setup. All the dichroic filters for the pump blocking were set at the Brewster angle and the polarization of the probe laser were adjusted accordingly. Imperfections in the polarization led to a residual interference, therefore a beam telescope was installed to lower the beam diameter (cf. Figure 6.9). As can be seen in the figure, this smaller beam diameter avoids a spatial overlap between two-fold reflected light in the filters, thereby minimizing fringe occurrences. As an alternative in the future, an overlap can be prevented by using thicker filter substrates.

Another important measure to prevent additional noise was the use of an AR-coated photodiode (Fermionics, FD300W). This diode was used to collect and detect the probe light in the sample arm.

The combination of these measures achieved shot noise limited measurements at 2 mW of probe power with a relative noise level at 4.7 x 10^{-4} (see section 5.1 and [12] for details).

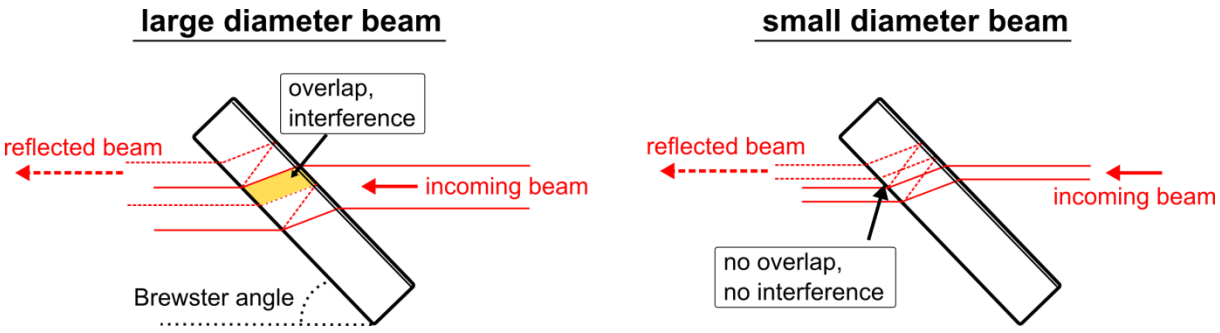

Figure 6.9: The use of a smaller beam diameter can help prevent interference fringes due to reflections in the optical elements. Left image: a large beam diameter causes a spatial overlap through which interference fringes occur. Right image: A small beam diameter prevents an overlap and therefore no interference fringes occur. This measure was necessary, even though the filters were positioned at the Brewster angle (see text).

7. TICO Raman spectroscopy

With the presented system it is possible to acquire fully automated SRS spectra with correct wavenumber information at high resolution and broadband coverage. This chapter presents experimental results of the recorded spectra. The next chapter will present hyperspectral Raman microscopy.

7.1. Results full spectrum

Figure 7.1 shows a Raman spectrum of benzene recorded with the TICO-Raman setup. The whole range of relevant Raman vibrations from 750 cm^{-1} to 3150 cm^{-1} is covered. The spectrum is merged out of four individual spectra, acquired with different FDML lasers and pump wavelengths. Two pump wavelengths at 1064 nm and 1122 nm were combined with two FDML lasers around 1310 nm and 1550 nm for the broadband coverage. Each individual spectrum consists of 512 spectral points (see also section 6.2). In the manual merging process, duplicate spectral points were dropped in the overlapping regions. The full spectrum thus consists of 1564 spectral points. Each single spectrum was averaged 1000-times for high signal-to-noise ratio (SNR). The measurement time for one single spectrum is 9 ms, i.e. 9 seconds for the 1000-times averaged single spectrum.

Besides the broad coverage, another remarkable feature of this spectrum is the high resolution. The narrowband peak of benzene, shown closer in the zoom-in, is clearly resolved. The sampling density in this region is 2 cm^{-1}. Nevertheless, higher resolution is possible (see also section 6.6). This higher resolution can be reached by dynamical spectral zooming, which is presented in section 7.4. This is also a fundamental advantage of SRS over spontaneous Raman, that the resolution of the spectra is only ultimately limited by the laser linewidth. As a side mark, SRS even allows spectroscopy of gases and resolving the rotational splitting of the vibrational modes [35].

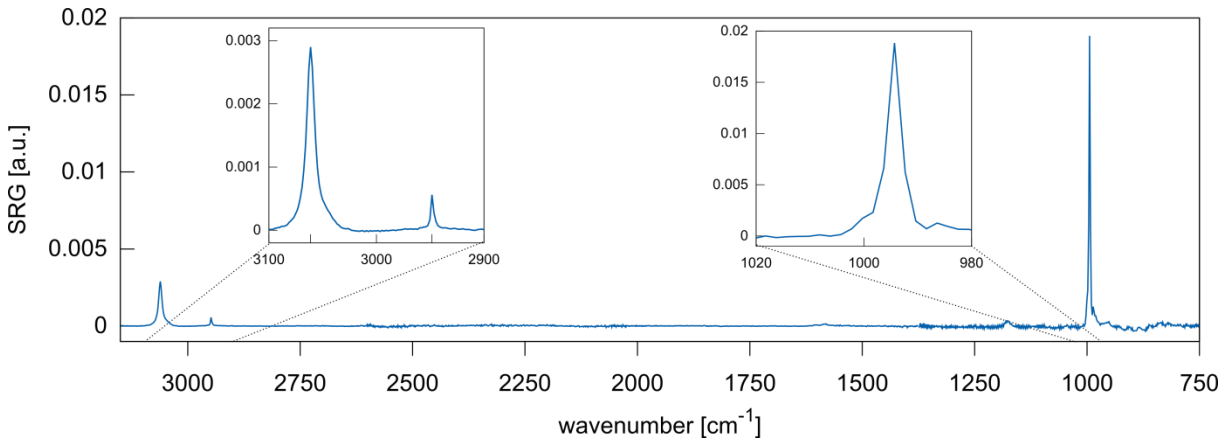

Figure 7.1: Raman spectrum of benzene with coverage from 750 cm^{-1} up to 3150 cm^{-1}. This spectrum was background corrected (explained in Figure 7.2). The noise is shot noise limited by the FDML Stokes laser. The spectrum was combined out of four individual spectra, each with ~700 cm^{-1} coverage and 1000-times averaged. The two zoom-ins show the high resolution and the high SNR of the spectrum. Upon merging the individual spectra, some duplicate spectral points were dropped (see text).

A problem in the stitching process was the background in the SRS spectra (see Figure 7.2). Therefore, an automated baseline was detected in Origin software. This background was generated and subtracted for each individual spectrum. The origin of this background is not definitely known, yet. However, it can be speculated to arise either from thermal effects due to pump absorption or non-linear cross-phase modulation (XPM)[18,19] [36, 37]. In fact, the background is not observed when only the pump or the probe light is present, but only when both are incident on the sample, so an origin due to fluorescence or chromatic error of the balanced detection is excluded. Pump light absorption can lead to a thermal effect, which changes the refractive index and hence lead to an intensity change of the probe laser. This was especially pronounced with long sample length (~1 mm), resulting in a donut shaped diverging probe beam in the far field. However, this effect was strongly reduced in the presented measurements by increasing the NA which consequently required only a 20 µm long sample length, thus drastically reducing pump absorption. The remaining effect can be seen in Figure 7.3, where three different chemicals and their mixture were recorded three times each and the intensity change of the probe beam observed (pump pulse occurs at sample 3). Interestingly, this intensity change prevails over more than one sample (~11 samples, i.e. ~14 ns), so longer than any instantaneous SRG or XPM effect.

[18] XPM is based on the Kerr effect and it causes a change in the refractive index of the probe beam induced by the nonlinear intensity of the pump beam. This refractive index change can lead to a change in divergence of the probe beam, which can then lead to a change in the recorded power of the probe beam. This intensity change induced by the pump pulse is thus indistinguishable from an SRG signal. However, for future measurements this can be improved by using higher NA condenser lenses after the sample [36].

[19] Another common explanation is two-color two-photon absorption. This, however, would show up as a loss in both pump and probe power. Consistently, it can be seen in the common case of SRL measurements, but is contraindicated with the here observed gain.

A further observation on the background effect of Figure 7.2 is that it differs between the individual spectra, which may be due to the different pump/Stokes wavelength combinations and the respective linear (thermal) or nonlinear (XPM) refractive index dependency. Another factor is that the alignment of the beams and the collimation were adjusted individually before each measurement of the individual spectra leading to different impacts on the divergent beams. As the aspheric lenses used for focusing and condensing had a chromatic focal shift, the pump beams were adjusted for best focal overlap, leading to a slightly diverging pump beam after fiber collimation (see also section 6.2). This divergence angle changed for the different pump/Stokes wavelengths combinations in the four individual spectra. In conclusion, the study of the exact source is still under investigation, especially as it does not show up consistently in all measurements (cf. raw data shown in Figure 6.5 middle-bottom).

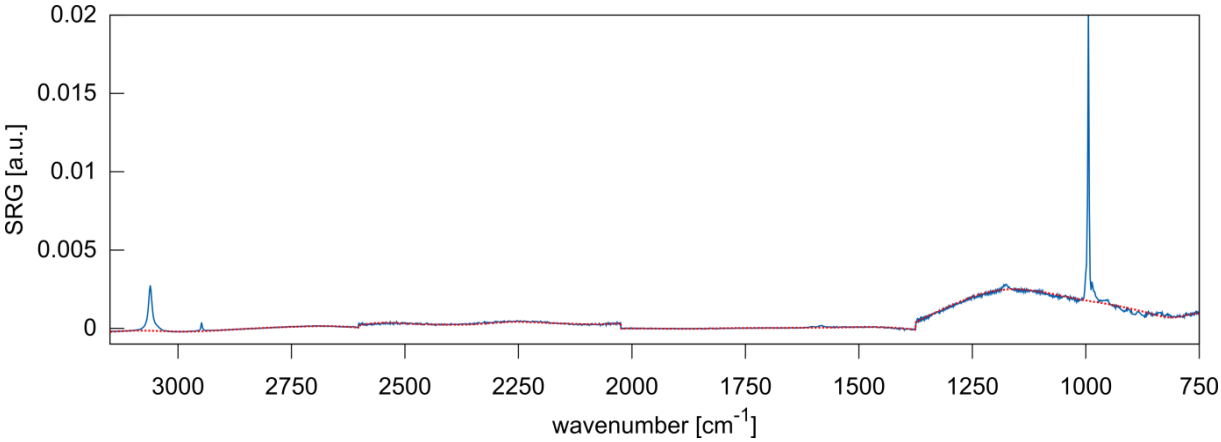

Figure 7.2: Spectrum of benzene (blue line) with the background (red, dotted) used for subtraction. This background is probably due to XPM occurring in the sample [36, 37]. The background was determined by an automated baseline detection in Origin software. This baseline was used for background subtraction for the data shown in Figure 7.1.

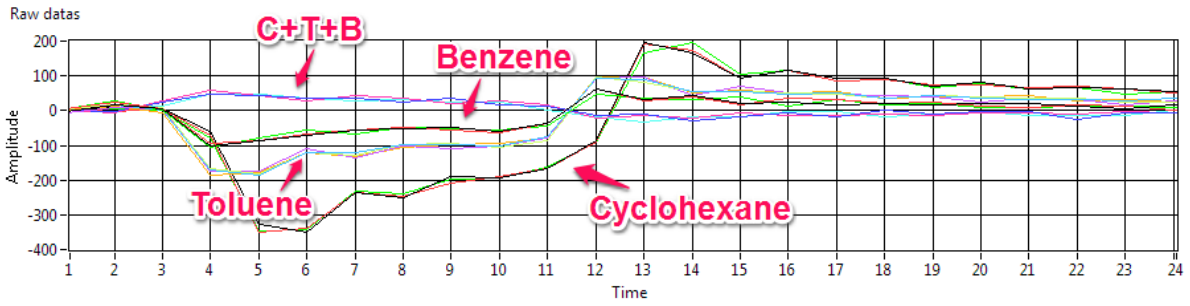

Figure 7.3: Pump induced probe intensity change in different chemicals. Shown is the intensity change of the FDML probe laser. At sample 3 the pump pulse is incident on the sample, which leads to a intensity change that prevails for several nanoseconds (~11 samples, i.e. ~14 ns). For each chemical, three consecutive measurements are plotted, which show a repeated behavior for each single chemical, but a variation for the different chemicals. (C+T+B: mixture of cyclohexane, toluene and benzene).

The individual spectra were divided by the probe and pump powers. This makes the noise contributions show up differently, as the 1122 nm pump power (~450 W peak) was less than the 1064 nm pump power (~1600 W peak).

The spectrum in Figure 7.1 shows a high SNR of ~500 for the 3060 cm^{-1} peak. The improvement of the SNR over the number of averaging was studied and the results are presented in Figure 7.4. The unaveraged spectrum already has an SNR of 34[20]. The noise of the FDML Stokes laser was shot noise limited. Nevertheless, as discussed before, when the pump pulse was applied, a background showed up. This background effects the noise contribution, as is apparent in the analysis in Figure 7.4. The noise was determined in two different spectral regions corresponding to two different wavelength regions of the FDML Stokes laser. In region I, the SNR increases at first, but then saturates near a value of ~500. In region II the SNR increases further to ~1600 for 10,000-times averaging, following almost the theoretical square-root behavior. The different behaviors in the different regions can be explained by considering the respective FDML dynamics. In region II, the FDML laser almost doesn't change its wavelength. Therefore, a wavelength dependent background effect does not show up in the standard deviation. This is different in region I, where changes in the background contribute to the standard deviation. This can be explained by a changing mean value of the samples (i.e. a slope in the graph, better visible on a logarithmic scale in Figure 7.5) which results in a larger standard deviation. If a baseline is subtracted to account for this slope, the SNR in region I increased by more than a factor of 2 to ~1200. In order to better visualize this background and the high SNR of the spectrum, Figure 7.5 shows the spectrum of benzene around 3000 cm^{-1} represented on a logarithmic scale.

[20] The SNR of 34 is calculated by dividing the peak height of the 3063 cm^{-1} peak with the noise in region I. As the noise in region II is initially higher, the unaveraged SNR with respect to region II is 24.

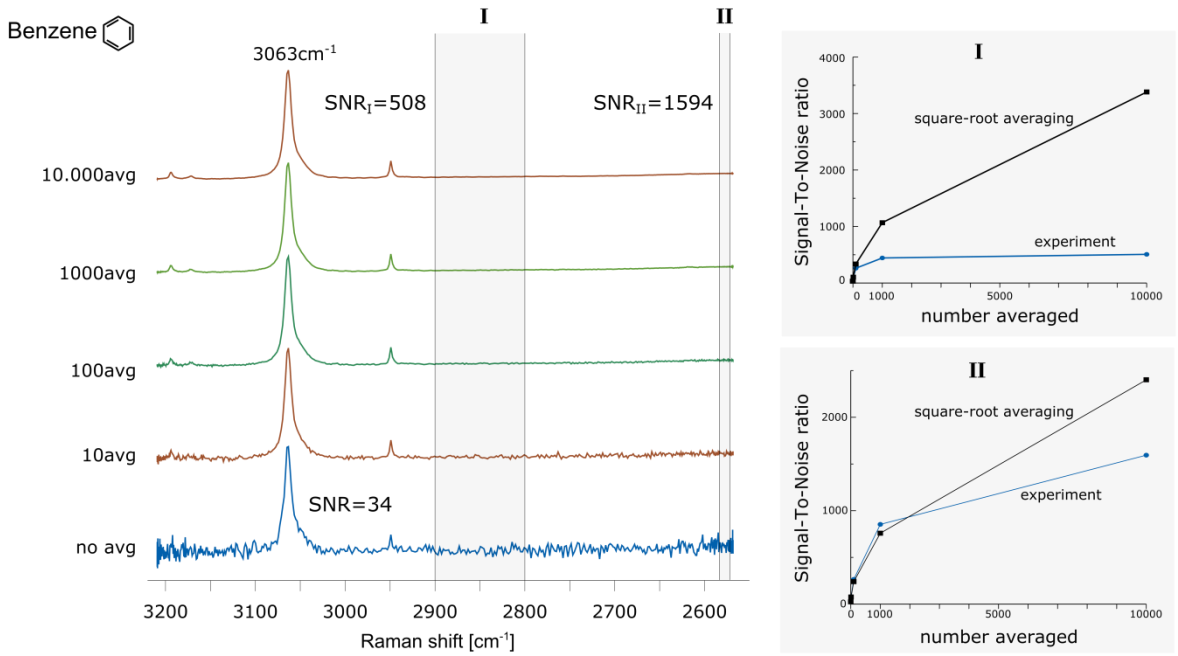

Figure 7.4: Improvement of the SNR of the TICO-Raman spectra with averaging. Two spectral ranges were chosen to measure the noise vs. averaging for different spectral regions of the FDML Stokes laser. The initial SNR of 34 increases to 508 (SNR_I, noise from region I) and 1594 (SNR_{II}, noise from region II), which is close to the maximum square-root behavior. The saturation in region I is probably due to the background on the spectra, which is visible as a linear slope which slowly decreases towards higher wavenumber values (see also Figure 7.5). In region II, where no slope is present, the SNR[21] still increases, as is discussed in the text.

[21] The term noise here includes background signals like thermal effects or XPM, that also contribute to the standard deviation used to calculate the noise value.

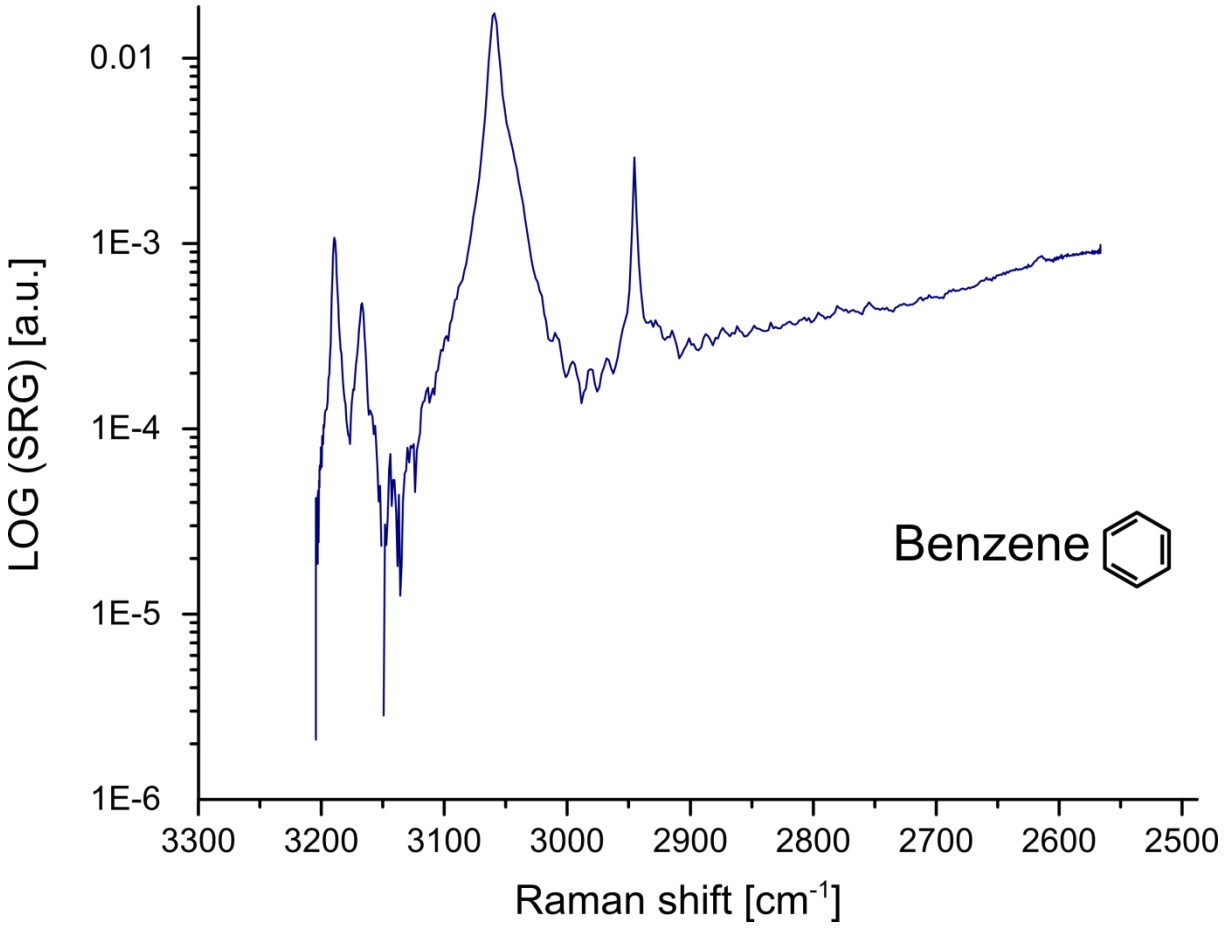

Figure 7.5: TICO-Raman spectrum of benzene on a Log-scale. This is spectrum was 10,000-times averaged for high SNR. The spectral background is also better visible on the Log-scale. An offset was added to shift all values into the positive in order to enable logarithmic scaling.

Figure 7.6 shows a broadband covered TICO-Raman spectrum of a chemical mixture of cyclohexane, benzene and toluene (CBT). The high-resolution spectrum covers the relevant Raman spectrum from 750 cm^{-1} up to 3150 cm^{-1}. This spectrum, like the one presented in Figure 7.1, was merged of four spectra. The pump and Stokes powers, the number of averaging and the spectral resolution are the same as for the spectrum in Figure 7.1.

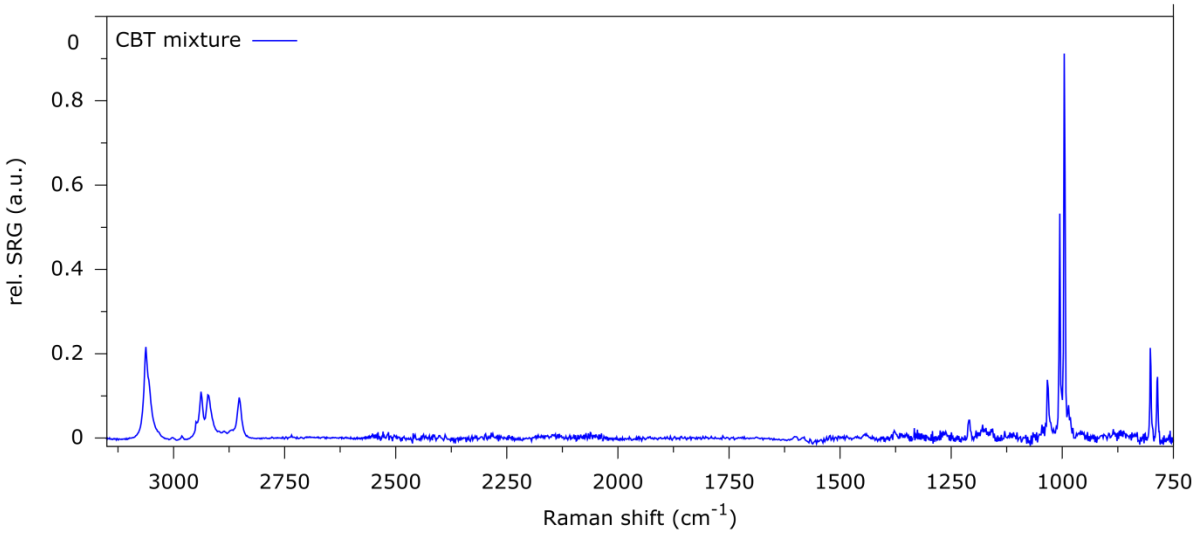

Figure 7.6: TICO-Raman spectrum of a mixture of cyclohexane, benzene and toluene (CBT) in equal parts. See section 7.4 for a high-resolution zoom-in into the crowded region around 1000 cm^{-1}.

7.2. Results spectrum with 1186 nm pump light

The cascaded Raman shift at 1186 nm light of the pump laser was found to be of narrowband character (cf. section 4.3). To demonstrate the temporal and spectral purity of this light, a TICO-Raman spectrum with the 1186 nm pulses as Raman pump pulses was recorded. The spectrum is shown in Figure 7.7. As SRS spectra rely critically on the linewidths of the laser sources and the temporal overlap, this spectrum of benzene around the narrowband peak at 992 cm^{-1} demonstrates the quality of this pump light. Furthermore, it demonstrates the spatially single-mode character of the 1186 nm light, as the SRS spectrum depend on the spatial focal overlap between pump and Stokes laser.

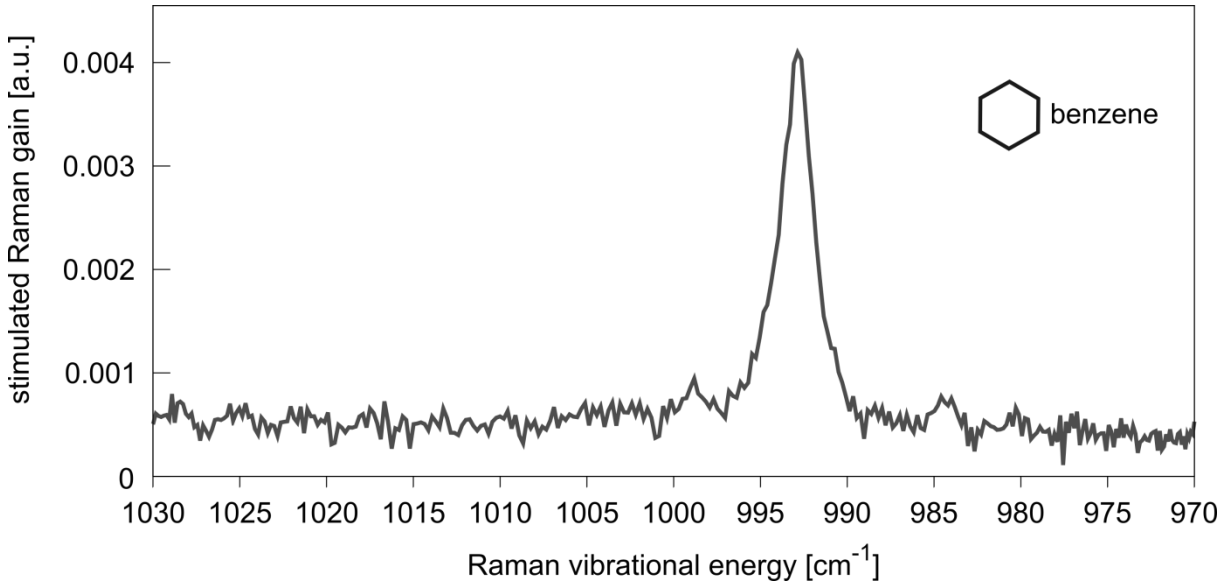

Figure 7.7: SRS spectrum of the narrowband transition of benzene at 992 cm^{-1}. As pump the shifted pump wavelength at 1186 nm was used. For the SRS signal the transmission change on an FDML laser around 1350 nm was recorded.

7.3. Comparison to spontaneous Raman spectrum

The TICO-Raman spectra have broadband coverage and high resolution. It is interesting to compare it to a state-of-the-art spontaneous Raman spectrum in order to assess the quality. Figure 7.8 presents a comparison between a TICO-Raman spectrum and a spontaneous Raman spectrum from the SDBS database [38]. The data was extracted from the literature spectrum and carefully normalized to the TICO-Raman spectrum, as is explained in the supplementary information of [12]. The spectrum of cyclohexane shows very good agreement regarding both the wavenumber value axis and the relative peak heights. Only the peak at 802 cm^{-1} is higher in the TICO-Raman spectrum, which may be due to the high-resolution of the TICO-Raman technique[22]. SRS has a natural advantage with the limit in resolution given by the laser linewidth in contrast to the spectrometer limit in spontaneous Raman systems. Thus, the comparison in Figure 7.8 shows the high accuracy and the quality obtained by the TICO-Raman technique.

[22] Unfortunately, the resolution of the spectrometer used in the recording of the literature spectrum [38] is not known. For future measurements, it would be interesting to obtain the data of a spontaneous Raman spectrum and compare the integrated area below the peaks which should be of the same value.

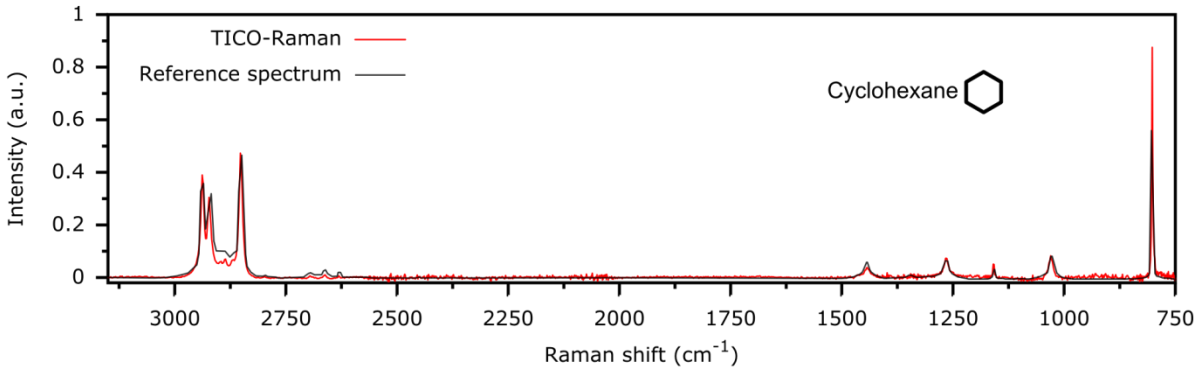

Figure 7.8: Comparison of a TICO-Raman spectrum of cyclohexane with a spontaneous Raman spectrum from the SDBS database [38]. Both the signal height and the Raman energy axis show very good agreement. Only the peak at 802 cm^{-1} shows a difference, where the TICO-Raman system records a higher signal. This is probably due to its high spectral resolution which helps to better resolve the narrowband peak.

7.4. Dynamical spectral zooming

The FDML laser allows to electronically adjust its sweeping range [5] by changing the voltage applied to the swept Fabry-Pérot filter. In the TICO-Raman setup, this can be used to adjust the spectral coverage, and with it the spectral resolution of the Raman spectra. This is demonstrated in Figure 7.9 which shows a Raman spectrum of a chemical mixture of benzene, cyclohexane and toluene in equal parts. First, a broader Raman spectrum was acquired with a spectral coverage of 650 cm^{-1} (blue spectrum), corresponding to a sweeping range of the FDML Stokes laser of 106 nm. Now by electronically lowering the sweeping range from ~106 nm to ~15 nm (red curve), the spectral coverage is reduced to 90 cm^{-1} and at the same time the spectral resolution is enhanced. This higher resolution, shown in the lower right graph, helps to better resolve the narrow and closely spaced peaks. This feature is called dynamical spectral zooming, as it is possible to dynamically enhance the resolution simply by changing the voltage applied to the swept filter without adjusting any optical component. If this technique can be applied to SRS spectroscopy of gases [35], it may be possible to first record a broadband survey spectrum to identify the substance and then zoom into the rotational bands to study e.g. the temperature of a sample [39].[23]

[23] Of course, improvements in laser linewidths and power values may need to be made in order to probe gases by SRS.

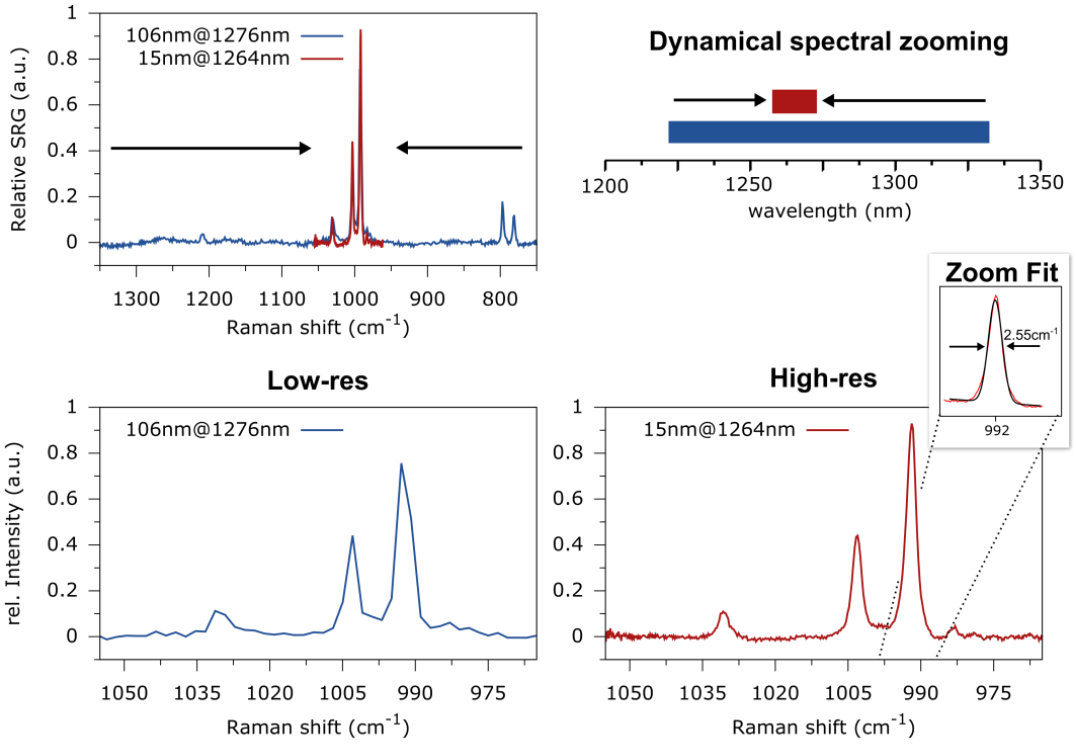

Figure 7.9: Dynamical spectral zooming made possible by the wavelength swept FDML laser. Reducing the electronical sweeping range of the FDML laser also reduces the Raman spectral coverage. This increases the spectral resolution. This zooming into spectral regions allows to better resolve narrowband features, like the aromatic modes in this spectrum of a mixture of benzene, cyclohexane and toluene. The fit on the 992 cm^{-1} band of benzene results in a 2.55 cm^{-1} FWHM width (see zoom fit inlay), which agrees well with a literature value of 2.4cm^{-1} [40].

7.5. Fast spectrum at 6.4 kHz spectral acquisition rate

The spectral acquisition rate can be increased by reducing the number of spectral points per spectrum. This also lowers the number of sweeps of the FDML laser needed to record a TICO-Raman spectrum. Figure 7.10 shows a TICO-Raman spectrum of toluene acquired in only 157 µs corresponding to a spectral acquisition rate of ~6.4 kHz. The spectrum has an SNR of 11, so the two peaks of toluene at 1002 cm^{-1} and 1030 cm^{-1} are clearly visible.

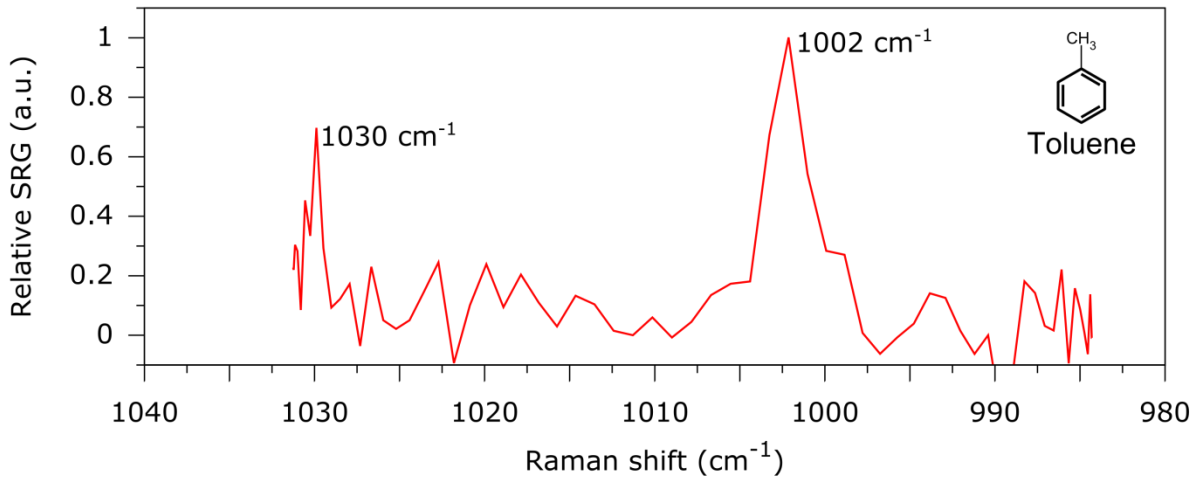

Figure 7.10: Fast spectrum of toluene acquired at a spectral acquisition rate of 6.4 kHz. The FDML laser was swept at 415 kHz. Together with a spectrum consisting of 64 spectral points, this corresponds to a total acquisition time of just 157 µs for the spectrum. The TICO-Raman spectrum shows the two-peaks of toluene at 1002 cm^{-1} and 1030 cm^{-1}. This unaveraged spectrum has an SNR of ~11.

7.6. Sparse sampling

An interesting question is how the speed of the spectral acquisition can be increased. In the current implementation only one spectral point per FDML period is acquired. Thus, the number of spectral points mostly determines the speed of the spectra. Faster spectra can easily be acquired by sacrificing spectral points or applying multiple pulses per sweep, as will be presented in section 7.8. Reducing the number of spectral points results in less information in the Raman spectrum. Nevertheless, sometimes only few specific Raman energies are of interest. This is the case if, for example, one only looks for a ratio of two chemicals. Then, sparse sampling of only the Raman transitions of interest can greatly increase the speed. This is schematically presented in Figure 7.11. If two species A and B are to be discerned by their specific Raman transitions, few samples are needed to sample the Raman peaks. In this case, a sparsely sampled spectrum may contain enough information and hence increase the acquisition speed.

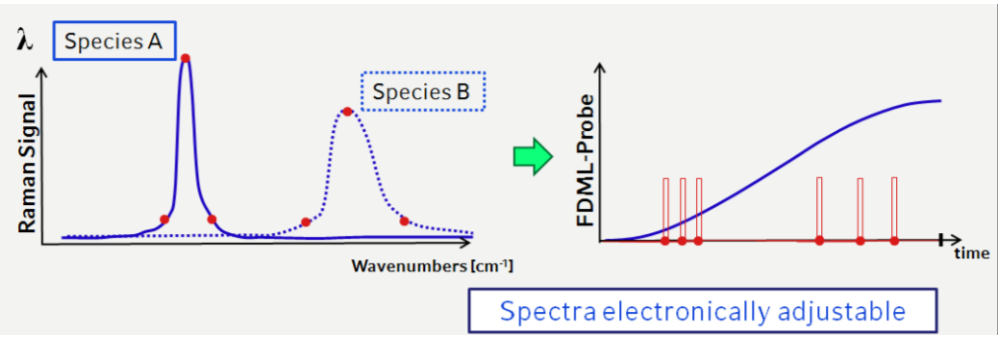

Figure 7.11: The concept of sparse sampling visualized in a schematic figure. In order to identify a species through its Raman band, it is often sufficient to just sample sparsely over the Raman band. This of course requires prior knowledge on the absolute peak position, i.e. the knowledge of the sample constituents. Then, only few samples are needed to detect the constituents. This sparse sampling can increase measurement speed. This is easily achieved in the setup, as the waveforms, i.e. the sampling positions can be programmed and are set electronically.

Experimentally, this can be done by reducing the spectral points sampled by the pump laser, i.e. by programming corresponding waveforms on the AWG. This was done experimentally and the result is shown in Figure 7.12, where a Raman spectrum of dimethyl sulfoxide (DMSO) was measured. The left, blue spectrum consists of 64 spectral points and took 157 µs to record. The right, green spectrum is a sparsely sampled spectrum. It consists of only 8 spectral points which corresponds to an 8-fold speed increase. The measurement time was only 22 µs.[24]

As is evident from Figure 7.12, the increase of speed comes at the cost of spectral resolution and information. Also, the center wavelength of the FDML needs to be controlled very precisely in order to ensure that the sample for the Raman peak remains at the maximum position, otherwise the SNR would suffer.

[24] Note that this is not a factor of 8, because a blank sweep is added at the end of each AWG waveform, as was explained in section 6.2.

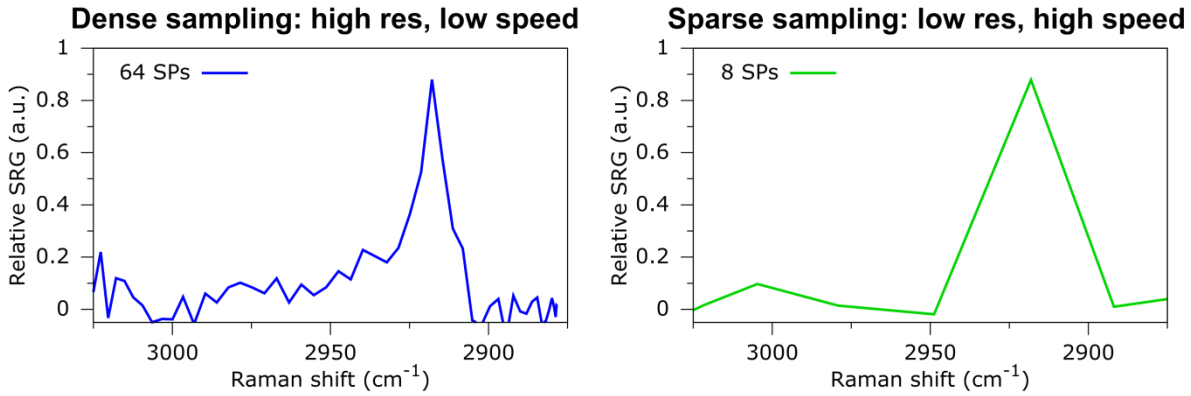

Figure 7.12: Experimental data showing sparse sampling of DMSO. The Raman spectrum of DMSO was acquired with 64 spectral points (left) and 8 spectral points (right), resulting in an 8-fold increase in speed. The spectral acquisition rate increased from 6.4 kHz to 46 kHz.

7.7. Spectral synthesis

A great advantage of SRS is the linearity in sample concentration. The SRG effect scales linearly with the number of molecules in the probe volume, whereas e.g. in CARS it scales quadratically. This makes SRS a reliable tool for quantitative analysis. In order to show the great analytical and synthetic capabilities of SRS, a mixture of three chemicals was recorded and the individual spectra of each constituent. First, the mixture of equal parts of cyclohexane, benzene and toluene was recorded. Figure 7.13 shows the TICO-Raman spectrum of the mixture. Then, three spectra of the neat chemicals were measured individually (Figure 7.14). The individual spectra were then added arithmetically, each weighted by 1/3 for the concentration in the mixture. The comparison between the linear combination and the measured mixture shows very good agreement (Figure 7.15). This proves the reliability and the reproducibility of the TICO-Raman system and can be used in the future to quantify concentrations of substances in unknown samples. The Raman energy and the unique combination of the different spectral features allow identification of substances and the peak height allows quantification of the molecules.

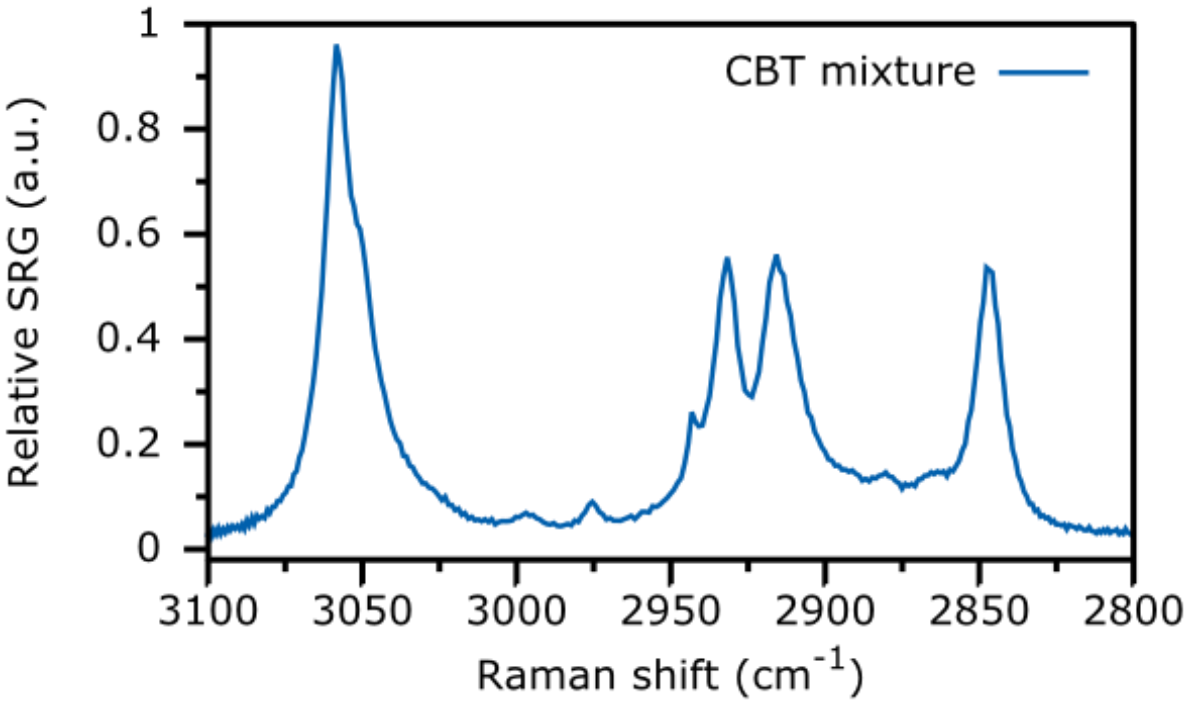

Figure 7.13: The spectrum of the chemical mixture of equal parts of cyclohexane, benzene and toluene.

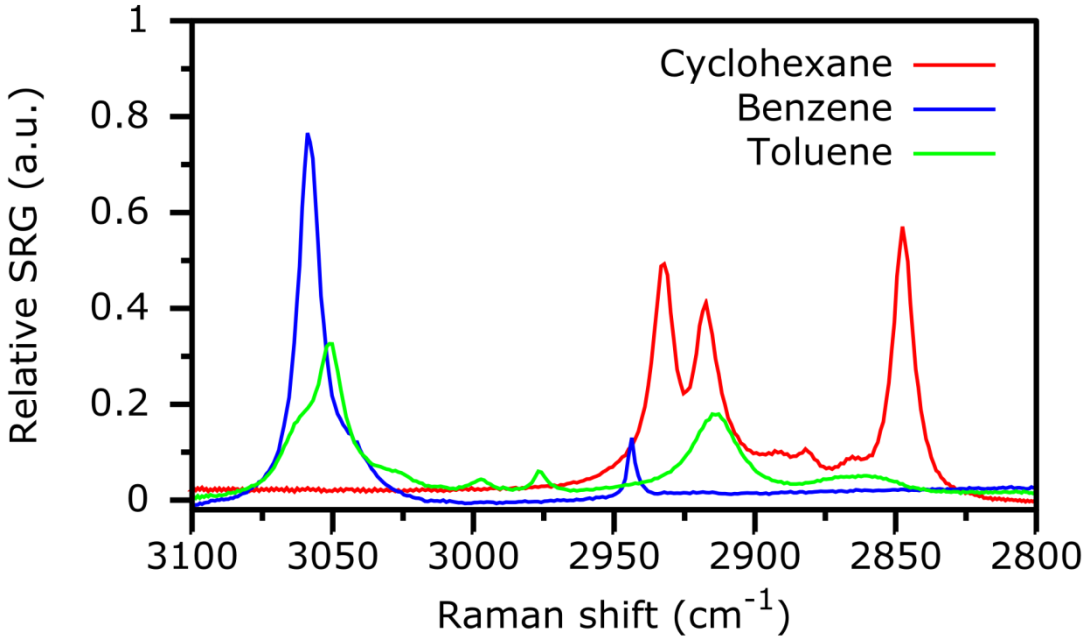

Figure 7.14: The individual spectra of the chemicals cyclohexane, benzene and toluene.

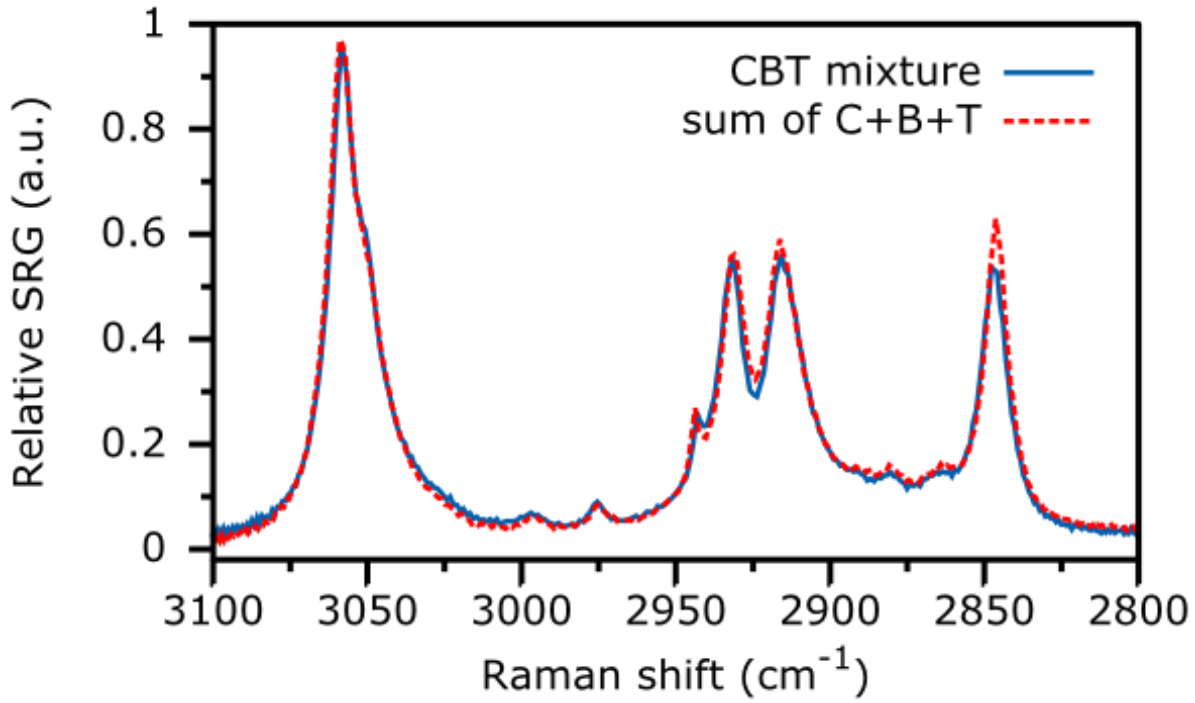

Figure 7.15: Comparison between the spectrum of the mixture (cf. Figure 7.13) and the mathematical sum of the individual spectra. Both match very well which proves the synthetic quality of the TICO-Raman system. This can also be used analytically to deduct ratios of chemicals through their Raman bands.

7.8. Spectrum with over 1 million spectral points per second

An interesting question is whether the speed of the TICO-Raman technique can be increased by probing more than one Raman transitions per sweep. The FDML laser covers a broad SRS spectrum within one sweep, so in principle it should be possible to obtain a Raman spectrum within a single sweep. Therefore, when a pulsed pump is used, many pulses need to be applied per sweep. Of course, this increases the average power on the sample if the pulse length is maintained. In Figure 7.16 a TICO-Raman spectrum with 1.3 MHz pulse repetition rate is shown, where 10 pulses were applied per sweep. Therefore, the AWG was programmed with a waveform with 640 samples per FDML sweep, i.e. 1280 samples per FDML period. With an FDML frequency of 55 kHz, this corresponds to a sample clock frequency of 70.4 MHz on the AWG. In order to keep a nearly constant repetition rate, both the forward and the backward sweep of the FDML were raster-scanned by pump pulses. This ensured nearly identical pump peak powers, as the YDFAs were CW-pumped and thus an equal time between the pulses ensures equivalent gain. The Raman spectrum from the backward sweep was then inversed, as the backward sweep has an inverse sinusoidal sweep in wavelength.

A problem with these long waveforms on the AWG (1280*65=83200 samples per waveform) is that the phase of the FDML relative to the first pump pulse can only be set

coarsely. This phase adjusting, as was already explained in section 5.3 and Figure 6.7, is important in order to assign accurate Raman wavenumber values. Nevertheless, the AWG can only set the phase in 3600 individual steps, which is too few for these long waveforms. This was circumvented by adjusting the phase in the best manner possible on the AWG[25] and then digitally in LabVIEW. Thereby, the spectrum from the backward sweep was rotated by an empirically determined number of samples (found by matching the main Raman peak) so that the Raman peaks overlap. This means, however, that some samples are on the wrong end of the Raman spectrum[26] and thus the calculation of the Raman transition energies is not entirely accurate. This minute deviation is also seen as the peaks of toluene and benzene are shifted by about 5 cm^{-1} on the spectrum shown in Figure 7.16 with respect to their known peak positions.

The spectrum presented here, despite the MHz rate of the spectral point acquisition, was averaged over 3200 waveform periods, which corresponds to a total of 6400 averaging. Shorter acquisition times were not possible in this preliminary experiment, as the high average power on the sample did not permit adjusting the parameters (alignment, overlap etc.) for higher SNR, which made higher averaging necessary. Nevertheless, this spectrum already demonstrates that multiple pulses per sweep are possible and spectra with higher than MHz pulse repetition rates are feasible.

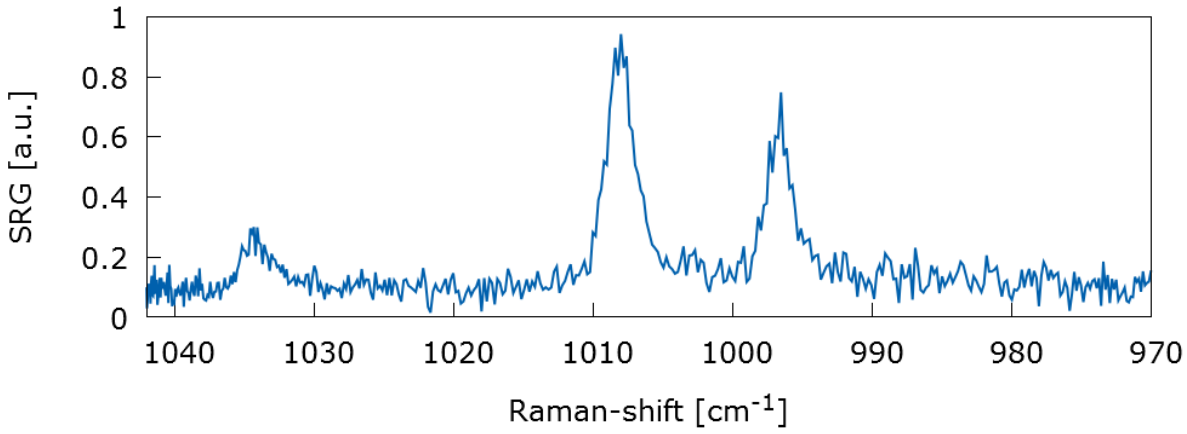

Figure 7.16: TICO-Raman spectrum of a mixture of toluene and benzene acquired with a spectral point acquisition rate of 1.3 MHz. This spectrum is averaged 6400-times, as is explained in the text.

[25] Note, that here 83200/3600=23,11. So, every phase adjustment step shifts the waveform by 23 samples, which is not an integer divider of a single FDML waveform. By shifting multiple waveforms one can set the first pump pulse very close to the start of a sweep.

[26] For clarification: If the first pulses do not coincide with the start of the sweep but rather with the end of the last sweep, the wavenumbers are not correctly assigned.

8. TICO Raman hyperspectral microscopy

Raman scattering allows label-free identification of molecules [4]. When applied to microscopy, the Raman signal can offer a molecular contrast [36, 41-47]. This makes Raman microscopy a very interesting imaging tool for biomedical applications [36, 44, 47]. SRS is a great candidate since it provides high signal enhancement factors (usually ~10^6) which lead to a faster acquisition time, often crucial for biological imaging. There exist several systems capable of acquiring SRS microscopy images [36, 45] with some systems even pushing the imaging speed up to video rate [44, 48]. However, at these speeds only one Raman transition is probed. The need for a fast imaging system with pixelwise spectral acquisition still prevails [49]. Furthermore, a system is needed which has broad spectral coverage and is endoscope ready through a fiber-based design [50].

The use of an FDML laser [5] for SRS microscopy can provide the aforementioned advantages. The fast wavelength sweeps over a broad spectral range (i.e. ~1000 cm^{-1} within 1 µs) are ideally suited for rapid fiber-based SRS hyperspectral imaging [12]. Acquiring a spectrum at every pixel allows choosing the Raman transitions in post-processing. In most systems, the molecular distribution is known prior to the acquisition, which is crucial if only one transition is recorded. Nevertheless, this does not apply to unknown tissue for real in vivo microscopy. Therefore, a hyperspectral Raman image is necessary. In hyperspectral imaging it is further possible to apply advanced filtering techniques like Savitzky-Golay filtering [45] or principal component analysis (PCA) / independent component analysis (ICA) [44] which can enhance the molecular recognition and/or the SNR of the images.

8.1. Setup

In order to add the imaging modality to the TICO-Raman setup, the beams need to be raster-scanned over the sample. The common approach using galvanometric mirrors provides very fast beam steering, but the scanning over the focusing lenses can lead to beam aberrations when not passing centrally through the lenses. Therefore, microscope objectives are commonly used which provide minimal aberrations and additionally are corrected for chromatic errors. Unfortunately, at long near-infrared wavelengths only few corrected microscope objectives are available and preliminary tests did not achieve the needed specifications of chromatic correction and transmission values. Thus, aspheric lenses (Thorlabs C230TM-C) were used, which have high transmission and a high numerical aperture NA= 0.55. For beam steering, the sample was moved instead of the beam for these preliminary images. Therefore, the sample was mounted on a three-dimensional translational stage, which allowed moving the sample into the focal volume in z-direction and then providing x-y-beam scanning for imaging. The intensity changes were measured in

transmission. A large-diameter photodiode (Fermionics FD300W) on the detector was installed in order to collect the most light possible. A shutter was installed on the pump beam in order to minimize exposure on the sample. This shutter opened only upon recording and closed upon the carriage return for a new line. Each pixel was recorded in LabVIEW Software just like in the spectroscopy setup. The image array was a three dimensional array with a spectrum at each pixel and, in the header, one wavenumber array for the vibrational energies (x-axis) of the Raman spectra. The translational stages were driven in synchronization with the imaging software. The speed of the stages was calculated based on the laser repetition rate, the number of spectral points, the number of spectral points per sweep, the number of averaging per spectrum and the pixel pitch.

For first imaging tests, a Siemens star was mounted on the stage and the transmission intensity was measured (Figure 8.1). To the left and to the right of the image, the acceleration and de-acceleration paths are visible as a distortion of the image. In the center a washout of the edges is visible which is due to the high speed of the stages. When they are driven at over 2 mm/s (2.5 mm/s in this image), the stages show velocity ripples which result in the image washout visible here. Thus, for imaging the velocity was kept below 1 mm/s (cf. **Figure 8.2**).

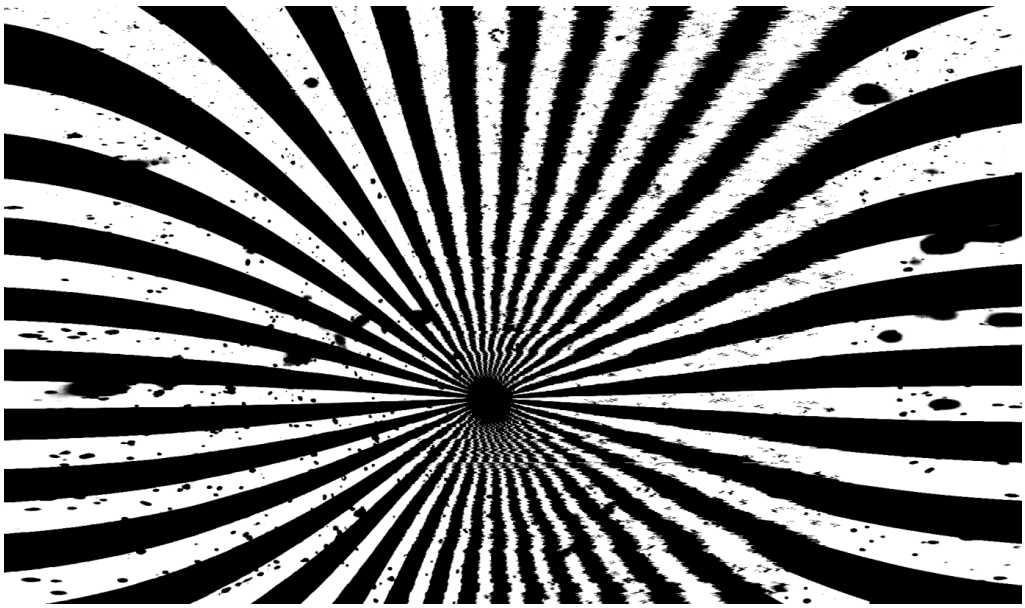

Figure 8.1: Imaging of a Siemens star allowed debugging of the imaging software and adjusting the imaging parameters (like e.g. speed of the stages, acceleration values, etc.). The image has 2048x1200 pixels and represents approx. 8 mm x 6 mm physical size. The high speed (>2mm/s) of the translational stages produced velocity ripples resulting in the “wavy” edges in the middle of the image. As a consequence, the velocity was kept below 1 mm/s for further imaging.

Figure 8.2: Image of a Siemens star acquired with slower speed at the translational stages. This slower speed prevents the "wavy" washout due to the velocity ripples of the stages (cf. Figure 8.1).

8.2. Results

For hyperspectral Raman imaging, the 415 kHz FDML setup was used. With one spectral point per FDML period, this results in an acquisition time of 2.4 µs per spectral point. Figure 8.4 shows a hyperspectral TICO-Raman image of Polymethymethacrylate (PMMA) and Polystyrene (PS) beads, which are hardly discernible through a transmission image contrast (see Figure 8.3) but easily through their different Raman signatures (Figure 8.4). At each pixel, a 32-point spectrum around 3000 cm^{-1} was acquired and 8-times averaged. This 480x320 pixel image (1 µm pixel pitch) then allows for choosing the visualization of Raman vibrational modes in post-processing. Two intrinsic Raman transitions were chosen; one was the C-H stretching mode of PS around 3050 cm^{-1} with blue color coding and the band at 2950 cm^{-1} of PMMA in red for molecular contrast representation. Figure 8.5 shows these single channels. To the right are spectra of the molecules at the points indicated. For better visualization of the spectra (Figure 8.5 B,D), 5x5 pixels were averaged and Savitzky-Golay filtered (three side points and second order polynomials). For the images, the single pixel spectra were Savitzky-Golay filtered followed by integration over the Raman bands (indicated by colored boxes under the peaks). This integration enhanced the SNR for higher imaging contrast. Finally, appropriate cut-levels were set to optimize the signal levels to the 8-bit image representation and maximize contrast.

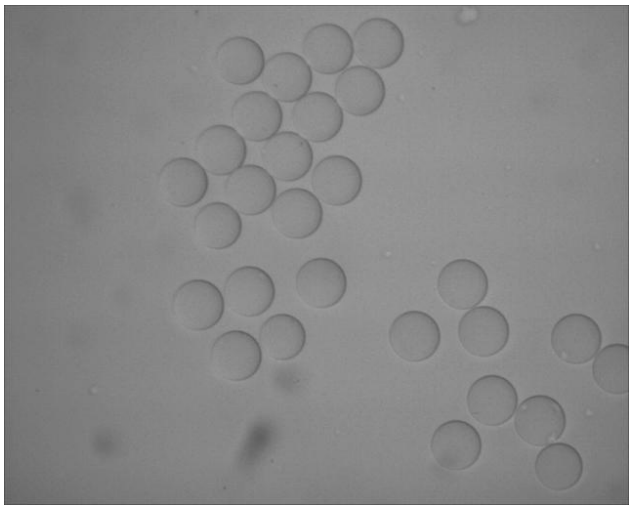

Figure 8.3: Standard bright-field microscopy image of PS and PMMA beads. The beads are not discernable by their transmission microscopy contrast.

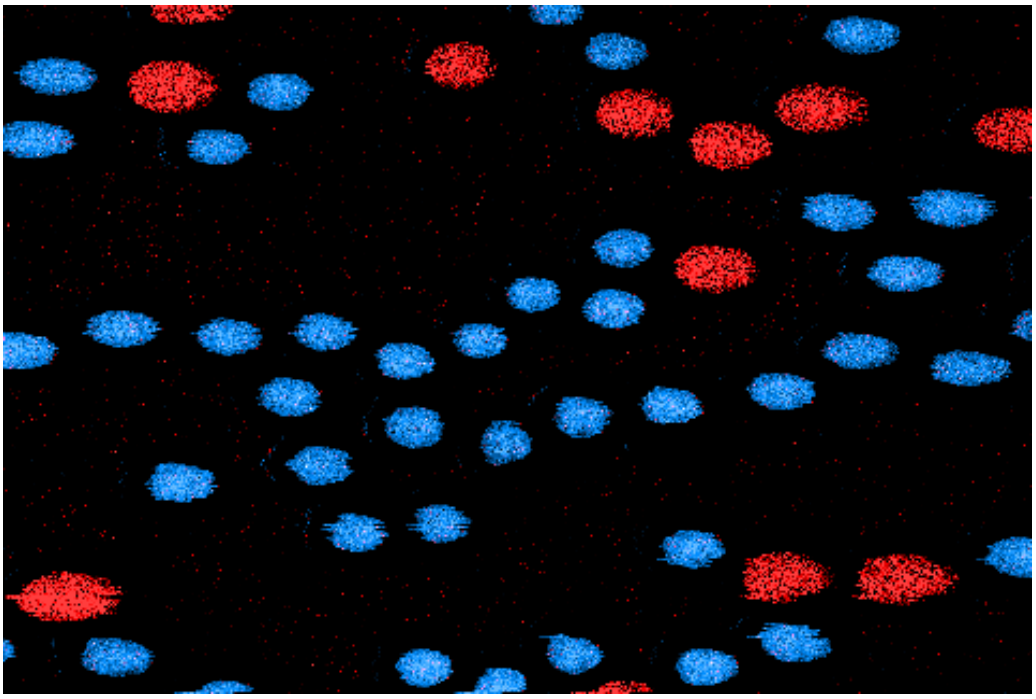

Figure 8.4: Hyperspectral Raman image of polystyrene (red) and polymethylmethacrylate (PMMA, blue) beads. The beads are 20 µm in diameter. The image is 480x320 pixel with 1 µm pixel pitch. At each pixel a 32-point TICO-Raman spectrum was acquired and 8-times averaged.

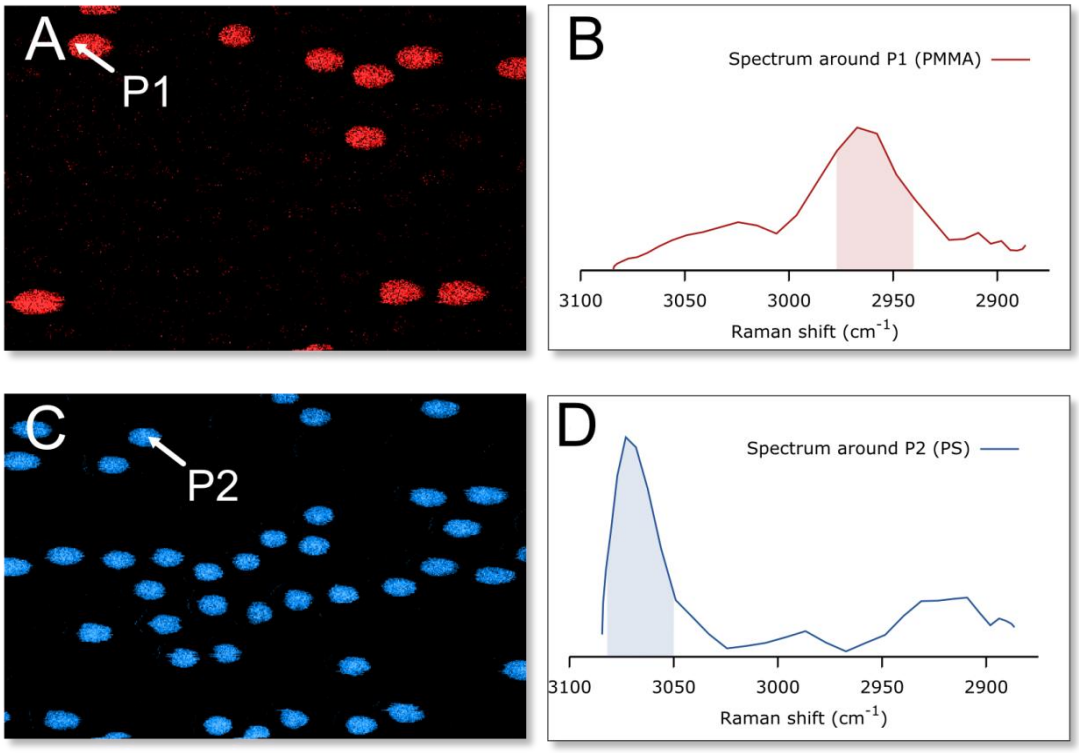

Figure 8.5: The single channels of the PS/PMMA Raman image. (A) shows the molecular vibration of PMMA around 2960 cm^{-1}. (B) The respective spectrum of PMMA around P1. The spectrum was Savitzky-Golay filtered and 5x5 pixels were averaged for this spectral representation. For imaging, only the single pixel spectra were used and the Raman peaks were averaged for higher contrast. The red area shows the spectral region used for integration. (C,D) Show the respective blue color-coding of PS and the spectrum around P2 with the typical peak around 3060 cm^{-1} used for visualization.

The polymer beads already showed good imaging contrast and proved the applicability of the TICO-technique to hyperspectral Raman imaging. It was examined whether this can be used in biological tissues and extended to the fingerprint region (below 2000 cm^{-1}) where the peaks are of more narrowband character and are thus better distinguishable. Unfortunately, most substances provide a much weaker signal in the fingerprint region [44], so imaging requires more averaging and thus longer imaging times.

As a biological sample a slice of a plant stem was chosen as it provides a cellular structure. Figure 8.6 shows a transmission microscopy image of a slice of *geranium phaeum* stem, acquired with the same system by removing the pump blocking filters. The sample was immersed in olive oil, which can provide a Raman contrast by probing lipid vibration around 1660 cm^{-1}. The olive oil diffuses inside the cells and provides a molecular contrast filling up the insides of the cells. Further, lignin is a natural Raman scatterer which is found in cell walls. The word derives from the Latin word *lignum* which translates to “wood”, meaning this is the substance that provides the plants’ stiffness. Lignin has a molecular vibration around 1600 cm^{-1}. Both Lignin and olive oil are thus Raman scatterers in the fingerprint region. This sample can be of interest for imaging with Raman microscopy as a modern field of research is

looking for enzymes that can produce mineral oil (fossil fuels) substitutes from biomass and lignin is found to hinder the conversion efficiency [43]. An instrument to visualize these processes without adding labels is of high importance [43, 51].

Figure 8.6: Transmission microscopy image of a sliced *geranium phaeum* stem. This morphological image was acquired by detecting the transmission power of the pump beam.

Figure 8.7 shows a hyperspectral Raman image of the slice recorded with the TICO-Raman system. At each pixel a spectrum consisting of 64 spectral points was acquired and 100-times averaged. The power of the pump laser at 1064 nm was 480 mW and 3.3 mW for the FDML probe laser[27]. Lignin was color coded in red and olive oil in blue through their respective Raman vibrational bands. The corresponding TICO-Raman spectra are shown in Figure 8.8 B,D. These spectra were taken at points P1 and P2 indicated by arrows in the individual channel images in Figure 8.8 A,C. The spectra were Savitzky-Golay filtered and offset corrected by a 2^{nd} order polynomial[28]. The high resolution of the TICO-Raman system is advantageous for imaging in the fingerprint region, as can be seen here. Even though, the two peaks are only 60 cm^{-1} apart, they are clearly distinguishable and can be used efficiently to visualize the two different constituents.

[27] The power levels used here are higher than in common picosecond SRS systems by about a factor of 10, which is probably possible as nanosecond pulses are used and the wavelength is at 1064 nm as opposed to 800 nm. A more detailed discussion can be found in [12].

[28] More info can be found in the supplementary material to reference [12].

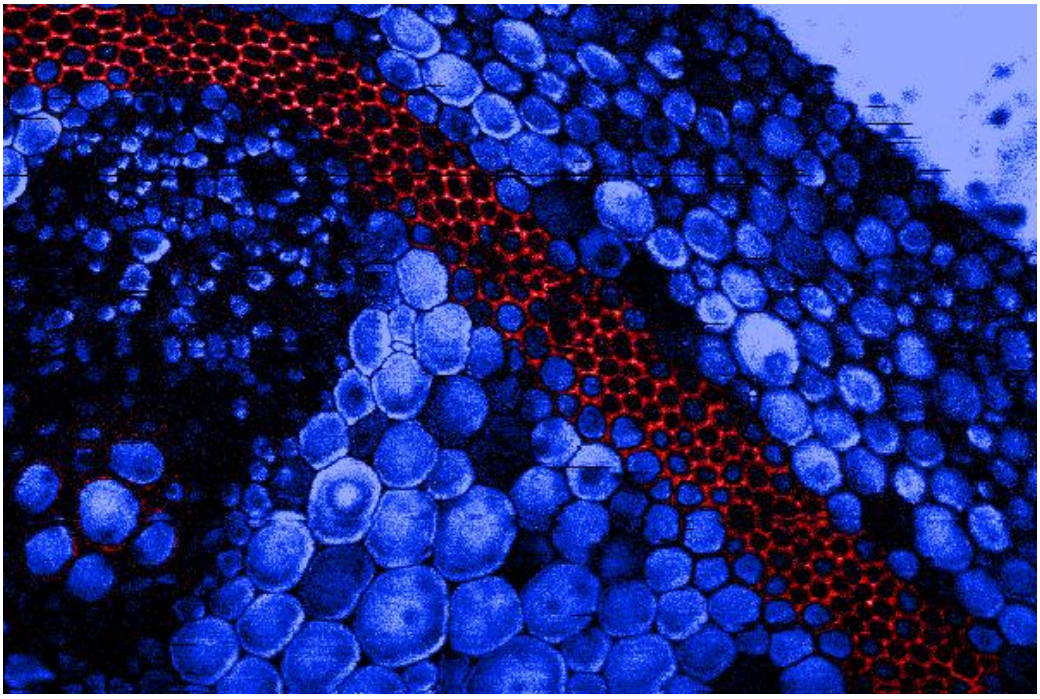

Figure 8.7: Hyperspectral TICO Raman microscopy image of a sliced geranium phaeum stem. Shown in red is lignin through its Raman transition around 1600 cm^{-1}. Olive oil, which was diffused in the sample, is color coded in blue through its' molecular vibration around 1660 cm^{-1}.

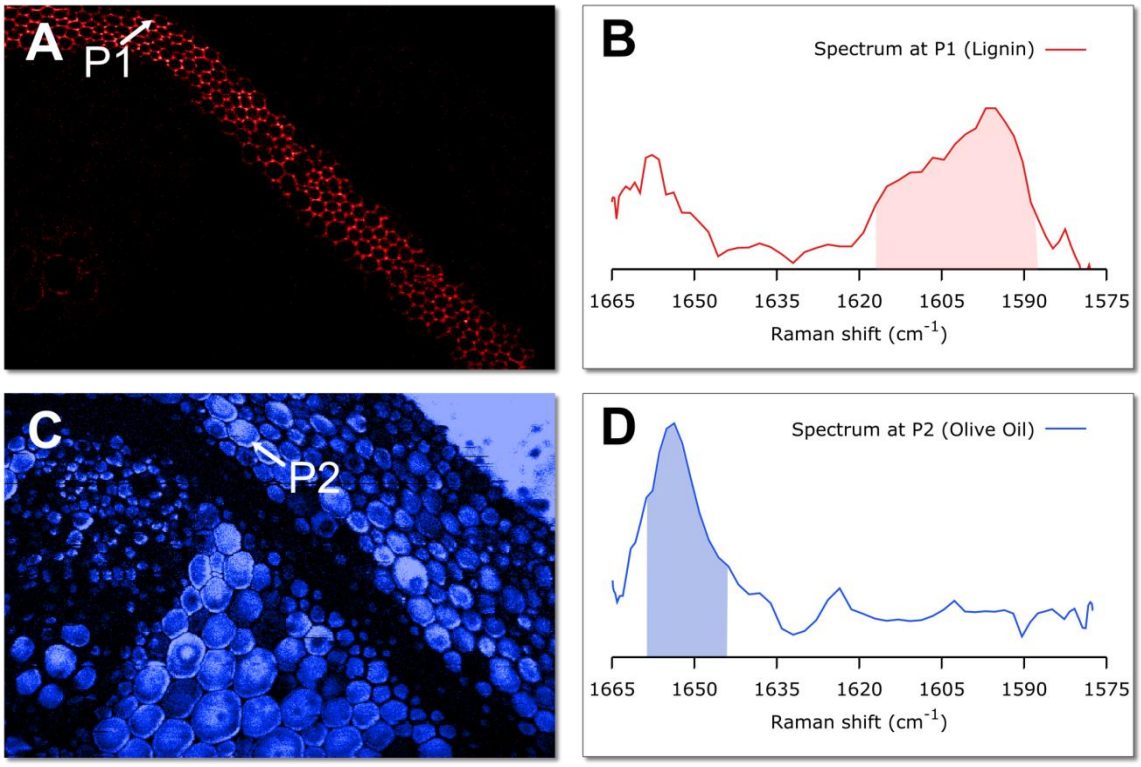

Figure 8.8: The single channels of the hyperspectral TICO-Raman image of *geranium phaeum*. (A) shows the molecular vibration of lignin in the fingerprint region around 1600 cm^{-1}. (B) The respective spectrum of lignin at P1. The spectrum was Savitzky-Golay filtered. The red area shows the spectral region over which was integrated for the lignin visualization. (C,D) Show the respective blue colour-coding of olive oil and the spectrum at P2 with the aromatic vibration around 1660 cm^{-1} used for visualization.

The Raman contrast provides insight into the molecular composition of a sample. This is a feature that is not possible in conventional microscopy and is often times only reached by staining the sample in histology or by exploiting fluorescence labeling [52, 53]. To visualize this insight, which is gained by Raman imaging, Figure 8.9 shows a morphological overlay of the simple transmission microscopy image and the color coded hyperspectral Raman image. The lignin and olive oil distributions are made visible with the aid of the Raman contrast. The colored image reveals that not all the cell walls contain significant amounts of lignin, but mostly the sclerenchyma and the xylem.

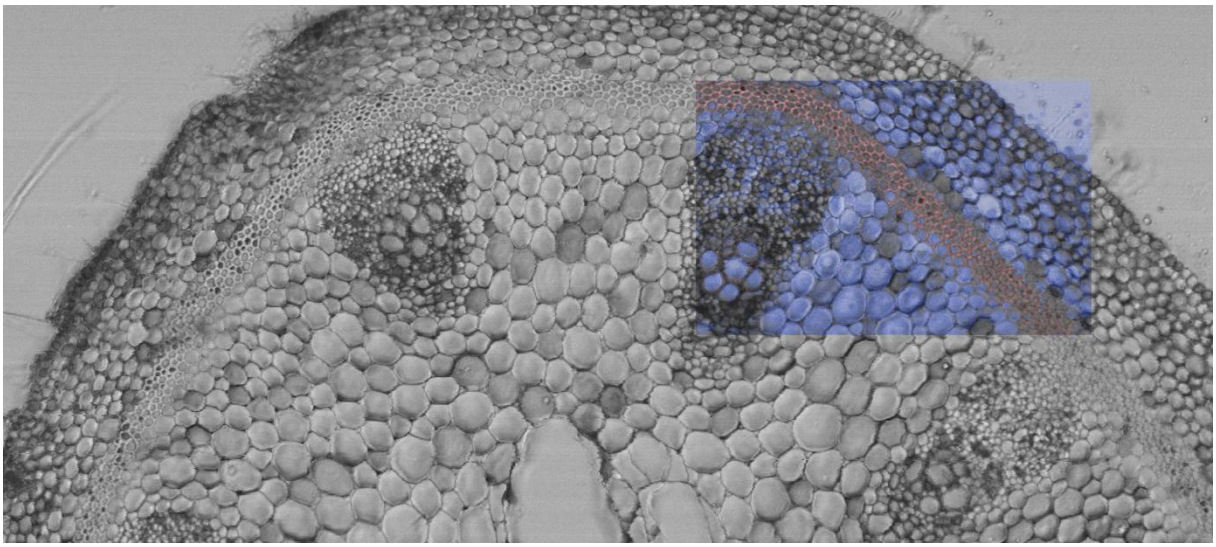

Figure 8.9: Morphological overlay of the hyperspectral TICO-Raman image and the transmission microscopy image. Although the transmission image already has high detail and resolution, individual functional sites cannot be distinguished. Adding the Raman contrast helps to identify the diffusion of olive oil in the sample and the distribution of lignin in the cell walls.

9. TICO multi-photon microscopy

The TICO-Raman system is ideally suited to provide a manifold of imaging contrasts, making it a highly promising multi-modal imaging platform. Already the FDML probe laser is used for fastest OCT [5, 14, 54-59] even with real-time volumetric image display [60]. Another non-linear imaging technique is now introduced by the high power pulses of the fiber MOPA pump laser in combination with the high numerical aperture (NA) focusing. The intensity reaches GW/cm^2 values, capable of inducing multi-photon absorption processes and suited for multi-photon imaging [61]. The multi-photon absorption processes can lead to second-harmonic generation (SHG), third-harmonic generation (THG) or two-photon excited fluorescence (TPEF). The great advantages of multi-photon processes are the deeper penetration depth in biological tissue due to the longer wavelength (usually double the wavelength of comparable one-photon fluorescence microscopes) and, due to its non-linearity, the high spatial resolution in the axial direction. This is the result of a quadratic behavior in intensity that renders multi-photon processes highly localized to the immediate focal volume.

In this chapter multi-photon imaging with the TICO system is presented. First, the theoretical description applied to the nanosecond pulses is presented. Then, the obtained multi-photon signal is experimentally verified. As the sample is already mounted on a translational stage, TPEF imaging of autofluorescence of plant leaves, moss and algae was recorded.

In the future, this multi-photon imaging of samples providing either autofluorescence or samples that have been engineered with specific marker fluorophores can be used to visualize functional parts of a tissue sample, like e.g. gene expression [52]. This can provide a comprehensive picture of the sample under investigation when combined with SRS and OCT.

9.1. Theory

The effect of non-linear, two-photon absorption (TPA) was first theoretically described in 1931 by Maria Goeppert-Mayer [62]. It is a very weak effect, as it requires the simultaneous absorption of two photons. Thus only with the advent of highly coherent light from lasers it was first experimentally observed by Kaiser and Garrett in 1961 [63]. Insight is gained by first looking at the equation for calculating the number of absorbed photons per fluorophore (after [61]):

$$n_a = \frac{p_0^2 \delta}{\tau_p f_p^2} \left(\frac{NA^2}{2\hbar c \lambda} \right)$$

where p_0 is the average power, δ the 2-photon absorption cross section, τ_p the pulse length, f_p the pulse repetition rate, NA the numerical aperture used for focusing, and λ the excitation wavelength. This formula was written for the commonly used scenario, where ultra short pulses (~100 fs) are used at high repetition rates (~80 MHz). Nevertheless, it is more instructive to rewrite this equation using $p_0 = p_{peak} \tau_p f_p$ to:

$$n_a = p_{peak}^2 \tau_p \delta \left(\frac{NA^2}{2\hbar c \lambda} \right)$$

where p_{peak} is the peak power. This means that the number of absorbed photons scales quadratically with the peak power and the NA, and is linear in the pulse duration[29]. In the TICO-system, where nanosecond pulses are used, the number of multi-photon absorption events n_a can be equivalently high to short pulse systems. In fact, if the peak power p_{peak} is the same as in short pulse systems, the linear dependence in pulse duration can lead to a 10.000-fold increase[30] in multi-photon absorption. Of course, the repetition rate needs to be reduced by the same amount in order to keep the average power below the sample damage threshold (i.e. 8 kHz instead of 80 MHz). This can be somewhat counterbalanced in practice, as the 1064 nm (and longer) excitation light of the TICO-system often permits significantly higher average powers on the sample than the common 800 nm, so even higher repetition rates are possible. Studies have shown that at 1064 nm usually ten times higher power than at 800 nm can be used [64]. Another advantage of a lower and adjustable repetition rate is that it can be adjusted to the fluorescence lifetime. The 12.5 ns between pulses in the common 80 MHz systems lie in the natural fluorescence lifetime range, so with some samples, lower repetition rates are wanted, which can be actively adjusted in the presented TICO-system.

A last but strong advantage of the nanosecond pulses is the high compatibility to fiber delivery and endoscopic probes without the need for chromatic dispersion management nor measures for omitting self-phase modulation (SPM).

9.2. Setup

The setup of the TICO multi-photon microscope is presented in Figure 9.1. The setup is the same as in the TICO-Raman setup, but here only the fiber MOPA pump laser is used for excitation. For the detection either an avalanche photodetector (APD) or a highly sensitive photomultiplier tube (PMT) with adjustable gain is used. The signals are recorded in epi-

[29] This holds, of course, only in the regime where enough sites are available for absorption.
[30] As nanosecond pulses are 10.000-times longer than 100 fs pulses.

direction, i.e. in the backward direction of the illumination. In order to separate the excitation light from the faint multi-photon light, a series of dichroic mirrors (DM) is employed. The signal is digitized on a personal computer (PC) using the same software in LabVIEW as for the Raman measurements. This means, only the samples of the fast ADC where a multi-photon signal occurs are recorded. This time-encoded (TICO) detection helps to detect the whole signal while omitting any background light. This is a further advantage to conventional multi-photon microscopes which integrate over many pulses and thus are also sensitive to spurious background light. Furthermore, this TICO approach can also be used to detect multiple signals on only one channel of the ADC by time-multiplexing. If e.g. TPEF, SHG and THG signals are present, these can be filtered by appropriate filters and all sent to a single photomultiplier, after being retarded in time by appropriate delay times. This means that all these different signals arrive at the detector sequentially in time and can then be sequentially recorded by a single detector and a single digitizer. Through the time-multiplexed setup the signals can thus be identified individually. In the presented setup, only one signal was recorded simultaneously.

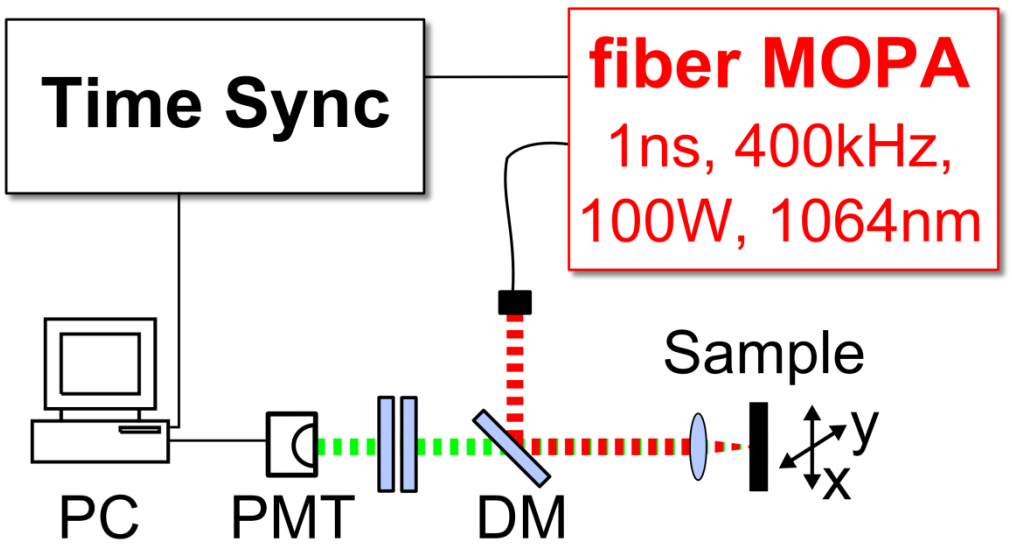

Figure 9.1: The schematic setup of the TICO multi-photon microscopy system. The nanosecond pulses from the fiber MOPA are focused on the sample with a high NA lens. The sample is mounted on a three-dimensional translational stage. The TPEF signals are detected in epi-direction. The excitation light is filtered by a series of dichroic mirrors (DM). The photomultiplier tube (PMT) detects smallest amounts of TPEF light. The image is reconstructed on a personal computer (PC). Here, the detection is driven synchroneously to the excitation to fully recover the signal and omit background light through the TICO technique.

9.3. TPEF confirmation

For first verification of the multi-photon signal, rhodamine 6G was dissolved in methanol and 100 W pulses were used at 1 ns pulse length and 415 kHz repetition rate. A fluorescence signal was observed and a photo was taken with a smartphone camera (Figure 9.2). Even though the camera was also sensitive to scattered excitation light at 1064 nm, this light was clearly distinguishable from the orange fluorescence light by its color. The 1064 nm light resulted in a white image signal and was not seen inside the sample but rather behind the setup on a photothermal detector where the power of the 1064 nm light was measured.

Figure 9.2: Photography of the TPEF signal of rhodamine 6G in methanol. This photography shows the orange fluorescence signal of the fluorophore after multi-photon excitation with intense 1064 nm light.

After this first observation, the fluorescence light was examined both spectrally and for its dependence on the pump power. The spectral output is shown in Figure 9.3. This proofs that the signal is at higher energies than the excitation light, indicating TPEF origin.

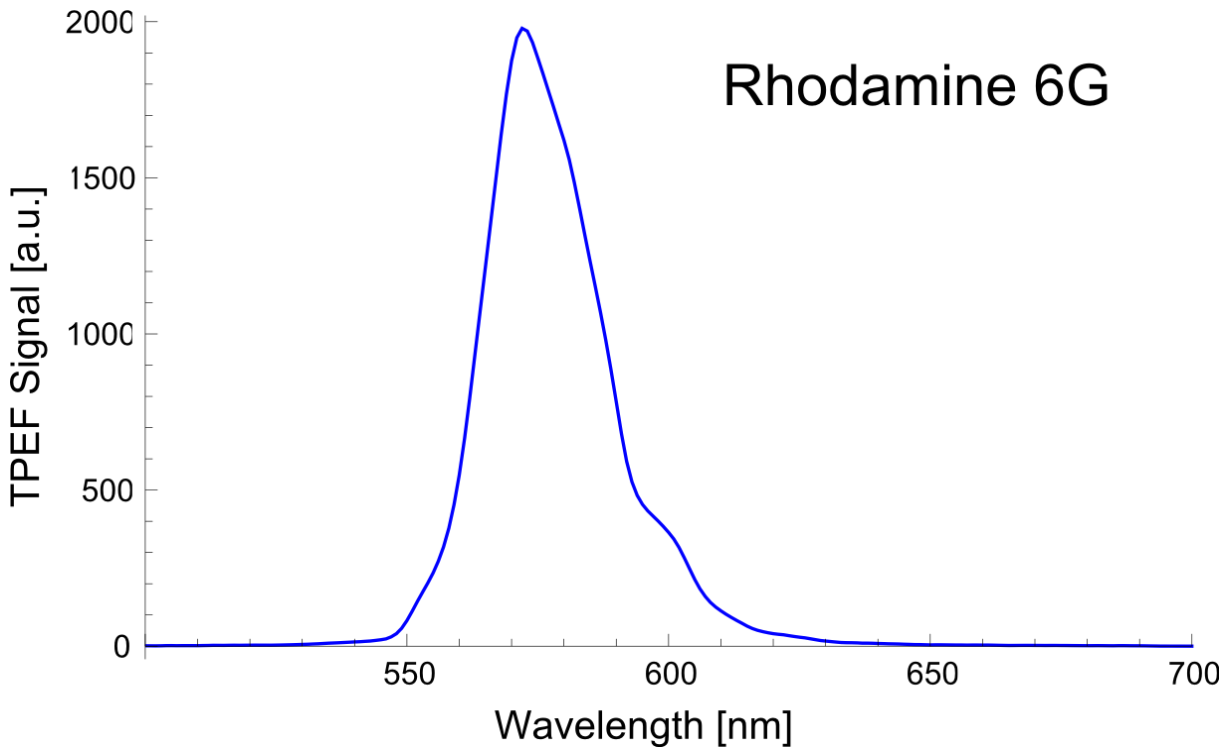

Figure 9.3: The emission spectrum of rhodamine 6G dissolved in methanol indicates the TPEF origin of the scattered light. The emission is at higher energies than the excitation light (lower wavelength) and is shifted from exactly double the energy (i.e. emission peak at ~575 nm instead of half the pump wavelength at 532 nm), as expected by TPEF.

Further, the quadratic dependence of the TPEF signal on the pump power was verified (Figure 9.4). A quadratic fit was calculated for pump powers up to 38 W which proves the quadratic dependence (blue curve). At higher pump powers, a minute deviation is visible, which is supposedly due to a saturation effect in the sample. For comparison, also a linear curve based on the slope of the first two measurement points was included (green curve) which shows that the observed signal behaves strongly non-linear on the pump power.

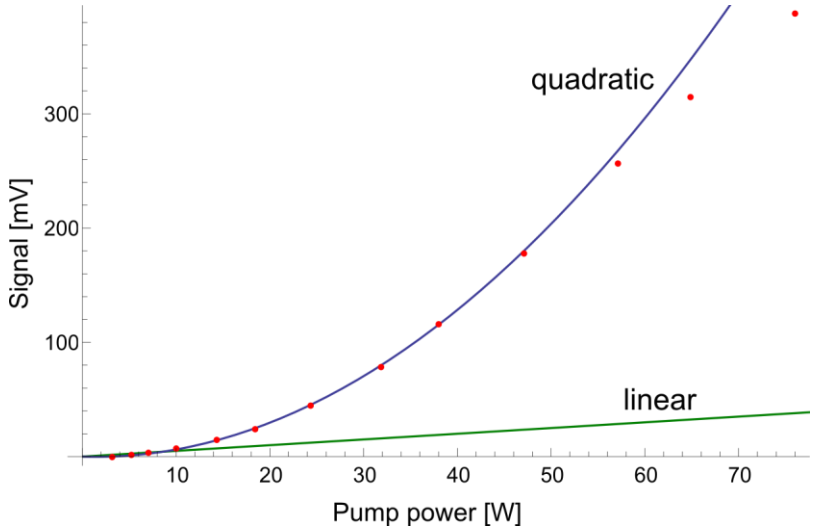

Figure 9.4: Confirmation of the quadratic behavior of the TPEF signal on the pump power. The red dots are the measured TPEF signals which clearly follow a quadratic fit (blue curve). The fit was calculated for small pump powers, as for higher pump powers a deviation is visible, probably due to a saturation effect. For comparison linear behavior is also shown (green), confirming the non-linearity of the observed TPEF signal.

9.4. TPEF Imaging

For TPEF imaging, the sample was raster-scanned with a pixel pitch of 1 µm. The naturally occurring autofluorescence of plant leaves was used for the TPEF contrast. The images were obtained by the following procedure: First, the intensity values for each pixel were casted to 8-bit integers. Therefore, the 16-bit integers from the ADC were taken and appropriate cut-levels for high and low value ranges set and then extrapolated to harvest the whole 8-bit range for the image. This means, that the lowest intensity value is set to 0 and the maximum intensity to 255. Then, for logarithmic scale images, the 16-bit integers from the ADC were calculated to a logarithmic scale (after the cut levels were set) and extrapolated to 8-bit values. Finally, the images were tinted green in GIMP 2 to apply a natural looking color.

The imaging speed here is limited by the translational stages. With a translational speed of 1 mm/s and a 1 µm pixel pitch, this holds a maximum of 1000 pixels/s. Nevertheless, already a single pulse creates a TPEF signal with enough SNR for imaging, so speed can in the future be increased by faster beam steering with galvanometric mirrors.

The pulse duration of the pump pulse was 0.5 ns at 120 W peak power and a repetition rate of 415 kHz. As the maximum imaging speed was already limited by the translational stages to 1000 pixel/s, the same waveforms as for the hyperspectral Raman images (cf. chapter 8) were used. For each pixel, the TPEF signal was 20-times averaged and a "spectrum", i.e. an array of 64 identical signals was acquired. Usually, the redundant data was omitted and only one point was used for the images. Conveniently, the slow acquisition could also be harnessed for high SNR imaging by averaging, as is shown in Figure 9.7.

Figure 9.5 shows a TPEF image of a leave of a snowdrop (g*alanthus*). The image consists of 2048x1005 pixels.

Figure 9.6 is a TPEF image of *algae*. This high contrast image consists of 2048x840 pixels.

Figure 9.7 presents a comparison of averaging on a TPEF image of moss. The left image (Figure 9.7 A) shows the 1400x3000 pixel image with 20-fold averaging per pixel. In the right image (Figure 9.7 B) the pixel were obtained by averaging over the whole "spectrum" obtained, thus by averaging 64*20=1280 pulses. The high SNR together with the logarithmic representation enables visualizing even minute SHG occurring on water droplets (see Figure 9.7 B1).

Figure 9.8 shows a comparison of the TPEF image of moss with a standard bright-field microscopy image. The zoom-in on the leave (Figure 9.8 A2) has a high contrast as only the inside of the cells are visible (probably due to carotene in the cells) and the outside is black. In the standard microscopy image (Figure 9.8 B) the leaf is visible but also the surrounding medium including dust particles and other impurities surrounding the plant leaf. Thus, the TPEF image can provide higher contrast images by visualizing only the scatterers with non-linear TPEF contributions.

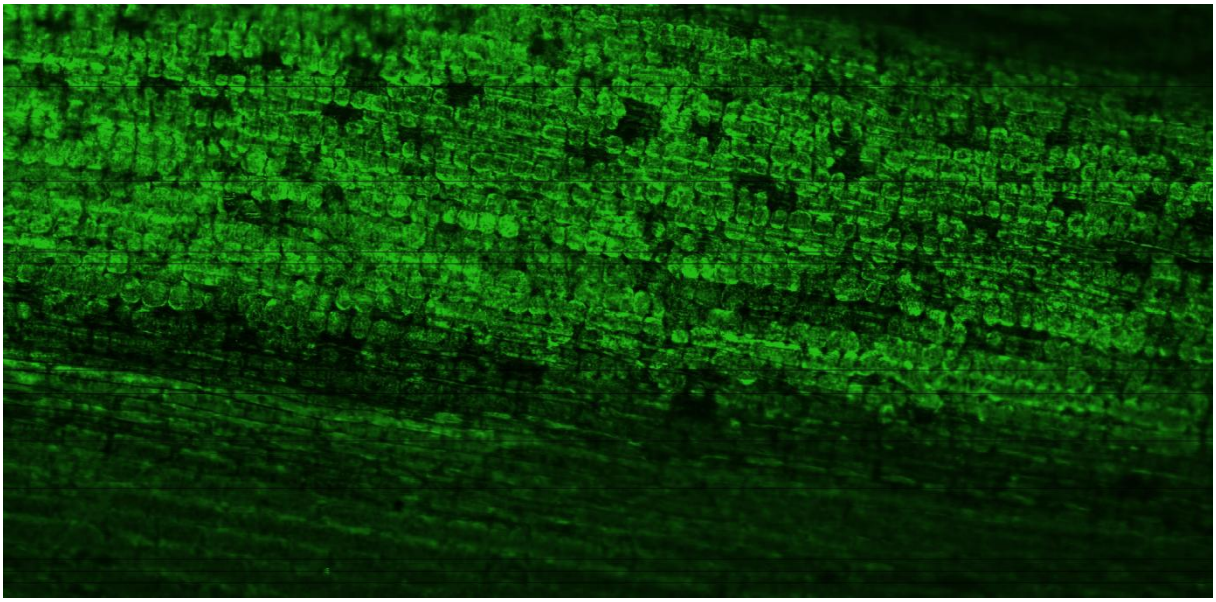

Figure 9.5: TPEF image of a snowdrop leaf. The endogenous autofluorescence of the plant leave is highly localized to interior of the cells. The image dimensions are 2048x1005 pixels with a 1 µm pixel pitch.

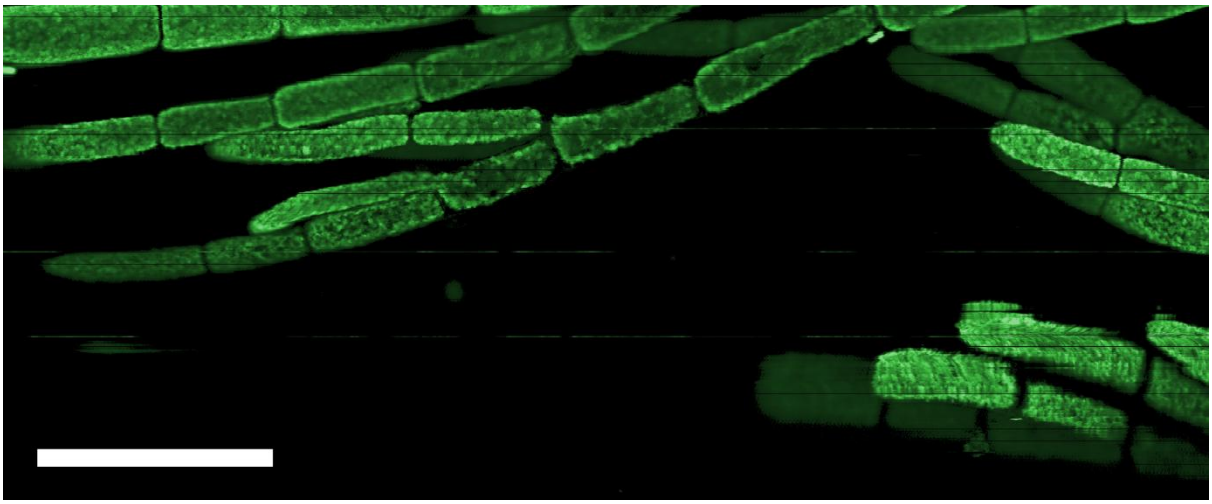

Figure 9.6: TPEF image of *algae*. The image consists of 2048x840 pixels, the scale bar corresponds to 400 µm.

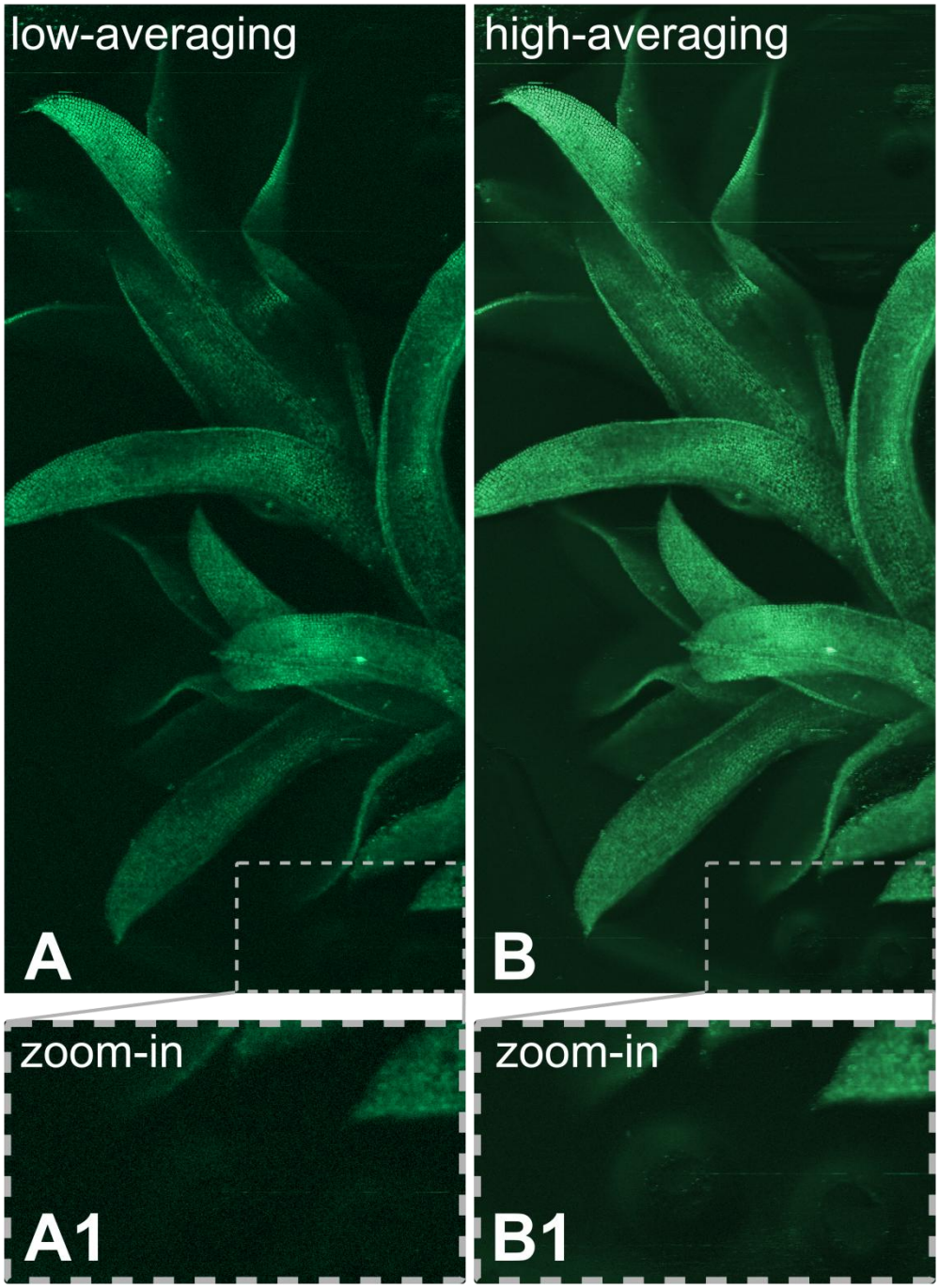

Figure 9.7: TPEF image of *moss* with different amount of averaging. Images A,B contain of 1400x3000 pixels with 1 µm pixel pitch. In image A each pixel averaged 20 pulses, in image B each pixel averaged 1280 pulses. Both images are on a logarithmic scale. Note the high depth range of the images. A1 and B1 show zoom-ins into a region, where SHG on surfaces is visible (most likely water droplets).

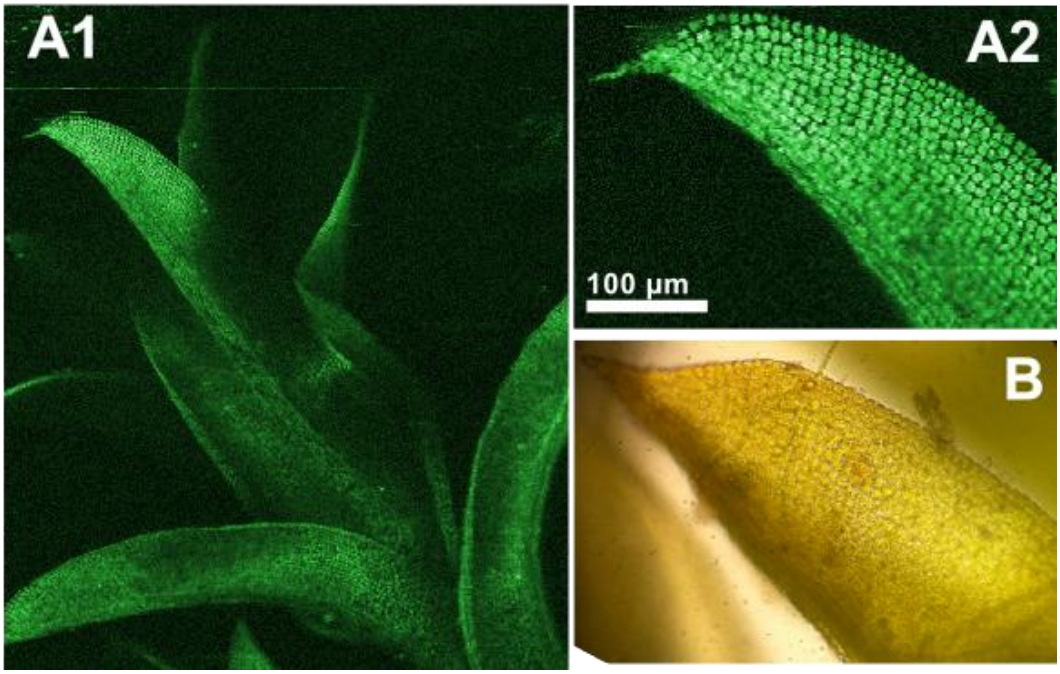

Figure 9.8: TPEF imaging comparison with standard microscopy image. (A1) is a TPEF image of moss. (A2) is a detail zoom-in to a moss leave. For comparison, a standard microscopy image of a similar moss leave is presented in (B). The TPEF image is only sensitive to the interior of the cells, providing much higher contrast than the standard bright-field microscopy image, which shows even minute scatterers in the surrounding medium.

For the future, the TPEF imaging modality can be explored by functionalizing samples with different fluorophores, taking advantage of the multi-color functionality of the fiber-based MOPA light source. By choosing of a broad range of engineered fluorophores, one can functionalize different parts of a sample with different fluorophores corresponding to the excitation wavelengths. For example, rhodamine 6G can be excited by the 1064 nm output, while Alexa Fluor 546 and Texas Red can be excited by 1122 nm and 1186 nm, respectively.

Furthermore, also SHG and THG imaging can be harnessed for a more comprehensive picture of the sample through multi-modal imaging [65].

10. Conclusion, Outlook

This thesis described the design of a new system for non-linear Raman spectroscopy using rapidly wavelength swept lasers. The TICO technique was implemented with two homebuilt light sources. The whole system was developed to produce high resolution spectra with broadband coverage. It was applied to SRS spectroscopy of chemicals.

Furthermore, the system was applied to hyperspectral Raman microscopy with pixelwise Raman spectrum acquisition. First images of biological samples with molecular contrast were recorded. In addition, multi-photon absorption imaging was performed with this system. This was made possible with the newly developed, multi-color pump laser. TPEF was used as a contrast to enable multi-photon microscopy (MPM) of biological plants with sub-cellular resolution.

This system thus has the capability of providing a multi-modal imaging platform for biomedical applications. It would be interesting to combine the outstanding potential of the FDML laser for fastest OCT [59, 60] together with non-linear imaging through hyperspectral SRS microscopy and MPM.

Another possibility of the TICO technique would be to enable the measurement of TPEF and fluorescence lifetime imaging (FLIM) in a single-shot time-based method. This could increase the speed of FLIM microscopy by reducing the number of pulses needed for recording the lifetime decay down to a single pulse.

As further upcoming goals of this system, there are several strategies to enrich the field of biomedical imaging. As a short-term goal, the imaging speed has to be increased. For SRS imaging, the probe power has to be increased in order to enhance the SNR. Several amplification techniques are available (like e.g. SRS [12] or rare-earth doped fibers [66]), but need to be investigated for broadband amplification capability, noise contribution and power limitations. Another important measure is the spectral acquisition speed. The probe laser already sweeps up to 1000 cm^{-1} per microsecond. If it would be possible to obtain a Raman spectrum within one sweep, MHz spectral rate would be possible. As a first step, 10 spectral points per FDML sweep were acquired by applying multiple pulses to one sweep. However, imaging speed is always limited by the maximum power the sample can handle. This sets a limit to the maximum number of pulses per sweep as the pulse length is bound to the speed of the digitizers (which, on the bright side, are becoming faster and faster every year). There exist several envisaged ideas in the group to increase the speed and further research will show how effective these will be at increasing the speed for the TICO system.

Another important speed improvement must be implemented by faster beam steering mechanisms like polygon or galvanometric mirrors. For TPEF imaging already a single pulse provides sufficient SNR for TPEF imaging, so with faster scanning images with 256x256 pixels would be already possible at 6 frames per second. For Raman, this faster scanning needs to be supported by the focusing lenses, as SRS depends highly on the overlap of the two

beams. Furthermore, if measuring in transmission, the probe beam must be de-scanned by appropriate, synchronized mechanical systems. Therefore, and for imaging applications *in vivo*, detection in epi-direction would be highly desirable and pose another important goal for the future.

A long term goal would be the use of a fiber endoscope for non-linear imaging. The whole system is already fiber-based and the quasi-continuous wave (quasi-CW) laser sources have a big advantage to the commonly used femtosecond or picosecond systems, as dispersion and SPM are not an issue. Therefore, appropriate endoscope optics with high numerical aperture (NA) for MPM and no chromatic errors for perfect two-beam overlap need to be engineered.

Bibliography

1. Raman, C.V. and K.S. Krishnan, "A new type of secondary radiation", *Nature*, **121**, 501-502, 1928.
2. Woodbury, E.J., Ng, W.K., "Correspondence", *Proceedings of the IRE*, **50**, 2365-2383, 1962.
3. Maker, P.D. and R.W. Terhune, "Study of Optical Effects Due to an Induced Polarization Third Order in the Electric Field Strength", *Physical Review*, **137**, A801-A818, 1965.
4. Owyoung, A. and E.D. Jones, "Stimulated Raman spectroscopy using low-power cw lasers", *Optics Letters*, **1**, 152-154, 1977.
5. Huber, R., M. Wojtkowski, and J.G. Fujimoto, "Fourier Domain Mode Locking (FDML): A new laser operating regime and applications for optical coherence tomography", *Optics Express*, **14**, 3225-3237, 2006.
6. Eigenwillig, C.M., et al., "Picosecond pulses from wavelength-swept continuous-wave Fourier domain mode-locked lasers", *Nat Commun*, **4**, 1848, 2013.
7. Boyd, R.W., *Nonlinear optics*. 2008, Burlington, Mass., U.S.A.: Academic Press.
8. Heiman, D., et al., "Raman-Induced Kerr Effect", *Physical Review Letters*, **36**, 189-192, 1976.
9. Levenson, M.D. and N. Bloembergen, "Dispersion of the nonlinear optical susceptibility tensor in centrosymmetric media", *Physical Review B*, **10**, 4447-4463, 1974.
10. Lago, L., et al., "Single-mode narrow-bandwidth temporally shaped nanosecond-pulse ytterbium-doped fiber MOPA for a large-scale laser facility front-end", *Journal of the Optical Society of America B*, **27**, 2231-2236, 2010.
11. Eibl, M., "Stimulated Raman Spectroscopy with a Rapidly Wavelength Swept Laser", Technical University Munich and Ludwig-Maximilians-University Munich, Diploma thesis, 2012.
12. Karpf, S., et al., "A Time-Encoded Technique for fibre-based hyperspectral broadband stimulated Raman microscopy", *Nature Communications*, **6**, 2015.
13. Karpf, S., et al., "Multi-color fiber MOPA with electronically switchable wavelength shifter for non-linear laser spectroscopy", *in preparation*, 2015.
14. Klein, T., et al., "Megahertz OCT for ultrawide-field retinal imaging with a 1050nm Fourier domain mode-locked laser", *Optics Express*, **19**, 3044-3062, 2011.
15. Krishnan, R.S., "The scattering of light in fused quartz and its Raman spectrum", *Proceedings of the Indian Academy of Sciences - Section A*, **37**, 377-384, 1953.
16. Stolen, R.H. and E.P. Ippen, "Raman gain in glass optical waveguides", *Applied Physics Letters*, **22**, 276-278, 1973.
17. Feng, Y., L.R. Taylor, and D.B. Calia, "150 W highly-efficient Raman fiber laser", *Optics Express*, **17**, 23678-23683, 2009.
18. Smith, R.G., "Optical Power Handling Capacity of Low Loss Optical Fibers as Determined by Stimulated Raman and Brillouin Scattering", *Applied Optics*, **11**, 2489-2494, 1972.
19. Ippen, E.P. and R.H. Stolen, "Stimulated Brillouin scattering in optical fibers", *Applied Physics Letters*, **21**, 539-541, 1972.
20. Lee, H. and G. Agrawal, "Suppression of stimulated Brillouin scattering in optical fibers using fiber Bragg gratings", *Optics Express*, **11**, 3467-3472, 2003.
21. Pei-juan, G., et al., "Stimulated raman scattering up to 10 orders in an optical fiber", *Applied physics*, **24**, 303-306, 1981.

22. Rosman, G., "High-order comb spectrum from stimulated raman scattering in a silica-core fibre", *Optical and Quantum Electronics*, **14**, 92-93, 1982.
23. Stolen, R.H., C. Lee, and R.K. Jain, "Development of the stimulated Raman spectrum in single-mode silica fibers", *Journal of the Optical Society of America B*, **1**, 652-657, 1984.
24. Stolen, R.H. and J.E. Bjorkholm, "Parametric amplification and frequency conversion in optical fibers", *Quantum Electronics, IEEE Journal of*, **18**, 1062-1072, 1982.
25. Malitson, I.H., "Interspecimen Comparison of the Refractive Index of Fused Silica", *Journal of the Optical Society of America*, **55**, 1205-1208, 1965.
26. Huang, D., et al., "Optical coherence tomography", *Science*, **254**, 1178-1181, 1991.
27. Lexer, F., et al., "Wavelength-tuning interferometry of intraocular distances", *Applied Optics*, **36**, 6548-6553, 1997.
28. Golubovic, B., et al., "Optical frequency-domain reflectometry using rapid wavelength tuning of a Cr^{4+};forsterite laser", *Optics Letters*, **22**, 1704-1706, 1997.
29. Chinn, S.R., E.A. Swanson, and J.G. Fujimoto, "Optical coherence tomography using a frequency-tunable optical source", *Optics Letters*, **22**, 340-342, 1997.
30. Haberland, U.H.P., V. Blazek, and H.J. Schmitt, "Chirp Optical Coherence Tomography of Layered Scattering Media", *Journal of Biomedical Optics*, **3**, 259-266, 1998.
31. Yun, S.H., et al., "High-speed spectral-domain optical coherence tomography at 1.3 μm wavelength", *Optics express*, **11**, 3598-3604, 2003.
32. Huber, R., D.C. Adler, and J.G. Fujimoto, "Buffered Fourier domain mode locking: unidirectional swept laser sources for optical coherence tomography imaging at 370,000 lines/s", *Optics Letters*, **31**, 2975-2977, 2006.
33. Biedermann, B.R., et al., "Dispersion, coherence and noise of Fourier domain mode locked lasers", *Optics Express*, **17**, 9947-9961, 2009.
34. Eigenwillig, C.M., et al., "K-space linear Fourier domain mode locked laser and applications for optical coherence tomography", *Optics Express*, **16**, 8916-8937, 2008.
35. Owyoung, A., C.W. Patterson, and R.S. McDowell, "Cw stimulated Raman gain spectroscopy of the ν1 fundamental of methane", *Chemical Physics Letters*, **59**, 156-162, 1978.
36. Freudiger, C.W., et al., "Label-Free Biomedical Imaging with High Sensitivity by Stimulated Raman Scattering Microscopy", *Science*, **322**, 1857-1861, 2008.
37. Ekvall, K., et al., "Cross phase modulation artifact in liquid phase transient absorption spectroscopy", *Journal of Applied Physics*, **87**, 2340-2352, 2000.
38. SDBSWeb: http://sdbs.riodb.aist.go.jp, National Institute of Advanced Industrial Science and Technology, accessed 03.03.2014.
39. Bohlin, A., et al., "Pure rotational CARS measurements of temperature and relative O2-concentration in a low swirl turbulent premixed flame", *Proceedings of the Combustion Institute*, **34**, 3629-3636, 2013.
40. Owyoung, A. and P.S. Peercy, "Precise characterization of the Raman nonlinearity in benzene using nonlinear interferometry", *Journal of Applied Physics*, **48**, 674-677, 1977.
41. Gierlinger, N., T. Keplinger, and M. Harrington, "Imaging of plant cell walls by confocal Raman microscopy", *Nat. Protocols*, **7**, 1694-1708, 2012.
42. Bégin, S., et al., "Coherent anti-Stokes Raman scattering hyperspectral tissue imaging with a wavelength-swept system", *Biomedical Optics Express*, **2**, 1296-1306, 2011.
43. Ding, S.-Y., et al., "How Does Plant Cell Wall Nanoscale Architecture Correlate with Enzymatic Digestibility?", *Science*, **338**, 1055-1060, 2012.
44. Ozeki, Y., et al., "High-speed molecular spectral imaging of tissue with stimulated Raman scattering", *Nat Photon*, **6**, 845-851, 2012.

45. Ploetz, E., et al., "Femtosecond stimulated Raman microscopy", *Applied Physics B*, **87**, 389-393, 2007.
46. Ideguchi, T., et al., "Coherent Raman spectro-imaging with laser frequency combs", *Nature*, **502**, 355-358, 2013.
47. Saar, B.G., et al., "Imaging Drug Delivery to Skin with Stimulated Raman Scattering Microscopy", *Molecular Pharmaceutics*, **8**, 969-975, 2011.
48. Saar, B.G., et al., "Video-Rate Molecular Imaging in Vivo with Stimulated Raman Scattering", *Science*, **330**, 1368-1370, 2010.
49. Camp JrCharles, H., et al., "High-speed coherent Raman fingerprint imaging of biological tissues", *Nat Photon*, **8**, 627-634, 2014.
50. Rigneault, H. and E. Andresen, "Microscopy: Fast and label-free", *Nat Photon*, **6**, 802-803, 2012.
51. Saar, B.G., et al., "Label-Free, Real-Time Monitoring of Biomass Processing with Stimulated Raman Scattering Microscopy", *Angewandte Chemie*, **122**, 5608-5611, 2010.
52. Chalfie, M., et al., "Green fluorescent protein as a marker for gene expression", *Science*, **263**, 802-805, 1994.
53. Giepmans, B.N.G., et al., "The Fluorescent Toolbox for Assessing Protein Location and Function", *Science*, **312**, 217-224, 2006.
54. Adler, D.C., et al., "Three-dimensional endomicroscopy using optical coherence tomography", *Nat Photon*, **1**, 709-716, 2007.
55. Adler, D.C., R. Huber, and J.G. Fujimoto, "Phase-sensitive optical coherence tomography at up to 370,000 lines per second using buffered Fourier domain mode-locked lasers", *Optics Letters*, **32**, 626-628, 2007.
56. Huber, R., et al., "Fourier domain mode locking at 1050 nm for ultra-high-speed optical coherence tomography of the human retina at 236,000 axial scans per second", *Optics Letters*, **32**, 2049-2051, 2007.
57. Klein, T., et al., "Multi-MHz retinal OCT", *Biomedical Optics Express*, **4**, 1890-1908, 2013.
58. Wang, T., et al., "Intravascular optical coherence tomography imaging at 3200 frames per second", *Optics Letters*, **38**, 1715-1717, 2013.
59. Wieser, W., et al., "Multi-Megahertz OCT: High quality 3D imaging at 20 million A-scans and 4.5 GVoxels per second", *Optics Express*, **18**, 14685-14704, 2010.
60. Wieser, W., et al., "High definition live 3D-OCT in vivo: design and evaluation of a 4D OCT engine with 1 GVoxel/s", *Biomedical Optics Express*, **5**, 2963-2977, 2014.
61. Denk, W., J. Strickler, and W. Webb, "Two-photon laser scanning fluorescence microscopy", *Science*, **248**, 73-76, 1990.
62. Goeppert-Mayer, M., "Über Elementarakte mit zwei Quantensprüngen", *Annalen der Physik*, **9**, 273-294, 1931.
63. Kaiser, W. and C.G.B. Garrett, "Two-Photon Excitation in CaF^2:Eu^{2+}", *Physical Review Letters*, **7**, 229-231, 1961.
64. Chen, S.-Y., et al., "*In Vivo* Virtual Biopsy of Human Skin by Using Noninvasive Higher Harmonic Generation Microscopy", *Selected Topics in Quantum Electronics, IEEE Journal of*, **16**, 478-492, 2010.
65. Chemnitz, M., et al., "Widely tuneable fiber optical parametric amplifier for coherent anti-Stokes Raman scattering microscopy", *Optics Express*, **20**, 26583-26595, 2012.
66. Leonhardt, R., et al., "Nonlinear optical frequency conversion of an amplified Fourier Domain Mode Locked (FDML) laser", *Optics Express*, **17**, 16801-16808, 2009.

List of publications

1. Wieser, W., T. Klein, D.C. Adler, F. Trépanier, C.M. Eigenwillig, **S. Karpf**, J.M. Schmitt, and R. Huber, "Extended coherence length megahertz FDML and its application for anterior segment imaging", *Biomedical Optics Express*, **3**, 2647-2657, 2012.
2. Wieser, W., T. Klein, **S. Karpf**, C.M. Eigenwillig, L. Reznicek, A. Kampik, A.S. Neubauer, and R. Huber, "1.6 MHz Single-Spot OCT Imaging the Whole Anterior Segment", *ARVO Meeting Abstracts*, **53**, 3114, 2012.
3. Wieser, W., W. Draxinger, T. Klein, **S. Karpf**, T. Pfeiffer, and R. Huber, "High definition live 3D-OCT in vivo: design and evaluation of a 4D OCT engine with 1 GVoxel/s", *Biomedical Optics Express*, **5**, 2963-2977, 2014.
4. **Karpf, S.**, M. Eibl, and R. Huber, "Two Photon Excitation Fluorescence Microscopy with Nanosecond Pulses from a Fiber-based Master Oscillator Power Amplifier", *in preparation*, 2015.
5. **Karpf, S.**, M. Eibl, W. Wieser, T. Klein, and R. Huber, "A Time-Encoded Technique for fibre-based hyperspectral broadband stimulated Raman microscopy", *Nature Communications*, 2015.
6. **Karpf, S.**, M. Eibl, W. Wieser, T. Klein, and R. Huber, "Multi-color fiber MOPA with electronically switchable wavelength shifter for non-linear laser spectroscopy", *in preparation*, 2015.
7. **Karpf, S.**, M. Eibl, W. Wieser, T. Klein, and R. Huber, "Time-encoded Raman spectroscopy with a rapidly wavelength swept CW-laser", *in preparation*, 2015.

Conference contributions

1. Dobrindt, J., **S. Karpf**, S. Krysiak, B. Schröter, B. Nickel, J. Rädler, and T. Kippenberg. *Dispersive single particle sensing with µs time resolution using toroidal microresonators*. in *CLEO/Europe and EQEC 2011 Conference Digest*. 2011. Munich: Optical Society of America.
2. Wieser, W., T. Klein, D.C. Adler, F. Trépanier, C. Eigenwillig, **S. Karpf**, J.M. Schmitt, and R.A. Huber. *Extended Coherence Range Megahertz FDML Laser for Imaging the Human Anterior Segment*. in *Biomedical Optics and 3-D Imaging*. 2012. Miami, Florida: Optical Society of America.
3. Wieser, W., T. Klein, D.C. Adler, F. Trépanier, **S. Karpf**, C. Eigenwillig, J.M. Schmitt, and R. Huber. *Dispersion Compensated Megahertz FDML Laser for Imaging of the Anterior Segment*. in *Conference on Lasers and Electro-Optics 2012*. 2012. San Jose, California: Optical Society of America.
4. **Karpf, S.**, M. Eibl, W. Wieser, T. Klein, and R. Huber. *FDML Raman: New High Resolution SRS with ultra broadband spectral coverage*. in *2013 Conference on Lasers and Electro-Optics - International Quantum Electronics Conference*. 2013. Munich: Optical Society of America.
5. **Karpf, S.**, M. Eibl, W. Wieser, T. Klein, and R. Huber. *FDML Raman: High Speed, High Resolution Stimulated Raman Spectroscopy with Rapidly Wavelength Swept Lasers*. in *CLEO: 2013*. 2013. San Jose, California: Optical Society of America.

6. Eibl, M., **S. Karpf**, W. Wieser, T. Klein, and R. Huber. *Broadband, High Resolution Stimulated Raman Spectroscopy with Rapidly Wavelength Swept CW-Lasers*. in *CLEO: 2014*. 2014. San Jose, California: Optical Society of America.
7. Eibl, M., **S. Karpf**, W. Wieser, T. Klein, and R. Huber. *Laser sources for Time-Encoded Raman microscopy: FDML probe and multi-wavelength MOPA pump lasers for fiber-based, hyperspectral SRS microscopy*. in *MicroCor 2014*. 2014. Heidelberg, Germany.
8. Eibl, M., **S. Karpf**, W. Wieser, T. Klein, and R. Huber, "Swept Source Raman Spectroscopy ", in *ICORS 2014*: Jena, 2014.
9. **Karpf, S.**, M. Eibl, T. Klein, W. Wieser, and R. Huber. *Hyperspectral Stimulated Raman Microscopy with Fiber-based, Rapidly Wavelength Swept CW-Lasers*. in *CLEO: 2014*. 2014. San Jose, California: Optical Society of America.
10. **Karpf, S.**, M. Eibl, W. Wieser, T. Klein, and R. Huber, "Time-Encoded Raman: Hyperspectral Stimulated Raman Microscopy with Fiber-based, Rapidly Wavelength Swept CW-Lasers", in *MicroCor 2014*: Heidelberg, Germany, 2014.
11. **Karpf, S.**, M. Eibl, W. Wieser, T. Klein, and R. Huber, "Fiber-based multi-wavelength laser for stimulated Raman scattering spectroscopy", in *ICORS 2014*: Jena, 2014.
12. **Karpf, S.**, M. Eibl, W. Wieser, T. Klein, and R. Huber, "Swept Source, hyperspectral Raman Microscopy with Fiber-based, Rapidly Wavelength Swept CW-Lasers", in *ICORS 2014*: Jena, 2014.
13. **Karpf, S.**, M. Eibl, and R. Huber, "All fiber based, multi-color two photon excitation microscopy with an amplified laser diode ", in *Multiphoton Microscopy in the Biomedical Sciences XV, BiOS 2015*: San Francisco. p. Paper 9329-101, 2015.
14. **Karpf, S.**, M. Eibl, W. Wieser, T. Klein, and R. Huber, "TICO Raman: time encoded Raman spectroscopy and microscopy with rapidly wavelength swept lasers", in *Multiphoton Microscopy in the Biomedical Sciences XV, BiOS 2015*: San Francisco. p. Paper 9329-105, 2015.

Patent applications

1. R. Huber, **S. Karpf**, M. Eibl, W. Wieser, and T. Klein, *A system and method for stimulated Raman spectroscopy*, WO2014180986 (2013)
2. **S. Karpf**, R. Huber, and M. Eibl, *A Coherent Dynamically Controllable Narrow Band Light Source*, WO2014180983 (2013)
3. **S. Karpf**, R. Huber, and M. Eibl, *A system and method for inducing and detecting multi-photon processes in a sample*, EP14001980.3 (2014)

Words of Appreciation

First of all, I want to thank my advisor Robert Hubert for giving me the opportunity to conduct research on this very interesting subject. His deep understanding paired with his capability of explaining the physics at hand greatly enriched the work and made research fun and stimulating. His ideas and his profound experience were of immeasurable value to this work. Further, I would like to thank my colleague Matthias Eibl. He started as a diploma student when the quest for a "Raman signal" was the daily concern of our efforts when starting the Raman project. Together we mastered to overcome this hurdle and created a very efficient and stimulating working atmosphere with many fruitful discussions and great findings. Thank you for the friendly working atmosphere and the perfect teamwork.

Special thanks to Wolfgang Wieser who helped a lot with his profound knowledge and deep understanding of electronics and programming that helped immensely with the success of this project. Also, I would like to thank the rest of the AG-Huber, Thomas Klein, Christoph Eigenwillig, Tom Pfeiffer, Jan Philip Kolb, Korbinian Schreiber, Andreas Weißl and all the others who helped with a collaborative and friendly working atmosphere. Many thanks to Professor Zinth for fruitful discussions on the project. His deep insight and profound experience with molecular spectroscopy and optics helped with the success of this research. Thanks to the whole BMO for the nice working atmosphere and the social events like the skiing trips and the soccer evenings. Thanks to the machining group at the BMO, Rudi Schwarz, Christian Hausmann, Alfons Stork, Harald Hoppe and Isabell Kalbe. Thanks also to the secretaries Ms. Widmann and Ms. Michaelis. Last, but not least, I want to thank my family and especially my beloved wife Alice for supporting me all these years. I am truly grateful to have all of you in my life.